



3 1293 00913 9498

This is to certify that the
dissertation entitled
INFRARED-INFRARED DOUBLE RESONANCE
STUDIES OF COLLISIONAL INTERACTIONS AND
POLARIZATION PHENOMENA

presented by

Uhyon Shin

has been accepted towards fulfillment
of the requirements for

Ph.D. degree in Chemistry

Major professor

Date May 9, 1991



**PLACE IN RETURN BOX to remove this checkout from your record.
TO AVOID FINES return on or before date due.**

DATE DUE	DATE DUE	DATE DUE
_____	_____	_____
_____	_____	_____
_____	_____	_____
_____	_____	_____
_____	_____	_____
_____	_____	_____
_____	_____	_____

MSU is An Affirmative Action/Equal Opportunity Institution

c:\cir\date.due.pm3-p.1

INFRARED-INFRARED DOUBLE RESONANCE
STUDIES OF COLLISIONAL INTERACTIONS AND
POLARIZATION PHENOMENA

By
Uhyon Shin

A DISSERTATION

submitted to
Michigan State University
in partial fulfilment of the requirements
for the degree of

DOCTOR OF PHILOSOPHY

Department of Chemistry

1991

ABSTRACT

INFRARED-INFRARED DOUBLE RESONANCE STUDIES OF COLLISIONAL INTERACTIONS AND POLARIZATION PHENOMENA

By

Uhyon Shin

Infrared-infrared double resonance experiments were used to study collisional interactions of CH_3F molecules and laser-induced optical anisotropy. From the line-shapes of four-level double resonance signals recorded under intensity modulation, velocity changes of molecules as a result of collisions were calculated by using the Keilson-Storer collision kernel. Four independent forms of laser-induced optical anisotropy were related to various forms of polarization modulation experiments using a Jones calculus. It is pointed out that linear dichroism, linear birefringence, circular dichroism, and circular birefringence can be independently detected with different experimental configurations. Dispersion shapes of circular birefringence were recorded by passing a plane polarized probe through a polarizer with $\theta = 45^\circ$ while the polarization of the pump laser was modulated between left- and right-circular polarization. The technique for measuring pure birefringence signals shows a promising future for measuring accurate transition frequencies as well as for assigning recorded spectra. Time domain measurement of intensity modulated infrared-infrared double resonance is also described.

DEDICATION

TO

my parents

wife, Young Gyo

my daughter, Mina A.

and

many invaluable friends

Acknowledgements

I would like to thank Professor Richard H. Schwendeman for the many critical contributions and his moral support through all the difficult hours in this research, as well as in preparing this thesis. My thanks are extended to Professors George Leroi, Stanley Crouch, and Daniel Nocera who shared their scientific insights and their instruments for my research. All of previous and current group members deserve partial credits for this thesis.

TABLE OF CONTENTS

LIST OF TABLE	viii
LIST OF FIGURES	x
1 Introduction	1
I Definitions	3
II Saturation Absorption Spectroscopy	5
A Lineshape Problem in Saturation Absorption Spectroscopy . .	5
B Lineshape Study of Transferred Spikes in $^{12}\text{CH}_3\text{F}$	7
C Lineshape Dependence on the Polarization	9
III Polarization Spectroscopy	10
IV Time Resolved Spectroscopy	11
2 Theory	13
I Line Broadening	13
II Creation and Detection of Bennett Holes	14
III Lineshape Study of Transferred Spikes	17
IV <i>M</i> Selection Rules	22
V Alignment and Orientation	23
VI Absorption and Dispersion	24
VII Optical Anisotropy	25
A Saturation Absorption Spectroscopy	26

B	Alignment Modulation vs. Orientation Modulation	26
VIII	Polarization Spectroscopy	28
IX	Jones Calculus	32
3	Experimental	41
I	Lineshape Study of Transferred Spikes	41
II	Polarization Spectroscopy	44
III	Time Resolved Spectroscopy	51
A	Electro-Optic Switch	54
B	Data Acquisition	59
4	Results and Discussion	61
I	Introduction	62
II	Lineshape Study of Transferred Spikes in $^{12}\text{CH}_3\text{F}$	64
A	Three-Level Double Resonance	64
B	Four-Level Double Resonance	68
C	Summary	79
III	Saturation Absorption Spectroscopy in $^{13}\text{CH}_3\text{F}$	80
A	Three-level Double Resonance Lineshape	80
B	Four-Level Double Resonance Lineshape	85
C	Simultaneous Measurements of Spikes for Co- and Counter- propagating Beam Geometry.	88
IV	Polarization Spectroscopy	93
V	Polarization Modulation	95
A	Alignment Modulation (σ^\pm/π)	95
B	Orientation Modulation (σ^-/σ^+)	98
C	Laser-induced Birefringence	100
VI	Polarization Labeling	107
VII	Backward and Forward Spikes: Revisited	110
VIII	Time Resolved Spectroscopy	113

A	Measurement of Relaxation rates	113
B	Phase Separation of Ortho- and Para-transitions	117
IX	Summary	121
5	Conclusion and Future Work	123
	APPENDIX	127
	REFERENCES	132

LIST OF TABLES

1.1	List of calculated coincidences between transitions in the ν_3 band of $^{12}\text{CH}_3\text{F}$ and CO_2 laser frequencies studied.	6
2.1	M selection rules for various polarizations states of laser. It should be noted that the laser propagates along the Y axis and the reference plane is $YZ(\pi)$	23
2.2	Comparison of calculated intensities using Jones calculus for different experimental conditions.	39
4.1	List of transitions of the $2\nu_3 \leftarrow \nu_3$ band in $^{12}\text{CH}_3\text{F}$ and their frequencies plotted in this Chapter.	89
4.2	List of transitions of the ν_3 band in $^{12}\text{CH}_3\text{F}$ and their frequencies plotted in this Chapter.	89
4.3	Velocity changes upon collision for ν_3 band transitions in $^{12}\text{CH}_3\text{F}$. The $^{\text{Q}}\text{R}(11,9)$ transition in the ν_3 band was pumped.	90
4.4	Velocity changes upon collision for $2\nu_3 \leftarrow \nu_3$ band transitions in the CH_3F . The $^{\text{Q}}\text{R}(11,9)$ transition in the ν_3 band was pumped.	91
4.5	List of transitions and their frequencies (MHz) in $^{13}\text{CH}_3\text{F}$ plotted in this Chapter.	92
4.6	Summary of relative signs observed in the population- and orientation-modulated double resonance signals. P, Q, R : Branch of the transition. +, -, and 0 are for positive, negative, and no observable signal, respectively.	109

5.1	Summary of identified relaxation paths, lineshapes, relaxation times, and their effects on velocity, alignment, and orientation.	125
-----	---------------------------------------------------------------------------------------------------------------------------------------------	-----

LIST OF FIGURES

2.1	A typical absorption line shape with a Bennett hole. The X -axis is frequency in units of MHz. Y -axis is the absorption intensity. The line shape was simulated with a Gaussian of 30 MHz HWHM and a Lorentzian of 1 MHz HWHM.	15
2.2	A typical double resonance absorption line shape with a modulated pump beam. The X -axis is frequency in units of MHz. Y -axis is the absorption intensity. The lineshape is Lorentzian of 1 MHz HWHM. .	16
2.3	Alignment and orientation created by polarized lasers. In (a) the dashed lines are for YX plane polarized light (σ^\pm) whereas the continuous line is for YZ plane polarized light (π). In (b) the dashed and continuous lines are for right- (σ^+) and left- (σ^-) circularly polarized pump radiation, respectively.	25
2.4	Two different saturation absorption configurations: (a) π pump, π probe; (b) π pump, σ^\pm probe. It should be noted that the selection of π is arbitrary, since there is no field applied to the sample. At some places the π and the σ^\pm is interchanged for the convenience of explanation or calculation. Exchanging the π and the σ^\pm should give the same result.	27

- 3.1 A CO₂ laser infrared microwave sideband laser double resonance system. The two CO₂ lasers are frequency stabilized to the fluorescence Lamb dip of CO₂(FC). The sideband is generated by mixing one of the CO₂ lasers with high power microwaves (8 – 18 GHz) in a CdTe crystal (Mod) and its intensity is stabilized by monitoring its output (RD). Since the sideband is amplitude modulated at 33 kHz, detected signals (SD,RD) always get demodulated at 33 kHz first by L1 or L3. The output from L1 is double demodulated (L2) at the chopping frequency (~ 100 Hz). The signal from L2 comes therefore purely from double resonance effects. Since the pump laser modulated by a mechanical chopper has a horizontal plane of polarization, it can be separated from the sideband laser using two polarizers P1,P2. The use of a polarizer to separate the two laser beams allows easy and perfect alignment that is critical to the lineshape. 42
- 3.2 Block diagram of the CO₂ laser – IMSL double resonance setup employing an electro-optic modulator. When 2.1 kV is applied to the CdTe modulator, it converts the YX plane polarized (π) pump laser into right circularly polarized (σ^+) light. The σ^+ radiation is changed back to a π -polarized laser after the rhomb (Rh) that works as a quarter wave plate. The laser passes a blocking polarizer (P1) whose angle is set to π and perturbs molecules in the sample cell. If -2.1 kV is applied instead, the pump laser becomes σ^\pm polarized and is reflected off the polarizer to a beam stop. The result is a TTL controlled optical modulator with π plane polarized laser pumping (perpendicular configuration). The same setup can be used to modulate σ^\pm plane polarized pump by rotating the blocking polarizer parallel to the YZ plane (parallel configuration). 45

- 3.3 Diagram of the electro-optic switching system. A TTL signal controls the high voltage control circuit and applies either +2.1 kV or -2.1 kV to the CdTe housing. A $YX(\pi)$ plane polarized pump beam (PL) is either converted to right circular polarization (σ^+) or to left circular polarization (σ^-) by the CdTe, depending on the polarity of the high voltage applied to it. A Fresnel rhomb oriented at 45° converts the circularly polarized beams back into either σ^\pm or π . A blocking polarizer (P1) whose angle is set parallel to the YX plane blocks the σ^\pm polarization of the pump beam and passes only the π polarized state of the pump beam. Since the intensity of the pump beam follows the shape of the TTL signal shown in the picture, this is called *intensity modulation* in the text. The different polarization states of the pump laser are shown with I (π), II (σ^+, σ^-), III (π, σ^\pm), and IV (π). The blocking polarizer (P1) can be rotated to obtain σ^\pm at IV. 47
- 3.4 Block diagram for alignment modulation between σ^\pm and π . Note: The intensities of the two σ^\pm - and π -polarized pump beams do not change. Only the polarization state of the pump beam is switched. Therefore, the pump always creates the same holes and spikes in terms of total population while the alignment of the molecules is different. 48
- 3.5 (a) Alignment modulated double resonance signal of the P(6,0), P(6,1), P(6,2), and P(6,3) in the $2\nu_3 \leftarrow \nu_3$ band of $^{13}\text{CH}_3\text{F}$. (b) Power modulated signal. The absolute intensity of the alignment modulated signal was about 1/3 of the normal double resonance signal. It is clear that the Gaussian signals are suppressed in the alignment modulation. The x -axis is the microwave frequency in MHz used to generate the sideband laser. When the transition is observed with negative sideband, the numbers are labeled in decreasing order. 49
- 3.6 Modulation of the polarization states between σ^+ and σ^- . Again the intensity of the pump beam stays constant, as in alignment modulation. Either a circularly polarized probe beam or a plane polarized beam can be used to observe the optical anisotropy created in this pump scheme. 50

- 3.7 (a) Intensity modulated double resonance signal. of the R(4,3) transition in the ν_3 band of $^{13}\text{CH}_3\text{F}$. (b) Orientation modulated double resonance signal. (c) Single resonance absorption signal. The single resonance absorption signal has a Bennett hole due to the laser pumping. The orientation modulated double resonance signal has dispersion line shape. The horizontal axis is the (negative) microwave offset frequency (MHz). 52
- 3.8 Experimental conditions for (a) alignment pumping: π -polarized pump, π -polarized probe; (b) alignment pumping: π -polarized pump, σ^\pm -polarized probe; (c) alignment modulation: π -polarized probe, $\sigma^\pm - \pi$ polarized pump; (d) orientation pumping: π probe, σ^+ pump, 90° polarizer; (e) orientation modulation: σ^+ probe, $\sigma^+ - \sigma^-$ pump, and (f) orientation modulation: π probe, $\sigma^+ - \sigma^-$ pump, 45° polarizer. For historical reasons (a) and (b) are also called as saturation absorption whereas (d) is called as polarization spectroscopy. Experiment (f) is named circular birefringent measurement because it measures laser-induced circular birefringence. 53
- 3.9 A schematic of the time resolved double resonance system used in this study. The flowing gas laser (Laser1) was used to pump $^{\text{Q}}\text{R}(4,3)$ transition in the ν_3 band. The beam paths of two CO_2 lasers and the high voltage cables are drawn with thick lines. The dashed line represents the IMSL beam path. Details of the operation are described in the text. 55

- 3.10 Diagram of the electro-optic switching system used for time resolved measurement. A TTL signal controls the high voltage control circuit and applies either +2.1 kV or -2.1 kV to the CdTe housing. A $YZ(\pi)$ plane polarized pump beam (PL) is either converted to right circular polarization (σ^+) or to left circular polarization (σ^-) by the CdTe, depending on the polarity of the high voltage applied to it. A Fresnel rhomb oriented at 45° converts the circularly polarized beams back into either σ^\pm or π . A blocking polarizer whose angle is set parallel to the YZ plane blocks the σ^\pm polarization of the pump beam and passes only the π polarized state of the pump beam. The amplitude of the final pump beam (IV) follows the shape of the TTL signal that is applied. A σ^\pm polarized sideband laser (SL) interacts with the sample, reflects off P2, and is monitored by the detector (SD). 56
- 3.11 Double resonance spectra of the ${}^Q\text{P}(6,3)$ transition. Soft inelastic $\Delta J = 1$ collisions with a large impact diameter result in the sharp spike marked S whereas the Gaussian marked G comes from the vibrational swapping mechanism. With sub-Doppler resolution, the two processes in the same transition can be time resolved separately. . . . 57
- 3.12 Time resolved spectra of the ${}^Q\text{P}(6,3)$ transition. G represents the signal from the Gaussian whereas S is from the spike. At time 0, the pump laser is turned off and relaxation is observed whereas at time $570\mu\text{s}$ the pump laser is turned on, and an increase in signal was observed. The difference between G and S can be seen at early time ($< 10\mu\text{s}$) where the $\Delta J = 1$ process dominates. 58

- 4.1 Graphical illustration of velocity distribution of molecules involved in the pump and probe. The Bennett hole can be studied by probing either the ${}^{\text{Q}}\text{P}(4,3)$ or the ${}^{\text{Q}}\text{Q}(4,3)$ transition while the Bennett spike can be done by using the ${}^{\text{Q}}\text{P}(5,3)$ transition in $2\nu_3 \leftarrow \nu_3$ band. The Bennett spike is collisionally transferred into different rotational levels and probed by four-level double resonance. It is not clear whether there exist transferred holes or not. 62
- 4.2 Three-level infrared-infrared double-resonance spectra of the ${}^{\text{Q}}\text{P}(12,2)$ transition in the ν_3 band of ${}^{12}\text{CH}_3\text{F}$; the ${}^{\text{Q}}\text{Q}(12,2)$ transition in the same band was pumped by the $9\text{P}(20) {}^{12}\text{C}^{16}\text{O}_2$ laser. The horizontal axis is the (negative) microwave frequency (MHz) offset from the $9\text{R}(12) {}^{13}\text{C}^{16}\text{O}_2$ laser. The lower trace is the single + double resonance and the upper trace is the double resonance. 65
- 4.3 Three-level Infrared-infrared double resonance spectra of the ${}^{\text{Q}}\text{Q}(11,9)$ transition in the ν_3 band of ${}^{12}\text{CH}_3\text{F}$; the ${}^{\text{Q}}\text{R}(11,9)$ transition in the same band was pumped by the $9\text{P}(22) {}^{12}\text{C}^{18}\text{O}_2$ laser. The horizontal axis is the microwave frequency (MHz) offset from the $9\text{P}(20) {}^{12}\text{C}^{16}\text{O}_2$ laser. The lower trace is the single + double resonance and the upper trace is the double resonance. The broad line was recorded after the first demodulation. For simplicity, the term *single resonance signal* is used to indicate this part in the text, since it is the average value of the single resonance and the double resonance. The spectrum with a sharp spike was recorded after the second demodulation. This part is called the *double resonance signal* in the text; it is the double resonance minus the single resonance. The area of the Bennett hole measured in the single resonance signal was $\sim 1\%$ of the total area, which implies that $\sim 2\%$ of the molecules in the ground state are excited by the laser pumping. 66

- 4.4 Three-level infrared-infrared double-resonance spectrum of the ${}^{\text{Q}}\text{Q}(12,9)$ transition in the $2\nu_3 \leftarrow \nu_3$ band of ${}^{12}\text{CH}_3\text{F}$; the ${}^{\text{Q}}\text{R}(11,9)$ transition in the ν_3 band was pumped by the $9\text{P}(22)$ ${}^{12}\text{C}^{18}\text{O}_2$ laser. The horizontal axis is the (negative) microwave frequency (MHz) offset from the $9\text{P}(36)$ ${}^{12}\text{C}^{16}\text{O}_2$ laser. 67
- 4.5 Four-level infrared-infrared double-resonance of the ${}^{\text{Q}}\text{P}(14,0)$ - ${}^{\text{Q}}\text{P}(14,5)$ transitions in the $2\nu_3 \leftarrow \nu_3$ band of ${}^{12}\text{CH}_3\text{F}$. The ${}^{\text{Q}}\text{Q}(12,2)$ and ${}^{\text{Q}}\text{Q}(12,1)$ transitions in the ν_3 band, were pumped simultaneously by the $9\text{P}(20)$ ${}^{12}\text{C}^{16}\text{O}_2$ laser. The horizontal axis is the (negative) microwave frequency (MHz) offset from the $9\text{P}(12)$ ${}^{13}\text{C}^{16}\text{O}_2$ laser. Transferred spikes are seen on both the ${}^{\text{Q}}\text{P}(14,2)$ and ${}^{\text{Q}}\text{P}(14,1)$ transitions. (The ${}^{\text{Q}}\text{P}(14,1)$ and ${}^{\text{Q}}\text{P}(14,0)$ transitions are almost completely overlapped.) 69
- 4.6 Four level infrared-infrared double resonance of the ${}^{\text{Q}}\text{Q}(9,3)$ - ${}^{\text{Q}}\text{Q}(9,9)$ and ${}^{\text{Q}}\text{Q}(12,3)$ - ${}^{\text{Q}}\text{Q}(12,9)$ transitions in the $2\nu_3 \leftarrow \nu_3$ band of ${}^{12}\text{CH}_3\text{F}$. The ${}^{\text{Q}}\text{Q}(12,K)$ transitions are the result of absorption of the negative sideband while ${}^{\text{Q}}\text{Q}(9,K)$ transitions are the result of absorption of the positive sideband, both of which are present in the probe radiation. The horizontal axis is the microwave frequency (MHz) offset from the $9\text{P}(36)$ ${}^{12}\text{C}^{16}\text{O}_2$ laser, negative for ${}^{\text{Q}}\text{Q}(12,K)$, positive for ${}^{\text{Q}}\text{Q}(9,K)$. The ${}^{\text{Q}}\text{R}(11,9)$ transition in the ν_3 fundamental band was pumped by the $9\text{P}(22)$ ${}^{12}\text{C}^{18}\text{O}_2$ laser. Calculated frequencies and relative intensities for normal single resonance spectra are plotted below the recorded spectra with + for $J=9$ and with \diamond for $J=12$ 70
- 4.7 Four-level infrared-infrared double-resonance spectrum of the ${}^{\text{Q}}\text{R}(13,9)$ transition in the $2\nu_3 \leftarrow \nu_3$ band of ${}^{12}\text{CH}_3\text{F}$; the ${}^{\text{Q}}\text{R}(11,9)$ transition in the ν_3 band was pumped by the $9\text{P}(22)$ ${}^{12}\text{C}^{16}\text{O}_2$ laser. The horizontal axis is the (negative) microwave frequency (MHz) offset from the $9\text{P}(36)$ ${}^{12}\text{C}^{16}\text{O}_2$ laser. 71
- 4.8 A typical double resonance spectrum in the fundamental band. (${}^{\text{Q}}\text{R}(11,9)$ transition in the ν_3 band is shown.) 72

4.9	Comparison of observed (noisy line) and calculated (smooth line) four-level double-resonance spectrum for the ${}^{\text{Q}}\text{Q}(9,9)$ transition in the $2\nu_3 \leftarrow \nu_3$ band of ${}^{12}\text{CH}_3\text{F}$; the ${}^{\text{Q}}\text{R}(11,9)$ transition in ν_3 band was pumped by the 9P(22) ${}^{12}\text{C}^{18}\text{O}_2$ laser. The horizontal axis is the microwave frequency (MHz) offset from the 9P(36) ${}^{12}\text{C}^{16}\text{O}_2$ laser. The calculated curve is the best fit to a single Keilson-Storer function + Gaussian.	72
4.10	Comparison of observed (noisy line) and calculated (smooth line) four-level double-resonance spectrum for the same pump-probe combination and horizontal axis as shown in Fig. 8. Here, the calculated curve is the best fit to a sum of two Keilson-Storer function + Gaussian. . . .	73
4.11	Plot of the ratio of the area of the wide spike to that of the narrow spike <i>vs.</i> ΔJ for the four-level double resonances listed in Table 4.2. .	73
4.12	Plot of the r.m.s. change in speed <i>vs.</i> ΔJ for the molecules that contribute to the broad spike for the four-level double resonance transitions listed in Table 4.2.	74
4.13	Plot of the ratio of the area of the wide spike to that of the narrow spike <i>vs.</i> ΔJ for the four-level double resonances.	75
4.14	Three-level double resonance spectra of ${}^{\text{Q}}\text{P}(5,3)$ transition in the $2\nu_3 \leftarrow \nu_3$ band while the ${}^{\text{Q}}\text{R}(4,3)$ transition in the ν_3 fundamental band was pumped. The intensities of both peaks were normalized. (a) σ^{\pm} probe and σ^{\pm} pump is broader than (b) π probe and σ^{\pm} pump. Sample pressure was 19 <i>mTorr</i>	79
4.15	Three-level double resonance spectra of the ${}^{\text{Q}}\text{P}(5,3)$ transition in the $2\nu_3 \leftarrow \nu_3$ band while the ${}^{\text{Q}}\text{R}(4,3)$ transition in the ν_3 fundamental band was pumped. (a) σ^{\pm} probe and σ^{\pm} pump is weaker than (b) π probe and σ^{\pm} pump. Sample pressure was 19 <i>mTorr</i>	79
4.16	Pump/probe polarization dependence of three-level double resonance observed in the ${}^{\text{Q}}\text{P}(5,3)$ transition, recorded with 3 <i>mTorr</i> sample. . .	80

4.17 Pump/probe polarization dependence of three-level double resonance observed in the ${}^Q\text{P}(5,3)$ transition, recorded with 1.5 mTorr sample.	81
4.18 Calculated three level double resonance lineshape under (a) thin line: σ^\pm/σ^\pm (b) thick line: σ^\pm/π configurations, respectively.	81
4.19 Pressure dependence of three-level double resonance observed in ${}^Q\text{P}(5,3)$ transition. To suppress relatively slow four-level contributions, the pump laser is optically modulated at 1 kHz.	82
4.20 Four-level double resonance lineshape of the ${}^Q\text{P}(6,3)$ transition recorded with σ^\pm pump and (a) σ^\pm probe (thick line) (b) π probe (thin line). The two peaks had different intensity values and were normalized for comparison. Sample pressure was 21 mTorr.	83
4.21 Four-level double resonance lineshape observed in the ${}^Q\text{P}(6,3)$ transition at various pressures.	84
4.22 A dip observed from the ${}^Q\text{P}(4,3)$ transition. Sample pressure was 1.5 mTorr. The skewed direction and its width are similar to the dip observed from the ${}^Q\text{P}(6,3)$ transition.	84
4.23 Four-level double resonance lineshape observed in the ${}^Q\text{P}(7,3)$ transition. Sample pressure was 1.5 mTorr. The peak is symmetric at the top and does not show any sign of dip.	85
4.24 The ${}^Q\text{R}(4,3)$ transition in the ν_3 band of ${}^{13}\text{CH}_3\text{F}$ was probed by an IMSL operating on the 9R(26) line of a ${}^{13}\text{CO}_2$ laser while being pumped by another 9R(32) CO_2 laser. The spike under counter propagating condition is at -16339.0 MHz whereas that at -16290.5 MHz is for the co-propagating condition. The difference between the two spikes is 48.5 MHz which corresponds to 24.25 MHz offset.	87
4.25 The ${}^Q\text{P}(5,3)$ transition in the $2\nu_3 \leftarrow \nu_3$ band of ${}^{13}\text{CH}_3\text{F}$ was probed by an IMSL operating on the 9P(16) line of a ${}^{13}\text{CO}_2$ laser while the ${}^Q\text{R}(4,3)$ transition in the ν_3 band was being pumped by another 9R(32) CO_2 laser. The center frequencies of the co- and counter-propagating spikes are 14596.0 MHz and 14547.0 MHz, respectively.	88

- 4.26 The ${}^{\text{Q}}\text{Q}(12,9)$ transition in the $2\nu_3 \leftarrow \nu_3$ band of ${}^{12}\text{CH}_3\text{F}$ was probed by an IMSL operating on the 9P(36) line of a ${}^{12}\text{CO}_2$ laser while the ${}^{\text{Q}}\text{R}(11,9)$ transition in the ν_3 band was pumped by another 9P(22) C^{18}O_2 laser. The spike under counter propagating conditions is at -9409.6 MHz whereas it is at -9361.7 MHz for co-propagating condition. The difference between the two spikes is 47.9 MHz which corresponds to 24.8 MHz offset in the ${}^{\text{Q}}\text{R}(11,9)$ after correcting for the Doppler effect. 93
- 4.27 ${}^{\text{Q}}\text{P}(5,3)$ in $2\nu_3 \leftarrow \nu_3$ of ${}^{13}\text{CH}_3\text{F}$ at 6 mTorr. The ${}^{\text{Q}}\text{R}(4,3)$ in the ν_3 fundamental band was pumped by a σ^+ 9R(32) CO_2 laser. Description of the experimental conditions is given in the text. 95
- 4.28 ${}^{\text{Q}}\text{P}(5,3)$ in $2\nu_3 \leftarrow \nu_3$ of ${}^{13}\text{CH}_3\text{F}$ at 60mTorr. The ${}^{\text{Q}}\text{R}(4,3)$ in the ν_3 fundamental band was pumped by a σ^+ 9R(32) CO_2 laser. The experimental arrangement is described in the text. 95
- 4.29 The frequency of the σ^{\pm} polarized probe laser was scanned from the ${}^{\text{Q}}\text{P}(5,0)$ to the ${}^{\text{Q}}\text{P}(5,4)$ transitions in the $2\nu_3 \leftarrow \nu_3$ band of ${}^{13}\text{CH}_3\text{F}$ while the polarization of the pump laser coincident on the ${}^{\text{Q}}\text{R}(4,3)$ transition in the ν_3 band was switched between σ^{\pm} and π . There is no sign of signal other than at the frequency where the ordinary spike is observed, which implies that only the spike changes its orientation to follow the change in polarization of the pump beam. 97
- 4.30 The frequency of the probe laser was scanned from the ${}^{\text{Q}}\text{P}(6,0)$ to ${}^{\text{Q}}\text{P}(6,3)$ transitions while (a) the polarization of the pump laser was switched between σ^{\pm} and π and (b) the pump beam was intensity modulated by blocking its σ^{\pm} component. Signals from the Gaussian part are apparent in (b) intensity modulation, but not in (a) alignment modulation. 98

- 4.31 Photo-selected VCD observed from ${}^Q\text{P}(5,3)$ in the $2\nu_3 \leftarrow \nu_3$ band of ${}^{13}\text{CH}_3\text{F}$ while the ${}^Q\text{R}(4,3)$ in the ν_3 band was pumped. (a) A σ^+ probe was used while the polarization of the pump beam was modulated between σ^+ and σ^- . (b) A wire-grid polarizer was put in front of the sample cell to create a plane polarized probe beam. Other conditions were exactly same as in (a). (c) The polarizer used in (b) was moved to in front of the detector. The probe beam is circularly polarized while interacting with molecules but plane polarized at the detector. 100
- 4.32 A dispersion signal observed in the ${}^Q\text{P}(5,3)$ transition in the $2\nu_3 \leftarrow \nu_3$ band of ${}^{13}\text{CH}_3\text{F}$ while the ${}^Q\text{R}(4,3)$ transition in the ν_3 band was pumped. Two polarizers were used for the probe beam (one to generate a plane polarized probe beam before the sample cell, the other after sample cell set to 45° relative to the first polarizer) while the polarization of the pump beam was modulated between σ^+ and σ^- 103
- 4.33 Photo-selected VCD observed in the ${}^Q\text{P}(6,3)$ transition in the $2\nu_3 \leftarrow \nu_3$ band while the ${}^Q\text{R}(4,3)$ transition in the ν_3 band was pumped. A σ^+ probe was used while the polarization of the pump beam was modulated between σ^+ and σ^- 104
- 4.34 A dispersion signal observed in the ${}^Q\text{P}(6,3)$ transition in the $2\nu_3 \leftarrow \nu_3$ band of ${}^{13}\text{CH}_3\text{F}$ while the ${}^Q\text{R}(4,3)$ transition in the ν_3 band was pumped. Two polarizers were used for the probe beam (one to generate a plane polarized probe beam before the sample cell, the other after the sample cell set to 45° relative to the first polarizer) while the polarization of the pump beam was modulated between σ^+ and σ^- 105
- 4.35 Intensity modulated double resonance signal observed in the ${}^Q\text{P}(6,3)$ transition with the same conditions as in the previous figure. A σ^+ probe was used while the power of the π pump beam was modulated with a mechanical chopper. 106
- 4.36 Intensity modulated spectrum of the ${}^Q\text{P}(5,3)$ transition in the $2\nu_3 \leftarrow \nu_3$ band while the ${}^Q\text{R}(4,3)$ transition in the ν_3 band was pumped. 106

4.37	Intensity modulated spectrum of of the ${}^{\text{Q}}\text{P}(5,3)$ transition in the $2\nu_3 \leftarrow \nu_3$ band while the ${}^{\text{Q}}\text{R}(4,3)$ transition in the ν_3 band was pumped. A π probe was used with a analysing polarizer ($\theta = 45$) in front of the detector.	107
4.38	Orientation modulated spectrum of the ${}^{\text{Q}}\text{P}(5,3)$ transition in the $2\nu_3 \leftarrow \nu_3$ band while the ${}^{\text{Q}}\text{R}(4,3)$ transition in the ν_3 band was pumped. A π probe was used with a analysing polarizer ($\theta = 45$) in front of the detector.	107
4.39	The $(v, J, K) = (2, 4, 3) \leftarrow (1, 5, 3)$ observed in double resonance: (a) intensity modulated signal; (b) polarization modulated signal; (c) signal recorded after the first demodulation during polarization modulation.	109
4.40	The $(v, J, K) = (1, 5, 3) \leftarrow (0, 4, 3)$ observed in double resonance: (a) intensity modulated signal; (b) polarization modulated signal; (c) signal recorded after the first demodulation during polarization modulation.	110
4.41	The $(v, J, K) = (2, 11, 3) \leftarrow (1, 10, 3)$ observed in four-level double resonance under conditions of polarization modulation. The sign changes from positive to negative.	110
4.42	The $(v, J, K) = (2, 4, 3) \leftarrow (1, 5, 3)$ transition of ${}^{13}\text{CH}_3\text{F}$ was probed by an IMSL while $(v, J, K) = (1, 5, 3) \leftarrow (0, 4, 3)$ was pumped (a) by polarization modulation (PM) between σ^+ and σ^- (b) by intensity modulation (IM). In both cases the pump laser was reflected back into sample cell to record both of the spikes occurring under co- and counter-configuration.	112
4.43	The $(v, J, K) = (1, 5, 3) \leftarrow (0, 4, 3)$ double resonance signal recorded (a) after the first demodulation from L1 (b) after double demodulation from L2.	112
4.44	The $(v, J, K) = (2, 4, 3) \leftarrow (1, 5, 3)$ double resonance signal.	113

4.45	Time resolved spectra of the (transferred) spike of ${}^Q\text{P}(4,3)$, ${}^Q\text{P}(5,3)$, ${}^Q\text{P}(6,3)$, and of ${}^Q\text{P}(7,3)$ transitions in the $2\nu_3 \leftarrow \nu_3$ band. The ${}^Q\text{R}(4,3)$ transition in the ν_3 fundamental band was pumped on at $3 \mu\text{sec}$. The transient digitizer was pre-triggered to record starting values.	115
4.46	Time resolved signal of the ${}^Q\text{P}(6,3)$ transition at (a) 20 mTorr (b) 40 mTorr	116
4.47	Time resolved signal of the ${}^Q\text{P}(6,3)$ transition. (a) when the pump laser is turned on; (b) when the pump laser is turned off. The measured ON signal is subtracted from a constant to have common starting level. The on-stage time response is faster and more intense than the off-stage.	117
4.48	Time resolved signals of (a) sharp spike (b) Gaussian + broad spike observed in ${}^Q\text{P}(6,3)$ transition (c) Gaussian observed in ${}^Q\text{P}(6,2)$ transitions.	117
4.49	Double-resonance spectrum of ${}^Q\text{P}(22,K)$ transitions in the $2\nu_3 \leftarrow \nu_3$ band of ${}^{13}\text{CH}_3\text{F}$ upon which calculated frequencies and intensities are superposed. It is clear that the $K = 3n$ transitions are stronger than calculated compared with $K \neq 3n$ transitions. The pump transition is ${}^Q\text{R}(4,3)$ in the ν_3 band and the pump source is a $9\text{P}(32) {}^{12}\text{C}^{16}\text{O}_2$ laser. The probe source is the negative sideband on the $10\text{R}(14) {}^{12}\text{C}^{16}\text{O}_2$ laser; the horizontal axis is the microwave frequency offset.	119
4.50	Time resolved spectra of $K=3$ and $K=4$ transitions in Figure 4.51. The $K=3$ transition is stronger and faster than the $K=4$ transition.	119
4.51	Calculated output <i>vs.</i> phase setting of the lock-in amplifier for the peak double resonance signal for the ${}^Q\text{P}(22,3)$ (thin line) and ${}^Q\text{P}(22,4)$ (thick line) transitions shown in Figure 4.49.	120

4.52	Double-resonance spectrum of ${}^Q P(22, K)$ ($K=0..9$, left to right) transitions in the $2\nu_3 \leftarrow \nu_3$ band of ${}^{13}\text{CH}_3\text{F}$ observed with the 110° phase. (The calculated spectrum is drawn with vertical bars for comparison.) The pump transition is ${}^Q R(4,3)$ in the ν_3 band and the pump source is a $9P(32)$ ${}^{12}\text{C}^{16}\text{O}_2$ laser. The probe source is the negative sideband on the $10R(14)$ ${}^{12}\text{C}^{16}\text{O}_2$ laser; the horizontal axis is the microwave frequency offset.	121
5.1	Application of double resonance in remote sensing. By changing the incident angle of the pump beam, only a selected portion (a, b, or c) of the probe beam path is affected and its signal can be recovered after the double demodulation.	126

Chapter 1

Introduction

In saturated absorption spectroscopy or in polarization spectroscopy¹ sub-Doppler resolution is achieved by probing molecules in a selected velocity group affected by a pump laser. The earliest optical saturation spectroscopy experiments (Lamb-dip spectroscopy), “discovered”²⁻⁴ soon after the operation of the first gas laser by Javan in 1961,^{5,6} provided means for finding the center frequency of an inhomogeneously broadened line and for removing the inhomogeneous linewidth by responding selectively to the transition frequency of the gas media (atoms or molecules) at rest. The frequency of the laser can be locked electronically to the center of the dip and this technique continues to be used to stabilize laser frequencies.

Later improvements in the experimental design of saturation spectroscopy experiments resulted in exciting new experiments to be performed. The incorporation of a sample cell inside the laser cavity allowed a wider variety of molecular species to be studied, even with fixed frequency lasers.⁷ Then, the cell was put outside of the cavity in an attempt to perturb the laser as little as possible and to study as much physics as possible.⁸ The extracavity techniques of saturation spectroscopy are complicated by the fact that an output beam reflected back into the laser cavity tends to destabilize the oscillation frequency. Some sort of isolation is necessary between the laser and the experiment. In the earliest stage, and still one of the most widely used owing to its simplicity, the isolation was achieved by crossing the pump and probe beams at a small angle in the sample cell. The finite angle θ between the interacting beams

introduces a residual linear Doppler width of roughly $\theta\Omega_D$ ($\Omega_D =$ Doppler width) in the resonance line width. The interaction length of the beams is also limited. But, the nonlinear resonances can be conveniently detected by chopping the pump beam and detecting the resulting modulation of the transmitted probe intensity.⁸

In our laboratory, Brewster angle windows were used at first to separate a plane-polarized probe beam from the pump beam whose polarization was orthogonal to the probe beam. Even though this procedure provided truly counter-propagating beams, the number of added optical components necessary to achieve the separation made the technique inferior compared to the design using two polarizers introduced in this study.^{9,10} This design is described in Chapter 3. Fewer optical components and the use of polarizers allowed an observation of a splitting of the Bennett spike in infrared double resonance experiments.^{11,12} Later the use of a partially transmitting mirror was introduced,¹² in which lasers with arbitrary polarization can be used either for pump or for probe. This design is suitable for a variety of saturation spectroscopy experiments, in which the polarization information can be used to obtain information about spatial orientation of molecules or to aid interpretation of observed spectra.

Improved spectroscopic precision, better measurements of fundamental constants and of basic units,¹³⁻¹⁵ and new studies of collisional dynamics were only some of the exciting possibilities opened by saturated absorption and related techniques. Experimental and theoretical developments rapidly succeeded one another, making saturation spectroscopy now one of the most highly developed and best-understood nonlinear techniques. A number of books, review articles, and original sources elucidate the many phenomena expected and observed.^{7,14,16-19}

As pointed out by Levenson²⁰ saturation techniques have potential applications related to high-resolution spectroscopy and well-defined wavelength and frequency standards such as in *computer memory and data storage* by allowing at least 10,000 times higher storage density than the best video-disk technology, in *optical transistors*, in *adaptive optical devices* which can transmit high power laser beams through the atmosphere or to produce a pattern, or in *remote sensing* where spatial resolution can be achieved by crossing the pump and probe beams at different angles.

A thorough understanding of the basic principles of various saturation phenomena may open exciting new techniques and is the subject of this thesis, which also deals with collisional energy transfer processes that are vital in global simulations such as global warming and ozone depletion. Collisional processes are studied not only because of the interest in the nature of the collision process and intermolecular potentials, but also because of the vital need for well-characterized line shapes and line widths for recovery of information in remote sensing experiments.²¹⁻²³

In the next few sections a brief history and review of saturation absorption spectroscopy, polarization labeling, and time resolved experiments is presented. Relevant theories, experimental designs, and the results of this study are discussed in Chapters II, III, and IV. A summary of this dissertation is presented in Chapter V along with the suggestions of future works to be done.

I. Definitions

As new experimental techniques have developed, different names were devised to designate each experiment. Unfortunately in the many possible combinations of the polarization states involved in double resonance experiments, the terms *saturation absorption spectroscopy* or *polarization spectroscopy* have been used to describe many different types of experiments mainly because different experiments were performed in different groups. It was understood that the term saturation absorption spectroscopy represents experiments in which the total population changes induced by a pump are of interest, whereas for experiments in which the pump-induced optical anisotropy was of interest, polarization spectroscopy was used. Many different but confusing names were also used by different authors to describe different (sometimes the same) experiments and added more confusion to the polarization related experiments.

I have tried to sort out the names and assign reasonable names for each experiment based on either the experimental technique or the source of the signals recorded. From the laser's point of view the double resonance experiments can be divided into two categories: *pumping* and *modulation*. In the pumping experiments the laser properties are kept constant, whereas in modulation experiments some characteristic of

the laser is switched on and off to record the difference. Modulation experiments are further divided into two categories: intensity modulation and polarization modulation. In intensity modulation the intensity (power) of the laser is modulated by a chopper or any other means, whereas in polarization modulation the polarization state of the laser is modulated by an electro-optic or an acousto-optic modulator. The polarization state of the laser used in either pumping or modulation can be either plane-polarized or circularly-polarized. Since a plane-polarized pump induces optical anisotropy^a as well as total population changes, we use the term *alignment pumping* when the optical anisotropy is of interest. Similarly, *orientation pumping* is used when the laser is circularly polarized. If the total population changes are of interest or if the source of the pump is not polarized, we have *population pumping*. Pumping experiments may be combined with a modulation technique to record the difference in absorption with and without pumping. In this case, a prefix *intensity modulated* will be added to the pumping experiment as e.g., *intensity modulated alignment pumping*. Similarly a plane- or circularly-polarized pump can be employed in polarization modulation experiments and we will call it alignment (orientation) modulation if a plane- (circularly-) polarized pump is used.

Based on the characteristics of the signals recorded, saturation absorption (population), linear dichroism, linear birefringence, circular dichroism, or circular birefringence measurement (or spectroscopy) seem to be useful names also. In many places, *polarization spectroscopy* was used to represent any of the polarization related experiments. Many of these definitions are mentioned repeatedly at various places in this thesis whenever they seem to be appropriate.

^aTerms such as alignment and orientation are described in Chapter 2.

II. Saturation Absorption Spectroscopy

A. Lineshape Problem in Saturation Absorption Spectroscopy

In spite of many years of effort, the present understanding of the line shapes observed in saturation spectroscopy is not complete. Even when collisions and power broadening are absent and long-lived states interact with a perfectly uniform beam with plane wave fronts, the line shapes remain more complex than expected. Numerous works have been published and others are still in progress. A list of problems and questions raised by Levenson²⁰ is quoted directly to show the complexity of the lineshape studies at the highest resolution (10 kHz).

The saturation resonances result from molecules emitting a photon in one direction and absorbing one propagating in the opposite direction. Either event can occur before the other, but the molecule recoils as the result of momentum transfer from the photon field. The result is a recoil splitting of the saturation resonance.

When the intensity of the interacting beams is not uniform or the wave fronts are not plane, transit time effects alter the line shape. Time-dependent and time-independent optical Stark shifts lead to asymmetries and reduce the recoil doublet splitting. Collisions cause pure dephasing and thus broaden the resonances, but they also alter molecular trajectories without damping the oscillations. Weak velocity changing collisions broaden the saturation resonances by increasing the width of the hole in velocity space. Strong velocity changing collisions remove molecules entirely from the resonant velocity groups thus adding a "lifetime" broadening. Finally, no laser is perfectly monochromatic.

What effect do the inevitable phase and amplitude glitches have on the ensemble? How much of its history does an ensemble remember? Could there perhaps be a better means of determining the center frequency of a Doppler-broadened transition than saturation spectroscopy?

Table 1.1: List of calculated coincidences between transitions in the ν_3 band of $^{12}\text{CH}_3\text{F}$ and CO_2 laser frequencies studied.

Transition ^a	Frequency ^b	Intensity ^c	Laser	Line	$\nu_l - \nu_o^d$
$^{\text{Q}}\text{Q}(12, 2)$	31383940.01	0.1027	$^{12}\text{C}^{18}\text{O}_2$	9P(20)	-39.60
$^{\text{Q}}\text{R}(11, 9)$	31998588.06	0.3658	$^{12}\text{C}^{18}\text{O}_2$	9P(22)	26.10
$^{\text{Q}}\text{R}(31, 4)$	32708074.10	0.1279	$^{12}\text{C}^{18}\text{O}_2$	9R(10)	22.30

^a Transition in the ν_3 band.

^b Transition frequency in MHz. Calculated from the constants in Ref. 25.

^c Calculated intensity.

^d Laser frequency minus calculated center frequency of the transition in MHz.

Constants for the laser frequency were taken from Ref. 26,27.

At Michigan State University we have been working on theories of three-level double resonance and collision-induced four-level double resonance lineshapes at resolutions of ~ 100 kHz. We now have theories and computer programs that can calculate double resonance lineshapes for all of our experimental conditions. Although the theories and programs are constantly being updated as new experimental observations are made, they now seem to agree with nearly all of the experimental observations.

I have carried out a series of studies of double-resonance effects in $^{12}\text{CH}_3\text{F}$ and $^{13}\text{CH}_3\text{F}$. The first of these studies was an analysis of transferred spikes in $^{12}\text{CH}_3\text{F}$. The main reason for undertaking a study of the normal species of methyl fluoride was our desire to attempt double resonance measurements in the $\nu_3 + \nu_6 \leftarrow \nu_6$ band, for which precise spectroscopic constants are available only for the C-12 species.²⁴ It seemed necessary to gain some experience with the strength of the double resonance effects in the stronger $2\nu_3 \leftarrow \nu_3$ band before attempting the more difficult measurements in the $\nu_3 + \nu_6 \leftarrow \nu_6$ band. In addition, the C-12 species has convenient coincidences between CO_2 laser lines and transitions in both the ortho species ($k = 3n$) and the para species ($k \neq 3n$). The familiar $^{\text{Q}}\text{Q}(12,2)$ transition has been used many times for infrared pumping for double resonance and far-infrared laser generation. But this work may be the first extensive use of the $^{\text{Q}}\text{R}(11,9)$ coincidence for infrared pumping. Details concerning the laser coincidences in $^{12}\text{CH}_3\text{F}$ are shown in Table 1.1.

The second part of this work is a more detailed study of the saturated absorption lineshapes in $^{13}\text{CH}_3\text{F}$ previously studied by Matsuo and Schwendeman.²⁸ Laser induced optical anisotropies and apparent splittings observed in the three- and four-level double resonance lineshapes are discussed.

B. Lineshape Study of Transferred Spikes in $^{12}\text{CH}_3\text{F}$

State-to-state collisionally-induced transitions between molecular levels are key ingredients of energy transfer between gas-phase molecules. Information about the rates and mechanisms of such transitions is necessary for quantitative characterization of interstellar chemistry, air pollution, ozone depletion, and global warming.²¹⁻²³ Among the methods that have been employed to study collisionally-induced transitions in the gas phase is the technique of four-level double resonance, pioneered in the microwave region by Oka and his coworkers²⁹⁻³¹ and subsequently extended to infrared-microwave³²⁻⁴⁴ and infrared-infrared double resonance.^{28,45-57} Infrared pumping has the advantage that substantial perturbations of the populations of the levels can be produced, in contrast to microwave pumping where the population changes are necessarily very small. Infrared probing also has an advantage in that Doppler effects at mid-infrared frequencies and above are many times larger than the homogeneous broadening for low-pressure gases. Therefore, four-level infrared-infrared double resonance can be used to obtain information about the changes in molecular velocity that accompany collisionally-induced transitions.^{28,45}

In recent communications from this laboratory the results of analyses of the lineshapes of transitions observed in infrared-infrared double resonance in $^{15}\text{NH}_3$ ⁴⁵ and $^{13}\text{CH}_3\text{F}$ ²⁸ were reported. The lineshapes were found to be adequately represented by the sum of two components, one of which is a Gaussian function whose center frequency and width are the expected center frequency and Doppler width of the transition, respectively. The second component is a nearly Doppler-free transferred spike whose lineshape is well-represented by a theoretical expression that was derived by assuming that the change in velocity of the molecules upon collision follows the

prediction of a collision kernel that is the sum of two of the kernels originally introduced by Keilson and Storer.⁵⁸ In the recent work, the double resonance experiments were carried out by pumping a single vibration-rotation transition in a fundamental band (ν_2 in $^{15}\text{NH}_3$ or ν_3 in $^{13}\text{CH}_3\text{F}$) by means of a single frequency CO_2 laser while scanning a single vibration-rotation transition in a hot band ($2\nu_2a \leftarrow \nu_2s$ in $^{15}\text{NH}_3$ ⁴⁵ or $2\nu_3 \leftarrow \nu_3$ in $^{13}\text{CH}_3\text{F}$ ²⁸) by means of an infrared-microwave sideband laser source. The advantage of this experimental arrangement is that as a result of the low rates of loss or gain of vibrational energy upon collision, the collisional effects involve almost entirely the effective transfer of population from the upper state of the pump transition to the lower state of the probe transition.

Two mechanisms were proposed to account for the double resonance lineshape. One mechanism assumes a near-resonant swapping of vibration-rotation energy between colliding molecules. In this case a molecule excited by the radiation returns to the ground state upon collision with a ground state molecule that becomes vibrationally excited. The net result is that a molecule in the upper state of the pumped transition becomes a ground state molecule while a molecule appears in a different rotational state of the excited vibrational state. This is effective population transfer from the upper state of the pump transition to another rotational state in the excited vibrational state. Since by this mechanism the molecule transferred is not the molecule pumped, the molecule probed should have a near thermal velocity distribution and give rise to a Gaussian lineshape with the expected Doppler width of the probe transition.

The second mechanism assumes that a molecule that was excited by the pump radiation undergoes one or more collision-induced rotational transitions to reach the lower state of the probe transition. If these transitions occur without much change in velocity, the double-resonance effect will be nearly Doppler-free and be centered near the center of the velocity group of the molecules pumped. It was found in this work, as had been determined earlier by theoretical calculations,^{59,60} that the collision kernel for such transitions can be well represented by a sum of two Keilson-Storer kernels,⁵⁸ a narrow one to describe the results of collisions with large impact parameter and a broader one to describe the results of collisions of small impact parameter. For

both ammonia and methyl fluoride, it was found that direct collisionally-induced transitions follow the $\Delta k = 3n$ ($n = 0$ or a positive or negative integer) selection rule discovered for C_{3v} symmetric tops by Oka³¹ many years ago. The $\Delta k = 0$ spikes were narrow and increased in width as $\Delta J = J_{probe} - J_{pump}$ increased. The $\Delta k = \pm 3$ and $\Delta k = \pm 6$ spikes were very broad, although still considerably narrower than the usual Doppler width. The widths of the transferred spikes and the resulting predicted r.m.s. change in velocity upon collision were reported for many transitions. The ratio of the area of the Gaussian to that of the transferred spikes was found to vary linearly with the inverse of the pressure and a rate constant theory was shown to account for this variation.⁴⁵

C. Lineshape Dependence on the Polarization

Double resonance lineshapes in saturation absorption spectroscopy have been studied in an attempt to understand optical pumping effects,⁶¹ collision dynamics,^{62,63} and relaxation paths of excited molecules^{28,45,64,65} and have been the subject of numerous papers.^{60,66-71}

At very high pump intensities, absorption and emission line-shape functions are changed by the optical frequency fields and a splitting is observed. Two different physical descriptions have been used to account for the splitting observed. The strong optical field of the pump radiation creates mixed eigenstates of molecular resonant transition and radiation. The new eigenstates are shifted in energy with respect to the radiation field, thereby causing a splitting in the observed lineshape. The amount of shift is called the Rabi frequency. There exist numbers of papers describing the physics and necessary conditions for this kind of splitting.^{19,72-78} Ingenious techniques dealing with this Rabi frequency and its application have resulted in fruitful measurements of related constants.⁷⁹⁻⁸¹ Both "AC Stark" effect and "optical Autler-Townes" effect were used to describe this phenomenon.

Another physical picture that can lead to the splitting (strictly speaking this should be called a dip rather than splitting) is called *velocity selective optical pumping* in which molecules in a selective velocity group in the ground state are pumped

to the second excited state by two-photon transitions. Since the population dip of the Bennett hole at the ground level also appears in the second excited level, scanning a probe which sees the difference in population between the second and the first excited level will lead to a dip at the center of the Bennett spike.^{82,61} The following arguments were added in proof to support this explanation; (1) velocity changing collisions destroy the splitting; (2) longer transit time creates bigger splitting; (3) certain time-delay is required to form the splitting; and (4) the experimental conditions are different from those required for the observation of the AC Stark effect.

III. Polarization Spectroscopy

Polarization spectroscopy¹ is an important variation of saturation spectroscopy, useful when the coupled energy levels are spatially degenerate. In polarization spectroscopy, the pump wave is polarized in such a way that it excites preferentially different components of transitions with equal frequency. As a result, the polarization state of the probe beam is altered by the anisotropy induced by the pump beam. The signal probed in polarization spectroscopy depends on the difference in absorption constants and/or refractive indices for the two polarization components of the probe beam. An important result is that the polarization signal shows a Doppler-free line profile. A detailed description of polarization spectroscopy is given in Chapter 2.

A slightly different type of polarization technique which is a combination of polarization spectroscopy¹ and lower level labeling⁸³ — *polarization labeling spectroscopy* — has been developed to simplify complex spectra.⁸⁴ A circularly polarized pump wave is tuned to a transition. Circular dichroism and birefringence appears on transitions coupled to the one that is pumped. This anisotropy is usually detected using a linearly polarized probe and a crossed (or nearly crossed) polarizer before the detector. Polarization labeling has been used successfully to simplify the spectra and identify the origin of transitions in Na₂,⁸⁵ in Cs₂,⁸⁶ and Li₂.^{87,88}

It is well known that polarized laser radiation can create spatially oriented molecules.⁸⁹ Consideration of this polarization on the lineshape has been the subject of many papers.^{60,66-69,90} Bain and McCaffery⁹¹⁻⁹⁴ derived expressions for laser

fluorescence polarization following excitation by linear or circularly polarized light. Aminoff^{95,96} calculated the velocity selective optical pumping (VSOP) line shape including collision effects. Nakayama⁹⁷⁻¹⁰¹ dealt with linear and circular optical anisotropies induced in polarization, VSOP, and saturation spectroscopy. Gawlik et al.^{102,103} reported observation of a splitting of the Na D1 line is the result of the nonstationary effect in velocity-selective optical pumping. Kim et al.¹⁰⁴ observed a polarization-modulated optical signal of Na. All of this work involved electronic transitions in atoms or simple diatomic molecules. This thesis presents the first report of polarization effects in vibration-rotation spectroscopy.

IV. Time Resolved Spectroscopy

Although a number of time-resolved experiments have been extensively used to study relaxation processes,^{55,105-115} there still remain questions to be answered at the level of sub-Doppler resolution. From the sub-Doppler infrared-infrared double resonance lineshape experiments described in this thesis and those performed previously,^{28,45} we learned that there exist at least three collisional relaxation processes in pure gaseous samples. The three processes have distinct selection rules and relaxation rates, therefore contributing to different portions of the observed lineshape;

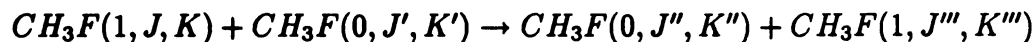
1. $\Delta J = \pm n, \Delta K = 0$; sharp spike



2. $\Delta J = \pm n, \Delta k = 3n$; broad spike



3. vibrational swapping; Gaussian



It is still an unresolved question whether the sharp spikes observed at levels for which n is large are the result of a series of consecutive $\Delta J = 1$ collisions or a single or a few $\Delta J = n$ collisions.

According to microwave-microwave double-resonance experiments, when the equilibrium population of molecules in the ground vibrational state is disturbed, as by interaction with powerful microwave radiation, there are selection rules governing the collisionally-induced rotational energy transfer that leads to a return to equilibrium.³¹ The strongest of these selection rules for molecules of C_{3v} symmetry is that upon collision the ortho ($k = 3n$ in vibrational states of A symmetry, where n is a positive or negative integer) or para ($k \neq 3n$) symmetry of a molecule is unchanged. There is good theoretical reason for this finding, based on the difficulty of changing the nuclear spin state of a molecule as a result of collision.³¹

Evidence for this ortho \leftrightarrow para selection rule in excited vibrational states of C_{3v} molecules has been obtained by Harradine *et al.* in CDF_3 ⁵² and from this laboratory in $^{15}NH_3$,⁴⁵ $^{13}CH_3F$ ²⁸ and in the present work. As still further evidence for a $\Delta k = 3n$ rule, it has been shown that it is possible to make a partial ortho-para separation in a sample of $^{13}CH_3F$ molecules by the technique of light-induced drift in which a vibration-rotation transition is irradiated slightly off resonance by a moderately strong infrared laser.¹¹⁶⁻¹²⁰ The ortho-para separation requires that molecules retain their symmetry after many collisions.

Chapter 2

Theory

General understanding of the broadening mechanisms in the spectral line is necessary to understand saturation absorption spectroscopy or polarization spectroscopy. In the first section of this chapter, a variety of line broadening mechanisms are discussed. Then, definitions such as a laser burned hole (*Bennett hole*), polarization, alignment, orientation, and a few related theories are discussed in subsequent sections.

I. Line Broadening

The interaction of a molecule with a radiation field does not occur at the single sharp frequency Ω^a , but is instead broadened by a variety of mechanisms to give a resonance line shape with some finite width Ω_w . *Homogeneous* or Lorentzian broadening gives rise to a line shape of the form

$$\alpha(\omega) = \alpha_o \frac{\Omega_w^2}{(\omega - \Omega)^2 + \Omega_w^2} \quad (2.1)$$

where α_o, ω, Ω , and Ω_w are the peak absorption intensity, probe beam frequency, transition center frequency, and half-width at half-maximum (HWHM), respectively. Lorentzian broadening arises from radiative decay (*natural* broadening), collisions, or power-broadening resulting from saturation by high-intensity radiation.

^aIn this thesis Ω is used for a fixed frequency related value whereas ω is used for variable frequency.

Inhomogeneous broadening, arising from a distribution of resonant frequencies in an ensemble of molecules, generally has a Gaussian line shape:

$$\alpha(\omega) = \alpha_o \exp^{-\ln 2 \frac{(\omega - \Omega)^2}{\Omega_D^2}} \quad (2.2)$$

In this inhomogeneously broadened line shape, different molecules are responsible for different portions of the absorption line. The absorption frequencies, however, are the same in the rest frame of each molecule. In gas-phase molecules with a Maxwell-Boltzmann velocity distribution, molecules moving away from a light source with a velocity component v absorb a frequency below that absorbed by stationary molecules due to the Doppler effect.

$$\omega(v) = \omega_o(1 - v/c)$$

where $\omega(v)$, ω_o , and c are the frequency felt by the molecule, the radiation frequency, and the speed of the light, respectively. The HWHM caused by this Doppler effect is

$$\Omega_D = \Omega/c \sqrt{2kT \ln 2 / M} = 3.58 \times 10^{-7} \Omega \sqrt{T/M} \quad (2.3)$$

Here T is the absolute translational temperature of the molecules and M is the molar mass in atomic mass units.

An important difference between the two broadening mechanisms is in their response to high-intensity radiation. A monochromatic radiation source can saturate only a particular velocity group of molecules, leaving the rest unaffected; it is thus possible to “burn a hole” into a Doppler line profile. A homogeneous line, on the other hand, is uniformly affected by pumping at any point along the line shape. In this case, the effect of monochromatic pumping is to “bleach” the entire line rather than to burn a hole.

II. Creation and Detection of Bennett Holes

If one laser (the pump laser) is used to burn a hole in an inhomogeneously broadened absorption line, a second (probe) laser scanned across the absorption will detect a profile similar to Figure 2.1 – an absorption line with a hole in it. Modulating the

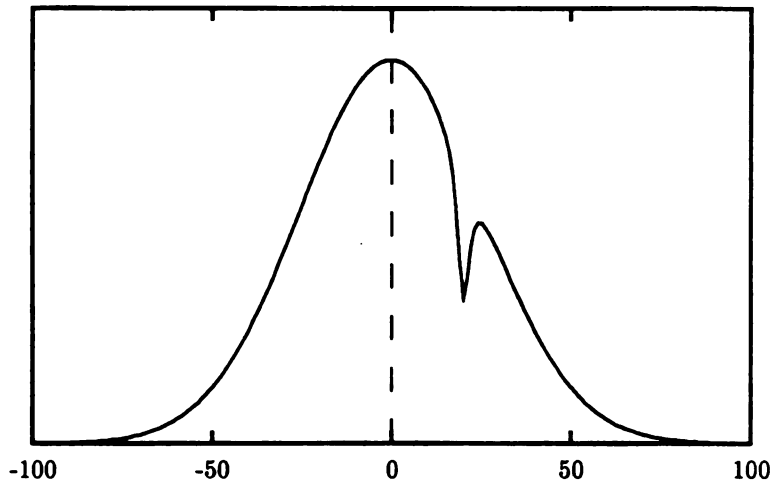


Figure 2.1: A typical absorption line shape with a Bennett hole. The X -axis is frequency in units of MHz. Y -axis is the absorption intensity. The line shape was simulated with a Gaussian of 30 MHz HWHM and a Lorentzian of 1 MHz HWHM.

pump laser or employing polarization techniques can separate the effect of the hole from that of the rest of the line, yielding the narrow profile in Figure 2.2.

In the most common saturation spectroscopy geometry, two counter-propagating waves of the same frequency,

$$E(t) = \frac{1}{2} \{ E_s e^{-i(\omega t + kv)} + E_p e^{-i(\omega t - kv)} \} \quad (2.4)$$

interact with an inhomogeneously broadened absorption line. If the saturating pump wave (E_p) is much stronger than the probe amplitude (E_s), the absorption and dispersion at the probe frequency can be calculated rather simply. In the steady state, the effect of the pump beam on the population difference is given by,

$$\rho_{aa}(v) - \rho_{bb}(v) = \left[1 - \frac{|x_s|^2 \gamma_2 / \gamma_1}{(\Omega - \omega + kv)^2 + \gamma_2^2 + |x_s|^2 \gamma_2 / \gamma_1} \right] (\rho_{aa}^0 - \rho_{bb}^0) \quad (2.5)$$

In this equation $\rho_{aa}(v)$, $\rho_{bb}(v)$ are the populations of the levels a and b , respectively ($E_a < E_b$) and v is the axial velocity of molecules in the positive y direction. Ω , ω , k , x_s , γ_1 , and γ_2 are the center frequency of the transition, probing laser

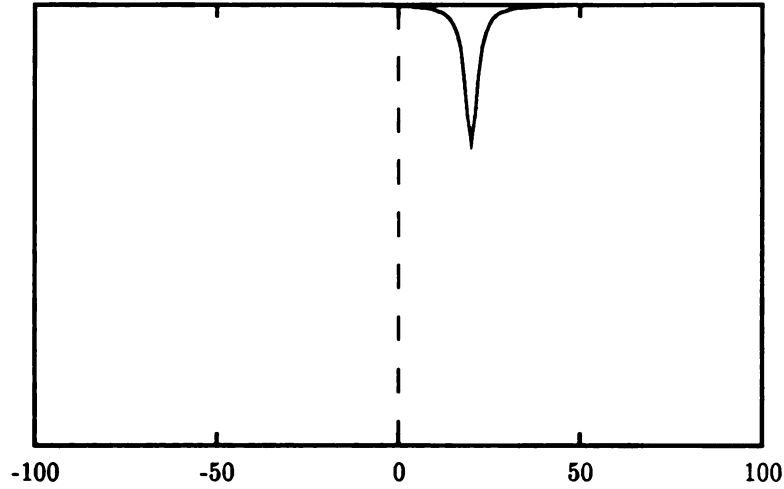


Figure 2.2: A typical double resonance absorption line shape with a modulated pump beam. The X -axis is frequency in units of MHz. Y -axis is the absorption intensity. The lineshape is Lorentzian of 1 MHz HWHM.

frequency, magnitude of the wave vector, Rabi frequency of the saturating beam, population relaxation rate, and coherence relaxation rate, respectively. For molecules moving with axial velocity v in the positive Y direction, the detuning from the pump frequency is

$$\Delta = \Omega - \omega + kv$$

and the Rabi frequency of the saturating laser is

$$x_s = \mu_{ab} \cdot E_s / \hbar$$

where E_s is the electric field of the saturating laser. All of the terms have been written here in circular frequency units, but ω has been used instead of ν to clearly distinguish from velocity v .

III. Lineshape Study of Transferred Spikes

The lineshapes of the three-level double resonance spectra were fitted by least squares to a theoretical lineshape that was calculated by solving the density matrix equations for a three-level system (the algebraic solution reported in Ref. 121,11 was used). The three-level fitting program includes provision for summation over the projection of the angular momentum ($m\hbar$) along the space-fixed axis and for numerical integration over the component of velocity in the direction of the radiation. The program also accommodates either co-propagating or counter-propagating geometry and all four of the possible arrangements of energy levels for three-level double resonance. For the summation over m states, the program assumes that the only effect of changing the radiant power of the probe beam is to change the overall intensity. Thus, as shown in the Appendix, only one three-level calculation is required for each possible m if the space-fixed Z axis is assumed to be parallel to the electric field of the pump radiation. Details concerning the three-level calculation and some results are given in Ref. 11. The fitting routine adjusts the center frequency of the probe transition, the vibrational contribution to the Rabi frequency, the relaxation rates for the populations and coherence, the overall amplitude, and the background of the spectrum to provide a best least-squares fit to the observed spectrum.

The lineshapes of the four-level double resonance spectra were fit by least squares to a theoretical lineshape that was derived in Ref. 45. In that work, however, only the shape and not the overall amplitude of the lineshape was derived. In this work, in order to lay the foundation for more careful intensity and lineshape studies, we rederive the four-level lineshape equations. The theoretical relations necessary for comparative intensity measurements are given in the Appendix where it is shown that the spectrometer output for four-level double resonance is

$$\Delta S_4 = C\nu_o S_{Jk} \Delta \bar{d}'_{ba} \quad (2.6)$$

in which

$$C = GI_o l \left(\frac{16\pi^2 \mu_v^2 N}{hc} \right). \quad (2.7)$$

In the Appendix, Eq.(A14), it is shown that the constant C may be determined by analysis of the lineshape of a three-level double resonance recorded under the same conditions as the four-level lineshape. In Equations (2.6) and (2.7),

ΔS_4 = the spectrometer output with the pump beam on minus the output with the pump beam off;

ν_o = the center frequency of the probe transition;

S_{Jk} = the linestrength of the probe transition for plane-polarized radiation summed over the space-fixed axis m components (expressions for S_{Jk} are given in Eq.(A11));

G = the spectrometer gain factor;

I_o = the intensity of the incident probe beam;

l = the absorption path length;

N = the number of absorbing molecules per unit volume in the lower level of the pump transition;

μ_v = the vibrational contribution to the transition dipole moment for $v = 2 \leftarrow 1$.

Finally, $\Delta \bar{d}_{ba}''$, the integral of the difference in the reduced value of the imaginary part of the off-diagonal density matrix element over the velocity in the direction of the probe beam for the probe transition, is taken to be the usual low power ($x_{ba} \ll \gamma_2$) expression for a two-level lineshape,

$$\Delta \bar{d}_{ba}'' = \int_{-\infty}^{\infty} \frac{\Delta d_{ba}''}{x_{ba}} dv_y = \frac{\gamma_2}{2} \int_{-\infty}^{\infty} \frac{(\Delta \rho_{aa}(v_y) - \Delta \rho_{bb}(v_y))}{(\nu - \nu_o - kv_y)^2 + \gamma_2^2} dv_y \quad (2.8)$$

Here, $x_{ba} = \mu_{ba} E^o / h$, where μ_{ba} is the transition moment for the probe beam; E^o is the probe beam electric field; γ_2 is the coherence relaxation rate for the probe transition; ν and k are the frequency and the magnitude of the wave vector for the probe beam, respectively; and $N \Delta \rho_{aa}(v_y) dv_y$ and $N \Delta \rho_{bb}(v_y) dv_y$ are the pump on minus pump off populations for the lower and upper levels, respectively, of the probe transition for molecules with velocity component in the direction of the probe beam between v_y and $v_y + dv_y$.

To simplify Eq.(2.8) we make two assumptions. First, we assume that the pump modulation rate is too fast for vibrational relaxation, so that $\Delta \rho_{bb}$ is negligible if level

b is in $v = 2$. Then, we assume that the spectral width of $\Delta\rho_{aa}$ is large compared to γ_2 so that $\Delta\rho_{aa}$ may be removed from the integral to give

$$\Delta\bar{d}'_{ba} = \pi\Delta\rho_{aa}([\nu - \nu_o]/k)/2k. \quad (2.9)$$

To obtain an expression for $\Delta\rho_{aa}$ we write rate equations for $\dot{\rho}_{aa} = d\rho_{aa}/dt$ and $\dot{\rho}_{nn} = d\rho_{nn}/dt$ in which level n is another rotational level in $v = 1$.

$$\dot{\rho}_{aa} = -A_{aa}\rho_{aa} + A_{ae}\rho_{ee} + \sum_n A_{an}\rho_{nn} \quad (2.10)$$

$$\dot{\rho}_{nn} = -A_{nn}\rho_{nn} + A_{na}\rho_{aa} + A_{ne}\rho_{ee} + \sum_{n' \neq n} A_{nn'}\rho_{n'n'} \quad (2.11)$$

In these expressions, level e is the upper level of the pump transition and the A_{ii} are scalar rate constants, but the A_{ij} for $i \neq j$ are integral operators, so that for example,

$$A_{an}\rho_{nn} = \int_{-\infty}^{\infty} A_{an}(v_y, v'_y)\rho_{nn}(v'_y)dv'_y. \quad (2.12)$$

In the steady state, the time derivatives vanish, so that

$$\rho_{aa} = A_{aa}^{-1} \left[A_{ae}\rho_{ee} + \sum_n A_{an}\rho_{nn} \right] \quad (2.13)$$

and

$$\rho_{nn} = A_{nn}^{-1} \left[A_{na}\rho_{aa} + A_{ne}\rho_{ee} + \sum_{n' \neq n} A_{nn'}\rho_{n'n'} \right]. \quad (2.14)$$

After substitution from Eq. (2.14) into Eq. (2.13),

$$\rho_{aa} = A_{aa}^{-1} \left\{ \left[A_{ae} + \sum_n A_{nn}^{-1} A_{an} A_{ne} \right] \rho_{ee} + \sum_n A_{nn}^{-1} A_{an} A_{na} \rho_{aa} + \sum_{n \neq n'} A_{nn}^{-1} A_{an} A_{nn'} \rho_{n'n'} \right\}. \quad (2.15)$$

This process can obviously be repeated indefinitely, but, for simplicity of writing, we choose to stop the iteration after one more collision by using, on the right-hand side of Eqs. (2.13) and (2.14), the approximations,

$$\rho_{aa} \cong A_{aa}^{-1} A_{ae} \rho_{ee} \quad (2.16)$$

and

$$\rho_{n'n'} \cong A_{n'n'}^{-1} A_{n'e} \rho_{ee}, \quad (2.17)$$

in which case

$$\rho_{aa} = \bar{A}_{ae}\rho_{ee}, \quad (2.18)$$

where the effective collision kernel \bar{A}_{ae} is

$$\bar{A}_{ae} = A_{aa}^{-1} \left\{ A_{ae} + \sum_n A_{an} A_{nn}^{-1} \left[A_{ne} + A_{na} A_{aa}^{-1} A_{ae} + \sum_{n' \neq n} A_{nn'} A_{n'n}^{-1} A_{n'e} \right] \right\}. \quad (2.19)$$

The products of operators are defined such that, for example,

$$\begin{aligned} A_{aa}^{-1} A_{an} A_{nn}^{-1} A_{nn'} A_{n'n}^{-1} A_{n'e} (v_y, v'_y) = \\ \frac{1}{A_{aa} A_{nn} A_{n'n'}} \iint A_{an}(v_y, v''_y) A_{nn'}(v''_y, v'''_y) A_{n'e}(v'''_y, v'_y) dv''_y dv'''_y. \end{aligned} \quad (2.20)$$

The effective collision kernel \bar{A}_{ae} may in principal be calculated from extensive information about the potential functions for collisional interactions. We choose to try to express \bar{A}_{ae} as a sum of simple collision kernels of the form introduced by Keilson and Storer.⁵⁸ To this end we write

$$\begin{aligned} \bar{A}_{ae}(v_y, v'_y) &= \sum_i A_i(v_y, v'_y) \\ &= \sum_i (A_i^\circ / \sqrt{\pi} \beta) e^{-(v_y - \alpha_i v'_y)^2 / \beta_i^2} \end{aligned} \quad (2.21)$$

where $\alpha_i = (1 - \beta_i^2 / u^2)^{1/2}$ in which $u^2 = 2k_B T / m$ with k_B the Boltzman constant, T the absolute temperature, and m the molecular mass. The constant β_i determines the velocity-changing effect of the collisions. For collisions defined by a single kernel A_i , $\beta_i / \sqrt{2}$ may be shown to be the *r.m.s.* change in velocity upon collision.⁵⁸

We show evidence below that in CH_3F the lineshapes of the collision-induced double resonance may be satisfactorily represented as a sum of three terms of the form in Eq.(16). In one of these terms β_i is the limiting value, $\beta_i = u$, in which case $\alpha_i = 0$. This term is interpreted below as arising from collisionally-induced vibrational energy swapping ($V - V$ transfer) in which a vibrationally-excited molecule exchanges vibrational energy upon collision with a ground state molecule.

With the representation just given for \bar{A}_{ae} ,

$$\Delta \rho_{aa} = \sum_i (A_i^\circ / \sqrt{\pi} \beta) \int_{-\infty}^{\infty} e^{-(v_y - \alpha_i v'_y)^2 / \beta_i^2} \Delta \rho_{ee}(v'_y) dv'_y, \quad (2.22)$$

in which $\Delta\rho_{ee}(v_y)$ is the pump on minus pump off difference in the population of the upper level of the pump transition for v_y between v_y and $v_y + dv_y$. For this quantity, we use the usual saturation formula for two levels with m degeneracy,

$$\Delta\rho_{ee}(v_y) = \frac{(1-b)}{2\sqrt{\pi}u} \sum_m \frac{(\gamma_2/\gamma_1)x_m^2 e^{(-v_y/u)^2}}{(\nu_p - \nu_{op} + k_p v_y)^2 + \gamma_2^2 + (\gamma_2/\gamma_1)x_m^2}. \quad (2.23)$$

In this expression, $b = \exp(-h\nu_{op}/k_B T)$ is the Boltzmann factor for the upper state of the pump transition whose center frequency is ν_{op} ; γ_1 and γ_2 are population and coherence relaxation rates, respectively, for the pump transition; ν_p and k_p are the fixed frequency and the magnitude of the wave vector of the pump laser; and x_m is the Rabi frequency for the m component of the pump transition. We assume $\Delta m = 0$ selection rules for the pump, so that

$$x_m = (E_p^\circ/h)(\partial\mu/\partial Q)_e \langle 0|Q|1 \rangle \langle J'km|\Phi_{Zz}|Jkm \rangle \quad (2.24)$$

in which Φ_{Zz} is the direction cosine between the space-fixed direction of the electric field E_p° of the pump radiation and the molecule-fixed symmetry axis. The induced population $\Delta\rho_{ee}$ is calculated at intervals in v_y and the integral in Eq.(2.22) is performed numerically.

If both sides of Eq.(2.22) are integrated over v_y , it is found that

$$\Delta\bar{\rho}_{aa} = \sum_{i=1}^3 \bar{\rho}_{aa}^{(i)} \quad (2.25)$$

in which $\Delta\bar{\rho}_{aa}$ is the total relative pumped population of level a , the lower level of the probe transition, and

$$\bar{\rho}_{aa}^{(i)} = A_i^\circ \Delta\bar{\rho}_{ee} \quad (2.26)$$

in which $\Delta\bar{\rho}_{ee}$ is the total relative pumped population of level e , the upper level of the pump transition. Thus, A_i° is the ratio of the population of molecules that reached state a by the i th mechanism to the total pumped population of molecules in state e .

By recasting Eq.(5),(6), and (8)–(14) in terms of rate constants for the total population, irrespective of velocity, an interpretation may be given for the A_i° in terms of ratios of rate constants. Thus, if γ_{nn} is the rate constant for loss of population from

state n and γ_{mn} is the corresponding constant for collisionally-induced transitions from state n to state m ,

$$\dot{\bar{\rho}}_{aa} = -\gamma_{aa}\bar{\rho}_{aa} + \gamma_{ae}\bar{\rho}_{ee} + \sum_n \gamma_{an}\bar{\rho}_{nn} \quad (2.27)$$

and

$$\dot{\bar{\rho}}_{nn} = -\gamma_{nn}\bar{\rho}_{nn} + \gamma_{na}\bar{\rho}_{aa} + \gamma_{ne}\bar{\rho}_{ee} + \sum_{n' \neq n} \gamma_{nn'}\bar{\rho}_{n'n'}. \quad (2.28)$$

Manipulation of the γ 's in much the same way as the collision kernels earlier leads to the result,

$$\bar{\rho}_{aa} = \frac{\bar{\gamma}_{ae}}{\gamma_{aa}} \bar{\rho}_{ee} \quad (2.29)$$

in which

$$\bar{\gamma}_{ae} = \gamma_{ae} + \sum_n \gamma_{an}\gamma_{nn}^{-1} \left[\gamma_{ne} + \gamma_{na}\gamma_{aa}^{-1}\gamma_{ae} + \sum_{n' \neq n} \gamma_{nn'}\gamma_{n'n'}^{-1}\gamma_{n'e} \right]. \quad (2.30)$$

Clearly, $\bar{\rho}_{aa}/\bar{\rho}_{ee}$ is the ratio of the effective rate constant for transitions into state a from state e , with any number of intermediate states, to the total effective rate constant for loss of population from state a by any mechanism. Comparison of Eq.(2.29) to Eq.(2.18) and consideration of Eq.(2.25) and (2.26) then shows that A_i^a may be viewed as the ratio of the effective rate constant for transitions from state e to state a by mechanism i to the total effective rate constant for loss of population from state a by any mechanism.

IV. M Selection Rules

The M quantum numbers are associated only with the $e^{\pm iM\phi}$ dependence of the wave functions in the integral

$$\int \int \int \psi_{nIM}^*(r, \theta, \phi) \vec{\mu} \cdot \vec{E} \psi_{n'I'M'}(r, \theta, \phi) r^2 dr \sin \theta d\theta d\phi \quad (2.31)$$

where $\vec{\mu} = r \sin \theta \cos \phi \vec{x} + r \sin \theta \sin \phi \vec{y} + r \cos \theta \vec{z}$. The three components of the electric dipole moment can be associated with three polarizations of the light wave. If the

Table 2.1: M selection rules for various polarizations states of laser. It should be noted that the laser propagates along the Y axis and the reference plane is $YZ(\pi)$.

Polarization	ΔM
σ^\pm	± 1
π	0
σ^-	-1
σ^+	+1

incoming radiation is linearly polarized, $\vec{E} = E\vec{z}$, with the electric vector coincident with the z axis defined, then there is no ϕ dependence in the $\vec{\mu} \cdot \vec{E}$ part of the integral and $M' = M$ in order for the integral to be nonzero. Therefore the selection rule is $\Delta M = 0$ for a π polarized light. For right circularly polarized light (σ^+) where $\vec{E} = E(\vec{x} + i\vec{y})$, the dot product is

$$\vec{\mu} \cdot \vec{E} = rE \sin \theta (\cos \phi + i \sin \phi) = r \sin \theta e^{i\phi} \quad (2.32)$$

and the integral

$$\int e^{iM\phi} e^{+i\phi} e^{-iM'\phi} d\phi \quad (2.33)$$

is nonzero only if $M - M' = -1$, so that $\Delta M = +1$; similarly, for left circularly polarized light (σ^-), $\Delta M = -1$. For σ^\pm linearly polarized light obviously the selection rule is $\Delta M = \pm 1$. Table 2.1 summarizes the M selection rules for different polarization states.

V. Alignment and Orientation

When a single rotational level in an array of molecules is excited by highly polarized laser radiation, a non-uniform distribution of M states is created. The polarization of such an array may be completely described in terms of the spherical tensor moments (or state moments), ${}^{JJ}\rho_Q^K$, of the density matrix. If the space-fixed z axis is chosen as the symmetry axis, only the $Q = 0$ components of ${}^{JJ}\rho_Q^K$ survive, and the density matrix becomes diagonal and thus the state moments can be related to the occupation numbers of individual m levels. The three tensor moments of relevance

in single photon experiments are the population, ${}^{JJ}\rho_0^0$, the orientation, ${}^{JJ}\rho_0^1$, and the alignment, ${}^{JJ}\rho_0^2$.^{91-94,122} They are related to the individual density matrix elements by:

$${}^{JJ}\rho_0^K = \sum_M \begin{pmatrix} J & J & K \\ M & -M & 0 \end{pmatrix} {}^{JJ}\rho_{MM} \quad (2.34)$$

in which $\begin{pmatrix} J & J & K \\ M & -M & 0 \end{pmatrix}$ is the $3j$ symbol.

Molecules pumped by a polarized laser are aligned or oriented depending on the polarization of the laser. A typical double resonance technique utilizes two linearly polarized lasers which are orthogonal to each other. If a plane polarized pump excites the $R(0)$ transition shown in Figure 2.3, for example, it creates an unequal population of the $|M|$ levels in the excited M degenerate state. This unequal population distribution in $|M|$ sublevels is called *alignment*. It should be noted that the alignment created by a parallel pump (continuous line in (a), $\Delta M = 0$) is different from another alignment created by a perpendicular pump (dash line, $\Delta M = \pm 1$). If a circularly polarized light is used for pumping, the selection rule is $\Delta M = +1$ for right-circularly polarized (σ^+) pump and $\Delta M = -1$ for left-circularly polarized (σ^-) pump.

The unequal population of M sublevels in this case is called *orientation*. *Alignment modulation* is used to describe experiments where only the alignment of samples are modulated while the total population is kept constant whereas *orientation modulation* is used when only the orientation of molecules is changed. Aligned samples are polarized since the populations of different $|M|$ levels are unequal. In addition an oriented sample is magnetized because the population of $+M$ and of $-M$ are different. Figure 2.3 and Table 2.1 show the different M selection rules under different conditions of the polarization state of the pump.

VI. Absorption and Dispersion

When an electromagnetic wave passes through a medium with refractive index n , not only the *wave amplitude* decreases (absorption) but also the *phase velocity* changes from its value c in vacuum to $v = c/n$ (dispersion). The refractive index n depends

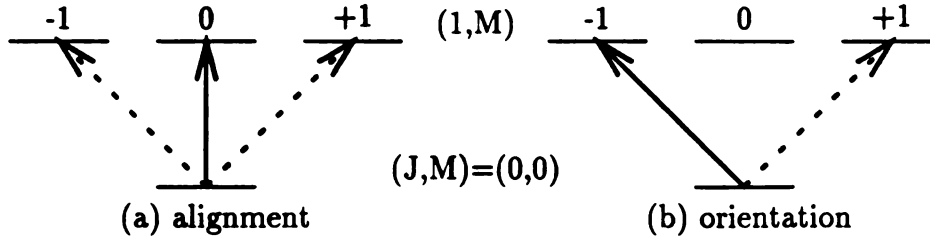


Figure 2.3: Alignment and orientation created by polarized lasers. In (a) the dashed lines are for YX plane polarized light (σ^\pm) whereas the continuous line is for YZ plane polarized light (π). In (b) the dashed and continuous lines are for right- (σ^+) and left- (σ^-) circularly polarized pump radiation, respectively.

on the frequency ω of the electromagnetic wave and is related to the absorption by the Kramers-Kronig relationships;

$$n(\omega) = -\frac{1}{\pi} \int_{-\infty}^{\infty} \frac{\alpha(\omega')}{\omega' - \omega} d\omega' \quad (2.35)$$

$$\alpha(\omega) = \frac{1}{\pi} \int_{-\infty}^{\infty} \frac{n(\omega')}{\omega' - \omega} d\omega'. \quad (2.36)$$

A homogeneously broadened absorption lineshape is a Lorentzian whereas a dispersion lineshape can be obtained for $n(\omega)$.

VII. Optical Anisotropy

There are two kinds of optical anisotropy: circular and linear. Circular optical anisotropy consists of circular dichroism ($\Delta\alpha_C = \alpha^+ - \alpha^-$) and birefringence ($\Delta n_C = n^+ - n^-$), which are differences in the absorption coefficient and the refractive index, respectively, between right- (σ^+) and left- (σ^-) circularly polarized beams, respectively. Linear optical anisotropy consists of linear dichroism ($\Delta\alpha_L = \alpha^{\sigma^\pm} - \alpha^\pi$) and birefringence ($\Delta n_L = n^{\sigma^\pm} - n^\pi$), which are differences in the absorption coefficient and the refractive index, respectively, between two linearly (σ_\pm and π) polarized beams whose polarization planes are perpendicular to each other. Isotropic samples may exhibit linear or circular optical anisotropy when excited by a plane-polarized laser or by a circularly-polarized laser, respectively. Aligned samples created by a plane polarized pump laser show linear dichroism (LD) and/or linear birefringence

(LB) whereas oriented samples created by a circularly polarized pump have circular dichroism (CD) and/or circular birefringence (CB).

A. Saturation Absorption Spectroscopy

In saturation absorption spectroscopy where a plane polarized pump (π) and probe (either σ^\pm or π) are used, the signal from the laser induced optical anisotropy is relatively small compared with the signal from the total population changes and is usually hidden behind the strong signal. Nevertheless, the laser induced optical anisotropy (alignment in this case) can be observed by comparing the lineshapes of a three-level double resonance under different pump and probe configurations (shown in Figure 2.4).

Even though most double resonance experiments are result of a saturation effect “saturation absorption” has been used for experiments involving two plane polarized lasers for historical reasons. Since the pump laser is mechanically chopped in these experiments in order to record only the double resonance effects, we refer to these experiments either as *intensity modulation* or *population modulation* when only the total population changes are of interest or as *intensity modulated alignment pumping* when our interest is in the linear anisotropy induced by the laser.

B. Alignment Modulation vs. Orientation Modulation

Instead of the two separate measurements done in the alignment pumping with parallel and perpendicular configurations, the polarization state of the pump (either pump or probe but not both) can be modulated between π and σ^\pm and the laser induced optical anisotropy can be directly measured. Since modulating polarization states of the pump results in changes in the orientation as shown in Figure 2.3-(a), this is called *alignment modulation* to distinguish from *orientation modulation* where the polarization state of the pump is modulated between σ^+ and σ^- . In alignment modulation, $\alpha_L = \alpha^\pi - \alpha^{\sigma^\pm}$ is recorded using a linearly polarized probe whereas in orientation modulation $\alpha_C = \alpha^+ - \alpha^-$ is measured with a circularly polarized probe.

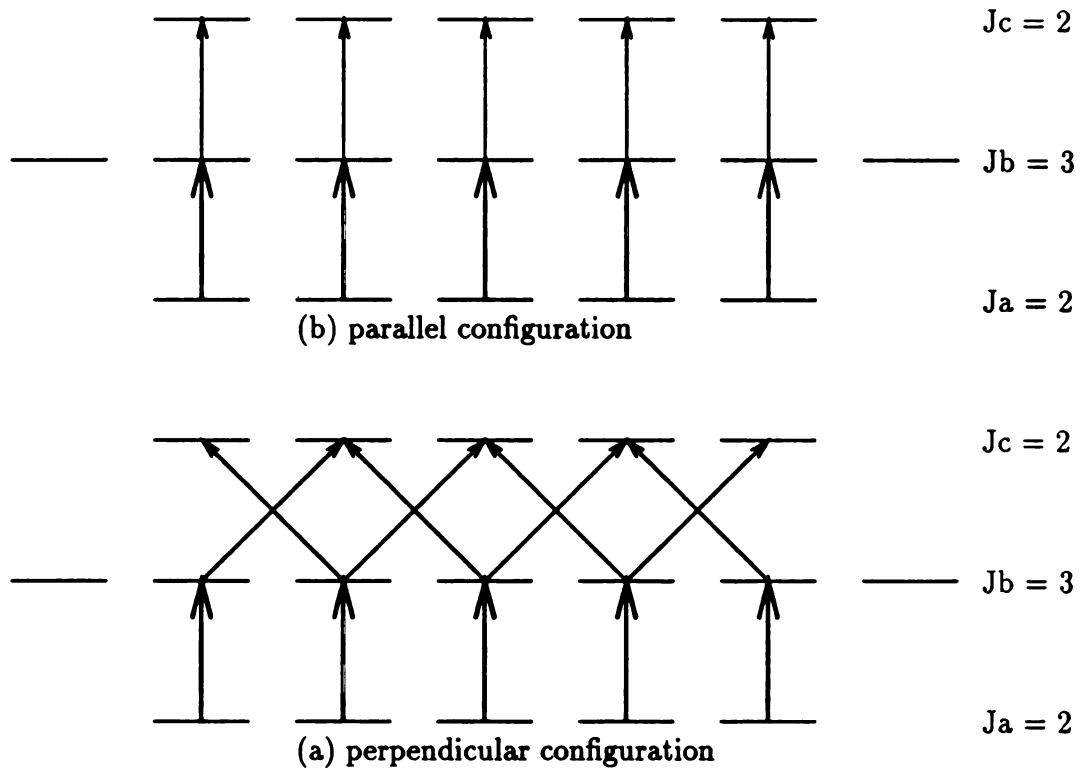


Figure 2.4: Two different saturation absorption configurations: (a) π pump, π probe; (b) π pump, σ^\pm probe. It should be noted that the selection of π is arbitrary, since there is no field applied to the sample. At some places the π and the σ^\pm is interchanged for the convenience of explanation or calculation. Exchanging the π and the σ^\pm should give the same result.

At some places in this thesis *polarization modulation* is used to represent either alignment modulation or orientation modulation, or both to differentiate from *intensity modulation* in which the intensity of the pump laser is modulated. Nakayama¹⁰¹ used the term *velocity selective optical pumping* for the alignment modulation described here.

VIII. Polarization Spectroscopy

Historically, *polarization spectroscopy* has been used for experiments in which laser induced optical anisotropy is recorded. In typical polarization spectroscopy, a circularly polarized pump beam induces a circular dichroism and birefringence to a sample and the detector sees a plane polarized probe beam through an analyzing polarizer rotated perpendicular to the incident probe polarization.

The qualitative theory for polarization spectroscopy and measurement of circular birefringence is presented here following similar derivations by Demtroder.¹⁶ A right circularly polarized (σ^+) laser beam excites molecules following a $\Delta M = +1$ selection rule, producing a nonuniform population of the M sublevels, which is equivalent to an anisotropic distribution for the orientations of the angular momentum vector J . Such an anisotropic sample becomes birefringent for the incident linearly polarized (σ^\pm) probe beam, and the plane of polarization is slightly rotated. Since a linearly polarized probe wave^b

(2.37)

can be always composed of a right and a left circularly polarized component, $\vec{E}^\pm = \vec{E}^+ + \vec{E}^-$ where

$$\vec{E}^+ = \frac{1}{2}(E_{ox}\vec{x} + iE_{oz}\vec{z})e^{i(\omega t - ky)} \quad (2.38)$$

$$\vec{E}^- = \frac{1}{2}(E_{ox}\vec{x} - iE_{oz}\vec{z})e^{i(\omega t - ky)} \quad (2.39)$$

^bIn this section ω is in angular frequency.

where \vec{x}, \vec{y} , and \vec{z} are unit vectors along x, y , and z direction, respectively. After passing a sample cell of length L the two components are

$$\vec{E}^+ = \vec{E}_o^+ e^{i(\omega t - k^+ L)} e^{-\alpha^+ L}; \quad \vec{E}_o^+ = \frac{E_{ox} \vec{x} + i E_{oz} \vec{z}}{2} \quad (2.40)$$

$$\vec{E}^- = \vec{E}_o^- e^{i(\omega t - k^- L)} e^{-\alpha^- L}; \quad \vec{E}_o^- = \frac{E_{ox} \vec{x} - i E_{oz} \vec{z}}{2}. \quad (2.41)$$

Due to the differences $\Delta n = n^+ - n^-$ and $\Delta \alpha = \alpha^+ - \alpha^-$ caused by the anisotropic saturation, a phase difference

$$\Delta \phi = (k^+ - k^-) L = (\omega L / c)(n^+ - n^-) \quad (2.42)$$

and a small amplitude difference

$$\Delta E = \frac{E_o}{2} [e^{-\alpha^+ L} - e^{-\alpha^- L}]. \quad (2.43)$$

have developed between the two components. If both components are again superimposed at $y = L$ after the sample cell, an elliptically polarized wave comes out with a major axis which is slightly rotated against the x axis.

$$\begin{aligned} \vec{E} &= \vec{E}^+ + \vec{E}^- \\ &= \frac{E_{ox}}{2} e^{i(\omega t - k^+ L) - \alpha^+ L} \left[(1 + e^{(\alpha^+ - \alpha^-) L + i(k^+ - k^-) L}) \vec{x} + i(1 - e^{(\alpha^+ - \alpha^-) L + i(k^+ - k^-) L}) \vec{z} \right]. \end{aligned}$$

If the differences $\Delta \alpha$ and Δk are small,

$$(\alpha^+ - \alpha^-) L \ll 1 \quad \text{and} \quad (k^+ - k^-) L \ll 1, \quad (2.44)$$

we can expand the exponential factor

$$\frac{E_{ox}}{2} e^{i(\omega t - k^+ L) - \alpha^+ L} [2\vec{x} + i(\Delta \alpha + i\Delta k)L\vec{z}] \quad (2.45)$$

and obtain for the transmitted amplitude after a linear polarizer whose angle is set to θ relative to z axis

$$E_t = \frac{E_{ox}}{2} e^{i(\omega t - k^+ L) - \alpha^+ L} [2 \sin \theta + i(\Delta \alpha + i\Delta k)L \cos \theta] \quad (2.46)$$

Since the detector sees the the transmitted intensity $I_t = E_t^* E_t$,

$$\begin{aligned} I(\omega) &= I_o \left[4 \sin^2 \theta - 4 \sin \theta \cos \theta (\Delta k) L + (\Delta k^2 + \Delta \alpha^2) L^2 \cos^2 \theta \right] \\ &= I_o \left[4 \sin^2 \theta - 2 \sin(2\theta) \Delta k L + (\Delta k^2 + \Delta \alpha^2) L^2 \cos^2 \theta \right]. \end{aligned} \quad (2.47)$$

where $I_o = E_{ox}^2 e^{-2\alpha^+ L}/4$. When $\theta = 0$, the laser induced optical anisotropy,

$$I(\omega) = I_o (\Delta k^2 + \Delta \alpha^2) L^2, \quad (2.48)$$

is observed whereas with $\theta = 90$, the intensity modulated signal,

$$I(\omega) = 4I_o, \quad (2.49)$$

is observed. If signals recorded with θ and $-\theta$ are subtracted from each other a pure birefringent signal,

$$I(\omega) = -4I_o \sin(2\theta) \Delta k L, \quad (2.50)$$

can be recovered. The maximum birefringent signal is observed at $\theta = 45^\circ$. The differences $\Delta \alpha = \alpha^+ - \alpha^-$ in absorption coefficients and $\Delta n = n^+ - n^-$ in refractive indices are due to the different M sublevel populations experienced by the right or the left circularly polarized probe component. Although each coefficient α^+ and α^- itself shows a intensity modulated spectral profile, the difference $\Delta \alpha$ exhibits the small difference between these two lineshapes. For weak saturation with homogeneous linewidth γ , a Lorentzian spectral profile is obtained for $\Delta \alpha$

$$\Delta \alpha = \frac{\gamma^2}{(\Omega - \omega)^2 + \gamma^2} \Delta \alpha_o \quad (2.51)$$

where $\Delta \alpha_o$ is the maximum difference at the center $\omega = \Omega$, and using the Kramers-Kronig dispersion relationship, we obtain

$$\Delta k = \frac{-2\gamma^2 \omega}{[(\Omega - \omega)^2 + \gamma^2]^2} \Delta \alpha_o. \quad (2.52)$$

The magnitude of $\Delta \alpha_o$ depends on the pump intensity I_p , the transition probability for the optical transition, and on relaxation processes which tend to restore thermal equilibrium. For the general case where pump wave and probe wave may come

from different lasers tuned to the coupled transitions $(J' = J_b) \leftarrow (J'' = J_a)$ and $(J' = J_c) \leftarrow (J'' = J_b)$ with a common level J_b , $\Delta\alpha$ can be calculated from the expression^{16,86}

$$\Delta\alpha = \frac{1}{2}\alpha_0(I_p/I_s) \cdot \zeta(J_b, J_a, J_c, \Delta M). \quad (2.53)$$

Here α_0 is the unsaturated absorption coefficient and I_p the pump intensity. The saturation intensity

$$I_s = \frac{\hbar\omega_{ab}}{\sigma_{J_a J_b}} \cdot \frac{\gamma_a \gamma_b}{\gamma_a + \gamma_b} \quad (2.54)$$

depends on the cross section $\sigma_{J_a J_b}$ for the pump transition and on the homogeneous widths γ_a and γ_b of lower and upper levels, respectively. The numerical factor ζ depends on the pump transition ($J_b \leftarrow J_a$), the probe transition ($J_c \leftarrow J_b$), and on the pump polarization. The factor ζ can be calculated from a sum of the Clebsch-Gordan coefficients over the M levels if weak saturation is assumed.⁸⁵ For $^{\text{Q}}\text{R}(4,3)$ pumping the calculated values of $\zeta(J_b, J_a, J_c, +1)$ are close to 1, $\frac{1}{6}$, and -1 for $P-$, $Q-$, and $R-$ branch probe, respectively. Therefore P -branch transitions have opposite signs from R -branch transitions whereas Q -branch transitions are too weak to be observed in general. These intensity changes are used to identify the branch of transitions in polarization labeling spectroscopy.

IX. Jones Calculus

The Jones calculus is a procedure for treating the effect of optical components on a beam of polarized light. In the Jones calculus,¹²³⁻¹³⁰ the light beam is represented by a vector (Jones vector), the optical device encountered by the beam is represented by a matrix (Jones matrix), and the two are multiplied to yield another vector representing the light beam after interaction with the optical element. Following the notation used by Kliger et. al.,¹³¹ examples of Jones vectors and matrices are described assuming that the polarized light propagates along the z direction.

The Jones vector for polarized light is

$$\vec{J} = \begin{pmatrix} A_x e^{i\phi_x} \\ A_y e^{i\phi_y} \end{pmatrix}$$

where A and ϕ are a positive amplitude factor and a phase factor of the light along the x or y axis, respectively. The intensity of the light can be calculated from

$$I = J^* \cdot J = A_x^2 + A_y^2$$

Using the standard normalized forms of Jones vectors, in which the vectors are reduced to their simplest forms and have a magnitude of 1, corresponding Jones vectors for σ^\pm ($A_x = 1, A_y = 0$) and π ($A_x = 0, A_y = 1$) polarized light are

$$J_{\sigma^\pm} = \begin{pmatrix} 1 \\ 0 \end{pmatrix}, J_\pi = \begin{pmatrix} 0 \\ 1 \end{pmatrix}.$$

The Jones vectors for right- (σ^+) or left- (σ^-) circularly polarized lights are

$$J_{\sigma^+} = \frac{1}{\sqrt{2}} \begin{pmatrix} 1 \\ i \end{pmatrix}, J_{\sigma^-} = \frac{1}{\sqrt{2}} \begin{pmatrix} 1 \\ -i \end{pmatrix}.$$

Various forms of the Jones matrix are listed here for the optical components treated in this thesis. For a linear polarizer at angle θ from the x axis,

$$M_{(\theta)} = \begin{pmatrix} \cos^2 \theta & \sin \theta \cos \theta \\ \sin \theta \cos \theta & \sin^2 \theta \end{pmatrix}$$

$$M_{(0)} = \begin{pmatrix} 1 & 0 \\ 0 & 0 \end{pmatrix} \quad M_{(90)} = \begin{pmatrix} 0 & 0 \\ 0 & 1 \end{pmatrix}$$

$$M_{(45)} = \frac{1}{2} \begin{pmatrix} 1 & 1 \\ 1 & 1 \end{pmatrix} \quad M_{(-45)} = \frac{1}{2} \begin{pmatrix} 1 & -1 \\ -1 & 1 \end{pmatrix}$$

The absorption by a sample is treated as the effect of an optical component. For an isotropic sample,

$$M = \begin{pmatrix} p & 0 \\ 0 & p \end{pmatrix} \text{ where } p = e^{-\alpha L}, L = \text{path length.}$$

For linear dichroism,

$$M_{LD} = \begin{pmatrix} p_x & 0 \\ 0 & p_y \end{pmatrix} \text{ where } \begin{cases} p_x = e^{-\alpha_x L/2} \\ p_y = e^{-\alpha_y L/2} \end{cases}$$

where $\alpha_x(\alpha_y)$ is the absorption coefficient for $xz(yz)$ plane polarized light. For linear birefringence,

$$M_{LB} = \begin{pmatrix} e^{i\delta} & 0 \\ 0 & e^{-i\delta} \end{pmatrix} \text{ where } \delta = \frac{\omega(n_{\sigma\pm} - n_{\pi})L}{2c}$$

and $n_{\sigma\pm}(n_{\pi})$ is the refractive index for $xz(yz)$ plane polarized light. For circular dichroism,

$$M_{CD} = \frac{1}{2} \begin{pmatrix} p_r + p_l & -i(p_r - p_l) \\ i(p_r - p_l) & p_r + p_l \end{pmatrix} \text{ where } \begin{cases} p_r = \exp^{-\alpha_r L/2} \\ p_l = \exp^{-\alpha_l L/2} \end{cases}$$

and $\alpha_r(\alpha_l)$ is the absorption coefficient for right (left) circularly polarized light. For circular birefringence,

$$M_{CB} = \begin{pmatrix} \cos \delta & \sin \delta \\ -\sin \delta & \cos \delta \end{pmatrix} \text{ where } \delta = \frac{\omega(n_r - n_l)L}{2c}$$

and $n_l(n_r)$ is the index of refraction for left (right) circularly-polarized light.

We assume a linearly polarized pump beam creates only linear anisotropy (LD, LB) and a circularly polarized pump beam creates only circular anisotropy (CD, CB). We can then find Jones matrices for the optical anisotropy induced by polarized pump lasers. Since M_{LD} and M_{LB} commute, the induced anisotropy by a linearly polarized laser can be expressed as a product of M_{LD} and M_{LB} ,^c

$$M_{al} = M_{LD}M_{LB} = \begin{pmatrix} p_x & 0 \\ 0 & p_y \end{pmatrix} \begin{pmatrix} e^{i\delta} & 0 \\ 0 & e^{-i\delta} \end{pmatrix} = \begin{pmatrix} p_x e^{i\delta} & 0 \\ 0 & p_y e^{-i\delta} \end{pmatrix} \quad (2.55)$$

^cIf the two matrices do not commute, this can not be done by a simple multiplication of two matrices. Although, this greatly complicates the derivation, similar operation can be performed using Jones N matrix. The Jones N matrix is discussed by Jones¹²⁹ in detail.

where M_{al} represents the Jones matrix for alignment induced by a xy plane polarized laser. Similarly, the Jones matrix for a polarization oriented sample can be represented by

$$\begin{aligned} M_{or} &= M_{CD}M_{CB} = \frac{1}{2} \begin{pmatrix} p_r + p_l & -i(p_r - p_l) \\ i(p_r - p_l) & p_r + p_l \end{pmatrix} \begin{pmatrix} \cos \delta & \sin \delta \\ -\sin \delta & \cos \delta \end{pmatrix} \\ &= \frac{1}{2} \begin{pmatrix} (p_r + p_l) \cos \delta + i(p_r - p_l) \sin \delta & (p_r + p_l) \sin \delta - i(p_r - p_l) \cos \delta \\ -(p_r + p_l) \sin \delta + i(p_r - p_l) \cos \delta & (p_r + p_l) \cos \delta + i(p_r - p_l) \sin \delta \end{pmatrix} \end{aligned} \quad (2.56)$$

We obtain $M_{al'}$ induced by a σ^\pm from Eq. 2.55 by exchanging p_x and p_y and replacing δ by $-\delta$ and $M_{or'}$ induced by a σ^- from Eq. 2.56 after exchanging p_r and p_l and by replacing δ with $-\delta$.

Since the infrared detector sees only the power of incident radiation, we are interested in the intensity of the resulting radiation $I = J^* \cdot J$.

We now consider the case where the sample is probed with a linearly polarized beam under various pumping conditions.

- π pump, π probe: The sample has LD and LB due to π pumping. Therefore the necessary calculation is $M_{LD}M_{LB}J_{\sigma^\pm}$:

$$\begin{aligned} M_{al}J_\pi &= \begin{pmatrix} p_x e^{i\delta} & 0 \\ 0 & p_y e^{-i\delta} \end{pmatrix} \begin{pmatrix} 0 \\ 1 \end{pmatrix} = \begin{pmatrix} 0 \\ p_y e^{-i\delta} \end{pmatrix} \\ I &= p_y^2. \end{aligned} \quad (2.57)$$

This is the typical double resonance configuration where two orthogonal plane polarized lasers are used for pump and probe.

- σ^\pm pump, π probe: $M_{al'}$ can be derived from M_{al} by interchanging p_x and p_y and replacing δ with $-\delta$.

$$\begin{aligned} M_{al'} \begin{pmatrix} 0 \\ 1 \end{pmatrix} &= \begin{pmatrix} 0 \\ p_x e^{-i(-\delta)} \end{pmatrix} \\ I &= p_x^2. \end{aligned} \quad (2.58)$$

If pumping induces a linear dichroism ($p_x \neq p_y$) as well as population changes, Eq. 2.57 is different from Eq. 2.58 and different intensities are observed for different configurations. This difference can be directly measured by modulating the polarization states of the pump beam between σ^\pm and π .

- σ^\pm/π pump modulation, π probe:

$$I_{\sigma^\pm}^2 - I_\pi^2 = p_x^2 - p_y^2 \quad (2.59)$$

This value increases as the effect of linear dichroism increases. If the pump changes only the population without inducing a linear dichroism ($p_x = p_y = p$) there will be no signal observed.

- σ^+ pump, π probe: The σ^+ pump induces circular dichroism and birefringence to the sample. Therefore, the required calculation is $M_{CD}M_{CB}J_\pi = M_{or}J_\pi$.

$$M_{or} \begin{pmatrix} 0 \\ 1 \end{pmatrix} = \frac{1}{2} \begin{pmatrix} (p_r + p_l) \sin \delta - i(p_r - p_l) \cos \delta \\ (p_r + p_l) \cos \delta + i(p_r - p_l) \sin \delta \end{pmatrix}$$

$$I = (p_r^2 + p_l^2)/2. \quad (2.60)$$

$M_{or'}$ induced by a σ^- pump is identical to the M_{or} induced by a σ^+ pump, if the p_r and δ in Eq. 2.56 is replaced with p_l and $-\delta$, respectively. Therefore a detector sees the same intensity as in Eq. 2.60.

- σ^+/σ^- pump modulation, π probe: Obviously, modulation of the polarization between σ^+ and σ^- should not change the intensity seen by the detector.

$$I = I_{\sigma^+}^2 - I_{\sigma^-}^2 = 0 \quad (2.61)$$

However, adding an analysing polarizer in front of the detector leads to a completely different story.

- σ^+ pump, π probe, polarizer($\theta = 90$): Required calculation is $M_{\theta=90}M_{CD}M_{CB}J_{\pi}$:

$$\begin{aligned} M_{(90)}M_{or} \begin{pmatrix} 0 \\ 1 \end{pmatrix} &= \begin{pmatrix} 0 & 0 \\ 0 & 1 \end{pmatrix} \frac{1}{2} \begin{pmatrix} (p_r + p_l) \sin \delta - i(p_r - p_l) \cos \delta \\ (p_r + p_l) \cos \delta + i(p_r - p_l) \sin \delta \end{pmatrix} \\ &= \frac{1}{2} \begin{pmatrix} 0 \\ (p_r + p_l) \cos \delta + i(p_r - p_l) \sin \delta \end{pmatrix} \end{aligned}$$

$$\begin{aligned} I &= [p_r^2 + p_l^2 + 2p_r p_l (\cos^2 \delta - \sin^2 \delta)]/4 \\ &= [p_r^2 + p_l^2 + 2p_r p_l \cos(2\delta)]/4. \end{aligned} \quad (2.62)$$

The corresponding I for a σ^- pump is $[p_r^2 + p_l^2 + 2p_r p_l \cos(-2\delta)]/4$.

- σ^+/σ^- pump modulation, π probe, polarizer($\theta = 90$):

$$I_{\sigma^+}^2 - I_{\sigma^-}^2 = 0 \quad (2.63)$$

- σ^+ pump, π probe, polarizer($\theta = 0$):

$$\begin{pmatrix} 1 & 0 \\ 0 & 0 \end{pmatrix} M_{or} \begin{pmatrix} 0 \\ 1 \end{pmatrix} = \frac{1}{2} \begin{pmatrix} (p_r + p_l) \sin \delta - i(p_r - p_l) \cos \delta \\ 0 \end{pmatrix}$$

$$\begin{aligned} I &= [p_r^2 + p_l^2 + 2p_r p_l (\sin^2 \delta - \cos^2 \delta)]/4 \\ &= [p_r^2 + p_l^2 - 2p_r p_l \cos(2\delta)]/4. \end{aligned} \quad (2.64)$$

- σ^+/σ^- pump modulation, π probe, polarizer($\theta = 0$):

$$I_{\sigma^+}^2 - I_{\sigma^-}^2 = 0 \quad (2.65)$$

- σ^+ pump, π probe, polarizer($\theta = 45$):

$$\frac{1}{2} \begin{pmatrix} 1 & 1 \\ 1 & 1 \end{pmatrix} M_{or} \begin{pmatrix} 0 \\ 1 \end{pmatrix} = \frac{1}{4} \begin{pmatrix} (p_r + p_l)(\sin \delta + \cos \delta) + i(p_r - p_l)(\sin \delta - \cos \delta) \\ (p_r + p_l)(\sin \delta + \cos \delta) + i(p_r - p_l)(\sin \delta - \cos \delta) \end{pmatrix}$$

$$I = (p_r^2 + p_l^2 + 2p_r p_l \sin 2\delta)/4. \quad (2.66)$$

- σ^+/σ^- pump modulation, σ^\pm probe, polarizer($\theta = 45$):

$$I_{\sigma^+}^2 - I_{\sigma^-}^2 = p_r p_l \sin 2\delta \quad (2.67)$$

If $2\delta \ll 1$ this can be expanded to $-2p_r p_l \delta$ from which the laser induced circular birefringence $\delta = \pi\omega(n_l - n_r)d/2$ can be deduced. On the other hand, linear dichroism can be measured from Eq. 2.59.

Similar expressions for a circularly polarized probe are derived, as follows,

- σ^\pm pump, σ^+ probe:

$$M_{al} \frac{1}{\sqrt{2}} \begin{pmatrix} 1 \\ i \end{pmatrix} = \frac{1}{\sqrt{2}} \begin{pmatrix} p_x e^{i\delta} \\ p_y e^{-i\delta} \end{pmatrix}$$

$$I = (p_x^2 + p_y^2)/2 \quad (2.68)$$

- σ^\pm/π pump modulation, σ^+ probe:

$$I = I_{\sigma^\pm}^2 - I_\pi^2 = 0 \quad (2.69)$$

- σ^\pm pump, σ^+ probe, polarizer($\theta = 0$):

$$\begin{pmatrix} 1 & 0 \\ 0 & 0 \end{pmatrix} M_{al} \frac{1}{\sqrt{2}} \begin{pmatrix} 1 \\ i \end{pmatrix} = \frac{1}{\sqrt{2}} \begin{pmatrix} p_x e^{i\delta} \\ 0 \end{pmatrix}$$

$$I = p_x^2/2 \quad (2.70)$$

- σ^\pm/π pump modulation, σ^+ probe, polarizer($\theta = 0$):

$$I = (p_x^2 - p_y^2)/2 \quad (2.71)$$

- σ^\pm pump, σ^+ probe, polarizer($\theta = 45$):

$$M_{45} M_{al} \frac{1}{\sqrt{2}} \begin{pmatrix} 1 \\ i \end{pmatrix} = \frac{1}{2} \begin{pmatrix} 1 & 1 \\ 1 & 1 \end{pmatrix} \frac{1}{\sqrt{2}} \begin{pmatrix} p_x e^{i\delta} \\ p_y e^{-i\delta} \end{pmatrix}$$

$$= \frac{1}{\sqrt{8}} \begin{pmatrix} p_x e^{i\delta} + p_y e^{-i\delta} \\ p_x e^{i\delta} + p_y e^{-i\delta} \end{pmatrix}$$

$$I = [p_x^2 + p_y^2 + 2p_x p_y \cos(2\delta)]/4 \quad (2.72)$$

For π pump, the intensity is $I_\pi^2 = [(p_y^2 + p_x^2 + 2p_y p_x \cos 2(-\delta)]/4$.

- σ^\pm/π pump modulation, σ^+ probe, polarizer(45):

$$I = 0 \quad (2.73)$$

- σ^+ pump, σ^+ probe:

$$M_{or} \frac{1}{\sqrt{8}} \begin{pmatrix} 1 \\ i \end{pmatrix} = \frac{1}{\sqrt{2}} \begin{pmatrix} 2p_r(\cos \delta + i \sin \delta) \\ -2p_r(\sin \delta - i \cos \delta) \end{pmatrix}$$

$$I = p_r^2 \quad (2.74)$$

- σ^- pump, σ^+ probe:

$$I = p_i^2 \quad (2.75)$$

- σ^+/σ^- pump modulation, σ^+ probe:

$$I = p_r^2 - p_i^2 \quad (2.76)$$

- σ^+ pump, σ^+ probe, polarizer($\theta = 0$):

$$M_0 M_{or} \frac{1}{\sqrt{2}} \begin{pmatrix} 1 \\ i \end{pmatrix} = \frac{1}{\sqrt{2}} \begin{pmatrix} 2p_r(\cos \delta + i \sin \delta) \\ 0 \end{pmatrix}$$

$$I = 4p_r^2 \quad (2.77)$$

- σ^+ pump, σ^+ probe, polarizer($\theta = 90$):

$$M_{90} M_{or} \frac{1}{\sqrt{2}} \begin{pmatrix} 1 \\ i \end{pmatrix} = \frac{1}{\sqrt{2}} \begin{pmatrix} 0 \\ -2p_r(\cos \delta + i \sin \delta) \end{pmatrix}$$

$$I = 4p_r^2 \quad (2.78)$$

- σ^+/σ^- pump modulation, σ^+ probe, polarizer($\theta = 0$):

$$I = p_r^2 - p_i^2 \quad (2.79)$$

Table 2.2: Comparison of calculated intensities using Jones calculus for different experimental conditions.

<i>Probe</i>	<i>Pump</i>	<i>Pol</i>	<i>I</i>	<i>Comment</i>
π	π	<i>no</i>	p_y^2	
π	π	0	0	
π	π	90	p_y^2	
π	π	45	$p_y^2/2$	
π	σ^\pm	<i>no</i>	p_x^2	
π	σ^\pm	0	0	
π	σ^\pm	90	p_x^2	
π	σ^\pm	45	$p_x^2/2$	
π	σ^\pm/π	<i>no</i>	$p_x^2 - p_y^2$	<i>LD</i>
π	σ^\pm/π	90	$p_x^2 - p_y^2$	<i>LD</i>
π	σ^\pm/π	45	$[p_x^2 - p_y^2]/2$	<i>LD</i>
π	σ^+	<i>no</i>	$(p_r^2 + p_l^2)/2$	
π	σ^+/σ^-	<i>no</i>	0	
π	σ^+	90	$[p_r^2 + p_l^2 + 2p_r p_l \cos(2\delta)]/4$	
π	σ^+/σ^-	90	0	
π	σ^+	0	$[p_r^2 + p_l^2 - 2p_r p_l \cos(2\delta)]/4$	
π	σ^+/σ^-	0	0	
π	σ^+	45	$[(p_r^2 + p_l^2) + 2p_r p_l \sin(2\delta)]/4$	
π	σ^+/σ^-	45	$p_r p_l \sin(2\delta)$	<i>CB</i>
σ^+	σ^\pm	<i>no</i>	$[p_x^2 + p_y^2]/2$	
σ^+	σ^\pm/π	<i>no</i>	0	
σ^+	σ^\pm	0	$p_x^2/2$	
σ^+	σ^\pm/π	0	$[p_x^2 - p_y^2]/2$	<i>LD</i>
σ^+	σ^\pm	90	$p_y^2/2$	
σ^+	σ^\pm/π	90	$[p_x^2 - p_y^2]/2$	<i>LD</i>
σ^+	σ^\pm	45	$[p_x^2 + p_y^2 + 2p_x p_y \cos(2\delta)]/4$	
σ^+	σ^\pm/π	45	0	
σ^+	σ^\pm	-45	$[p_x^2 + p_y^2 - 2p_x p_y \cos(2\delta)]/4$	
σ^+	σ^\pm/π	-45	0	
σ^+	σ^+	<i>no</i>	p_r^2	
σ^+	σ^-	<i>no</i>	p_l^2	
σ^+	σ^+/σ^-	<i>no</i>	$(p_r^2 - p_l^2)$	<i>CD</i>
σ^+	σ^+	0	$p_r^2/2$	
σ^+	σ^+	90	$p_r^2/2$	
σ^+	σ^+/σ^-	0	$(p_r^2 - p_l^2)/2$	<i>CD</i>
σ^+	σ^+/σ^-	90	$(p_r^2 - p_l^2)/2$	<i>CD</i>

Derivation of Jones calculus for all possible optical pumping experiments are derived and listed in Table IX. It will be worth mentioning a few findings from this Table. First the four components of laser induced optical anisotropy, namely LD , LB, CD, and CB, can be independently measured using different experimental schemes listed in Table IX.

1. The LD ($\Delta\alpha^L = \alpha_{\sigma^\pm} - \alpha_\pi$) can be measured directly when the polarization of the pump is modulated between π and σ^\pm using either a plane- or a circularly-polarized probe.
2. The LB ($\Delta n^L = n_\sigma^\pm - n_\pi$) can be calculated from two different measurements taken with circularly polarized probe under plane polarized pump with a linear polarizer rotated to 45° and to -45° from the reference axis.
3. The CD ($\Delta\alpha^C = \alpha_l - \alpha_r$) can be measured directly with a circularly polarized probe while modulating the polarization of the pump between σ^+ and σ^- .
4. The CB ($\Delta n^C = n_l - n_r$) can be directly measured using a plane polarized probe while modulating the polarization of the pump between σ^+ and σ^- with a polarizer rotated to 45° relative to the reference axis.

Chapter 3

Experimental

I. Lineshape Study of Transferred Spikes

A block diagram of the spectrometer used for the present study, which includes some improvements from that used previously in this laboratory, is shown in Figure 3.1. A CO₂ laser (Laser1)^a serves as the pumping source, while an infrared microwave sideband laser (IMSL) of the Magerl design¹³² (Laser2) is used for the probe source. The two single mode CO₂ lasers are each stabilized by monitoring the Lamb dip in the fluorescence from a CO₂ sample in a cell outside the laser cavity(FC). The frequency jitter of each of the two sources is estimated to be < 150 kHz including the intentional frequency modulation used for the stabilization. One of the lasers is a flowing gas system that is normally used as the pumping source for the double resonance, while the second laser is a semi-sealed model that is normally used as the carrier frequency for the IMSL system. In this work the two lasers were interchanged when the ^QR(11,9) transition in ¹²CH₃F was pumped, because in this case ¹²C¹⁸O₂ is required for the laser transition. The microwaves for the IMSL system were generated by a computer-controlled synthesizer (accuracy ~ 3 kHz) and amplified to ~ 20 W by a traveling wave tube amplifier (TWTA). The infrared and microwaves were mixed in a CdTe crystal in an RF-matched housing (Mod). The IR radiation leaving the crystal contained the laser carrier at frequency ω_l and upper and lower sidebands at

^aThe abbreviations in parentheses refer to abbreviations used in Figure 3.1

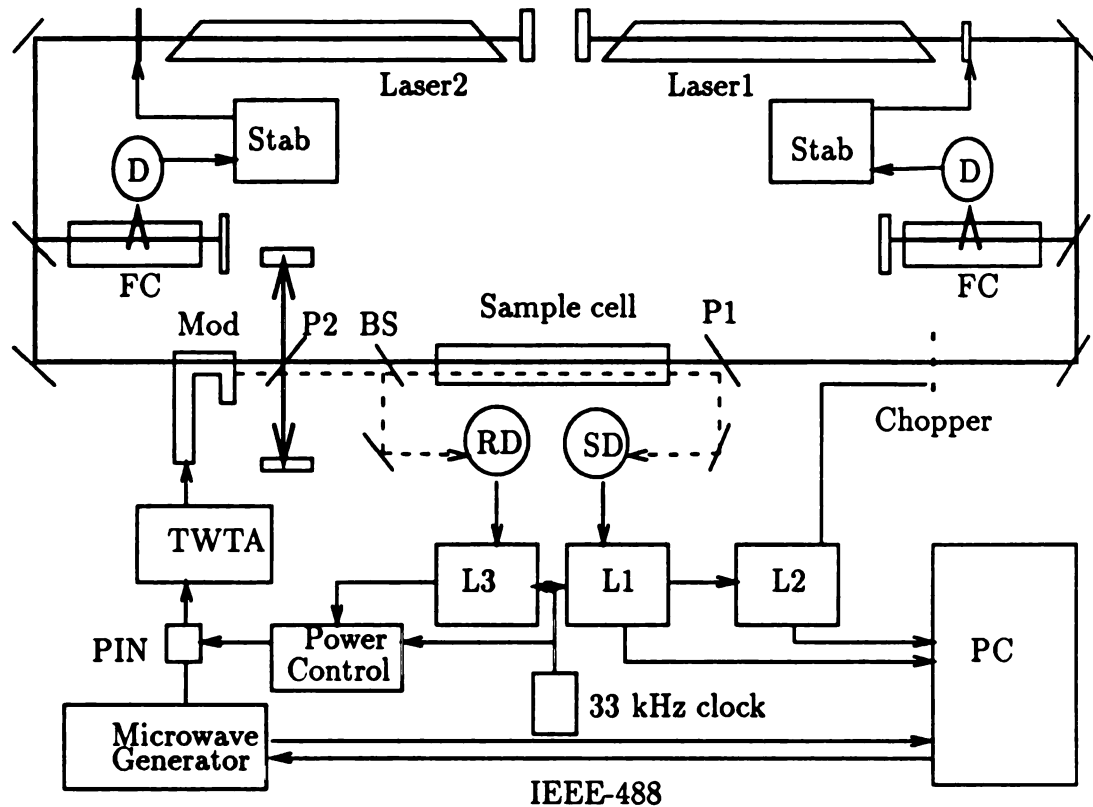


Figure 3.1: A CO₂ laser infrared microwave sideband laser double resonance system. The two CO₂ lasers are frequency stabilized to the fluorescence Lamb dip of CO₂(FC). The sideband is generated by mixing one of the CO₂ lasers with high power microwaves (8 – 18 GHz) in a CdTe crystal (Mod) and its intensity is stabilized by monitoring its output (RD). Since the sideband is amplitude modulated at 33 kHz, detected signals (SD,RD) always get demodulated at 33 kHz first by L1 or L3. The output from L1 is double demodulated (L2) at the chopping frequency (~ 100 Hz). The signal from L2 comes therefore purely from double resonance effects. Since the pump laser modulated by a mechanical chopper has a horizontal plane of polarization, it can be separated from the sideband laser using two polarizers P1,P2. The use of a polarizer to separate the two laser beams allows easy and perfect alignment that is critical to the lineshape.

frequencies $\omega_l \pm \omega_m$ where ω_m is the microwave frequency. The carrier and sidebands had orthogonal planes of polarization so that the carrier was reflected by the first polarizer (P2) after the modulation.

The two infrared sources, pump radiation and IMSL probe, had orthogonal planes of polarization and the arrangement of polarizers shown in Figure (3.1) was used to separate the two beams for the usual geometry of counter-propagating pump and probe radiation. When co-propagating radiation was needed, as in some three-level double resonance experiments, it was necessary to slightly misalign the two beams. Although the probe radiation included both upper and lower sidebands, the spectrum of methyl fluoride is sufficiently sparse that only one of the two sidebands was absorbed in any given experiment.¹³³

The sample cell for all of the measurements was a 1-m long glass tube, 25 mm in diameter, with NaCl windows mounted at a slight angle to reduce etalon effects. The methyl fluoride sample was purchased from Peninsula Chemical Research and used as received. Sample pressures, which were 1–20 mTorr, were measured by means of a capacitance manometer. All of the spectra were recorded at room temperature ($\sim 295K$).

As shown in Figure 3.1, the double resonance effects were recorded by means of a double modulation scheme. The infrared-microwave sidebands were 100% amplitude modulated by chopping the microwaves by means of a PIN diode. A portion of the sidebands, monitored by a reference detector (RD) and processed by a phase-sensitive lock-in amplifier (L3), was used for stabilization of the amplitude of the probe beam by controlling the microwave power applied to the sideband generator. The frequency of the sideband chopping (~ 33 kHz) was high enough to eliminate much of the laser noise, but low enough to ignore the effect of modulation sidebands. The output of the lock-in amplifier (L1) that processed the output of the signal detector (SD) contained the single+double-resonance spectrum and was often recorded by the computer. The S/N ratio of this spectrum was rather high, not only because of the low time constant filtering required to allow the second lock-in amplifier (L2) to process the double resonance effect, but also because of the intensity changes that resulted from the intensity modulation of the pump beam. The pump beam was amplitude modulated

by a mechanical chopper at 100 Hz for four-level double resonance, but at frequencies up to 1 kHz for three-level double resonance. The output of the second lock-in amplifier (L2) contained only the double-resonance effects, which were recorded by the computer (PC) for later numerical processing.

II. Polarization Spectroscopy

Figure 3.2 shows the experimental diagram of a CO₂ laser-IMSL double resonance system employing an electro-optic switch used for polarization experiments. The main differences from a typical intensity modulated double resonance technique are (a) pump laser guiding optics and (b) the electro-optic polarization modulator shown in Figure 3.3. The heart of the guiding optics is a 90% reflecting mirror that passes 10% of incident radiation through the mirror. When a pump beam hits the mirror, 90% of the radiation is reflected off the mirror into the sample cell while approximately 10% of the IMSL probe radiation passes the mirror and is detected by the usual double demodulation scheme. The electro-optic switch system consists of a CdTe crystal mounted in a high-voltage housing, a Fresnel rhomb rotated at 45° angle, a wire-grid polarizer, two 2.1 kV variable high voltage power supplies, a home made high voltage switching circuit, and a programmable trigger circuit. The details of the flowing gas CO₂ laser, the infrared-microwave sideband laser, and the handling of the sample were already explained in the previous section.

In Figure 3.3, for the intensity-modulated studies the flowing gas CO₂ pump laser (PL) was essentially 100% amplitude modulated by passing the beam successively through a CdTe electro-optic crystal (CdTe), a ZnSe Fresnel rhomb (Rhomb), and a polarizer (P1). By repetitively switching a voltage across the electro optic crystal (CdTe) between +2100 V and -2100 V, the plane-polarized infrared beam entering the crystal was switched between right and left circularly-polarized radiation. The rhomb converted the circularly-polarized light to horizontal or vertical plane-polarized radiation and the polarizer (P1) then reduced the beam power by almost three orders of magnitude during one-half of each cycle. The switching can be controlled by any pulse generator that provides TTL pulses at rates up to 10 kHz. For the experiments

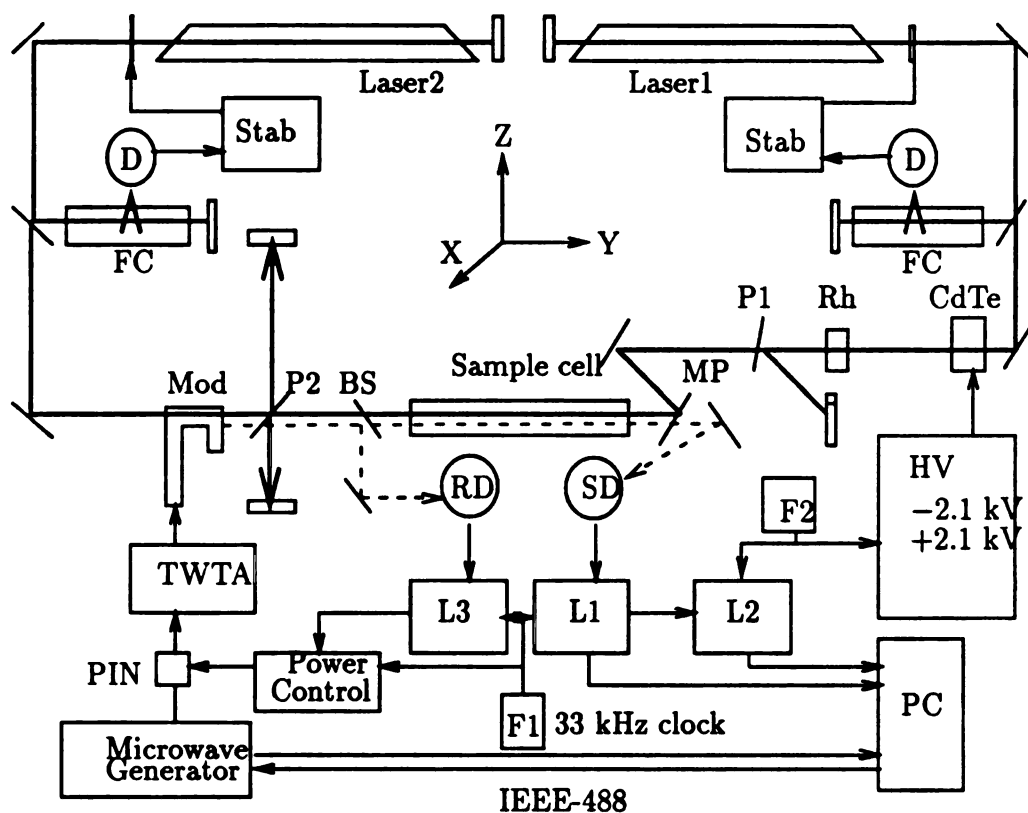


Figure 3.2: Block diagram of the CO₂ laser - IMSL double resonance setup employing an electro-optic modulator. When 2.1 kV is applied to the CdTe modulator, it converts the YX plane polarized (π) pump laser into right circularly polarized (σ^+) light. The σ^+ radiation is changed back to a π -polarized laser after the rhomb (Rh) that works as a quarter wave plate. The laser passes a blocking polarizer (P1) whose angle is set to π and perturbs molecules in the sample cell. If -2.1 kV is applied instead, the pump laser becomes σ^\pm polarized and is reflected off the polarizer to a beam stop. The result is a TTL controlled optical modulator with π plane polarized laser pumping (perpendicular configuration). The same setup can be used to modulate σ^\pm plane polarized pump by rotating the blocking polarizer parallel to the YZ plane (parallel configuration).

described here, the switching was performed by means of an electronic switch designed by Martin Rabb at MSU.

Unlike previous double resonance setups where intentional misalignment, Brewster angle windows, or polarizers were used to separate a probe beam from the pump beam, the current setup with a partially transmitting mirror (MP) allows a unique and rich environment for various double resonance experiments by allowing the use of σ^\pm , π , σ^+ , σ^- , or any other kind of polarization states of lasers for modulation purposes. For example, the same setup can be used to record orientation modulation, in which the polarization state of the pump beam is switched between σ^\pm and π , by removing the blocking polarizer (P1), as in Figure 3.4. Also, by removing the Fresnel rhomb, it can be used for orientation modulation, in which the polarization of the pump laser is switched between σ^+ and σ^- (Figure 3.6). Figures 3.3,3.4,3.6 graphically describe the polarization states of the pump beam under different experimental conditions.

A diagram of the modulation part in the alignment modulation experiment is shown in Figure 3.4. It is important to note that the intensity of the pump laser is constant all the time while the polarization state of the laser follows the TTL. This eliminates the *pure population pumping* effect from the recorded signal. A typical alignment modulated signal is shown in Figure 3.5 along with an intensity modulated signal. The alignment modulated signal is very similar to the typical double resonance signal except that the Gaussian part is suppressed.

The same setup is easily converted into an orientation modulated double resonance system by removing the Fresnel rhomb and by using a circularly polarized probe beam (Figure 3.6). The polarization state of the pump beam is now switched between σ^+ and σ^- . It creates a circular optical anisotropy in the sample, which means a different absorption coefficient ($\Delta\alpha = \alpha^+ - \alpha^-$) as well as refractive index ($\Delta n = n^+ - n^-$). A σ^+ probe beam, for example, can be used to observe this laser induced optical anisotropy.

Another interesting experimental setup takes advantage of the phase changes created by a circularly polarized pump with a linearly polarized probe beam. A linearly polarized pump beam σ^\pm can be considered as the sum of two circular components:

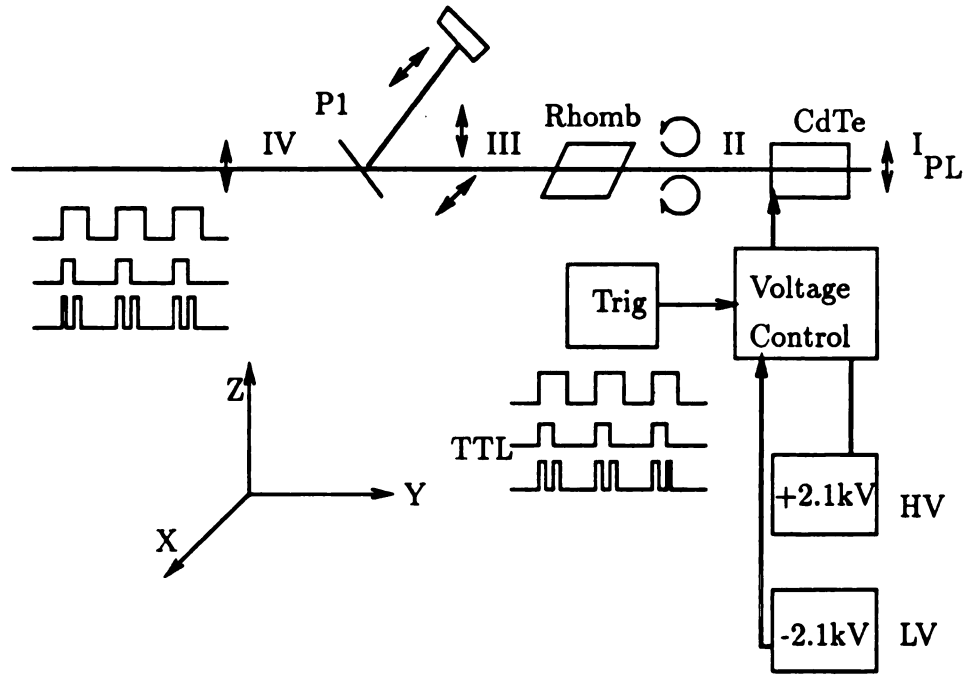


Figure 3.3: Diagram of the electro-optic switching system. A TTL signal controls the high voltage control circuit and applies either +2.1 kV or -2.1 kV to the CdTe housing. A $YX(\pi)$ plane polarized pump beam (PL) is either converted to right circular polarization (σ^+) or to left circular polarization (σ^-) by the CdTe, depending on the polarity of the high voltage applied to it. A Fresnel rhomb oriented at 45° converts the circularly polarized beams back into either σ^\pm or π . A blocking polarizer (P1) whose angle is set parallel to the YX plane blocks the σ^\pm polarization of the pump beam and passes only the π polarized state of the pump beam. Since the intensity of the pump beam follows the shape of the TTL signal shown in the picture, this is called *intensity modulation* in the text. The different polarization states of the pump laser are shown with I (π), II (σ^+ , σ^-), III (π , σ^\pm), and IV (π). The blocking polarizer (P1) can be rotated to obtain σ^\pm at IV.

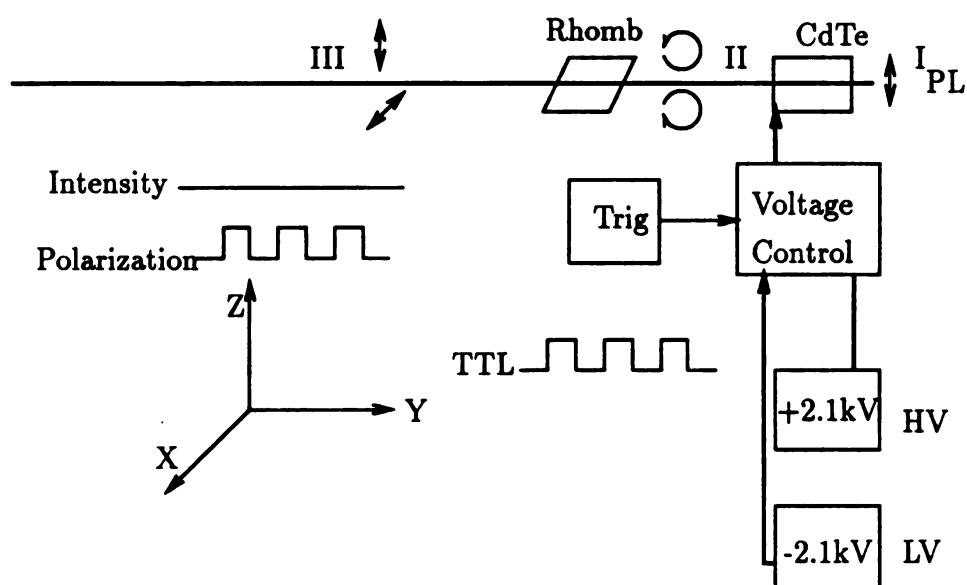


Figure 3.4: Block diagram for alignment modulation between σ^\pm and π . Note: The intensities of the two σ^\pm - and π -polarized pump beams do not change. Only the polarization state of the pump beam is switched. Therefore, the pump always creates the same holes and spikes in terms of total population while the alignment of the molecules is different.

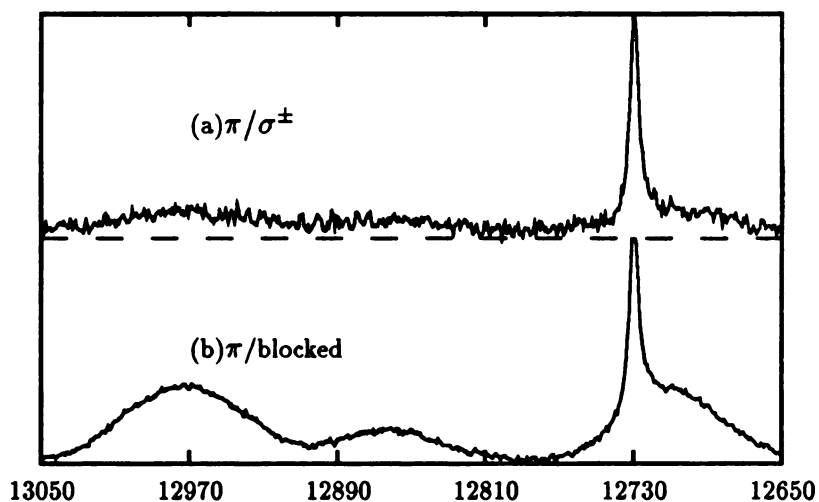


Figure 3.5: (a) Alignment modulated double resonance signal of the P(6,0), P(6,1), P(6,2), and P(6,3) in the $2\nu_3 \leftarrow \nu_3$ band of $^{13}\text{CH}_3\text{F}$. (b) Power modulated signal. The absolute intensity of the alignment modulated signal was about 1/3 of the normal double resonance signal. It is clear that the Gaussian signals are suppressed in the alignment modulation. The x -axis is the microwave frequency in MHz used to generate the sideband laser. When the transition is observed with negative sideband, the numbers are labeled in decreasing order.

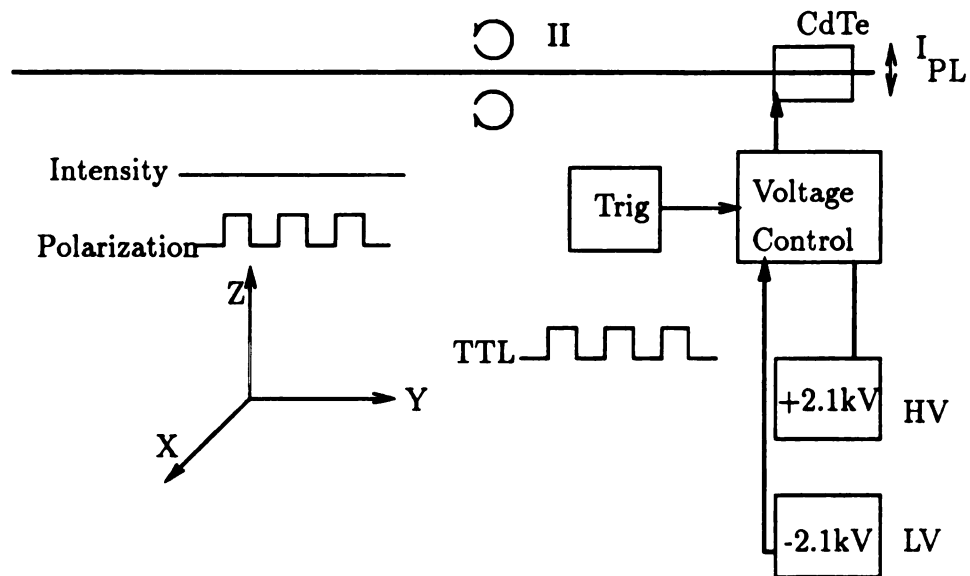


Figure 3.6: Modulation of the polarization states between σ^+ and σ^- . Again the intensity of the pump beam stays constant, as in alignment modulation. Either a circularly polarized probe beam or a plane polarized beam can be used to observe the optical anisotropy created in this pump scheme.

σ^+ and σ^- with the same intensity and no phase difference. The absorption coefficient and phase change experienced by a σ^+ component of the probe beam are different from those experienced by the σ^- component when a circularly polarized pump beam is used. A σ^\pm probe beam becomes an elliptically polarized beam (due to differential absorption coefficient) whose main axis is tilted (due to phase shift) a little from its original axis ($X - Y$ in the experiment). Although the intensity of the linearly polarized probe beam does not change as the polarization of the pump changes, the direction of the tilt created by the σ^+ pump is opposite to that created by the σ^- pump. If a polarizer oriented at 45° is put before the detector, the detector sees a difference in intensity upon changing the polarization state of the pump, because the polarizer selects only the polarization component of the probe beam along its axis. The intensity is proportional to the amount of the phase shift ($\Delta n = n^+ - n^-$), which is proportional in turn to the interaction between the pump and the sample. The signal recorded in this experiment is related to the previous signal via the Kramers-Kronig relationship and has a dispersion line shape as shown in Figure 3.7. For obvious reasons, no signal is observed when the polarizer before the detector is removed or if its angle is set close to either 0 or 90° relative to the σ^\pm plane.

Figure 3.8 graphically summarizes the polarization states of the pump and probe beams under variety of double resonance experiments.

In this part of the work, all of the double resonance experiments were performed with 1-60 mTorr of $^{13}\text{CH}_3\text{F}$ while the $(1,5,3) \leftarrow (0,4,3)$ transition was pumped by a flowing CO_2 gas laser with 1- 5 W/cm^2 power.

III. Time Resolved Spectroscopy

Figure 3.9 shows a diagram of the the spectrometer used for the time-resolved CO_2 laser-IMSL double resonance study. The spectrometer is essentially the same as the previous setup used for the saturation absorption experiments except for the data recording part. The details of the flowing gas CO_2 laser, the infrared-microwave sideband laser, and the sample handling are the same as described in the first section of this chapter. The pump beam is essentially 100% amplitude modulated as discussed

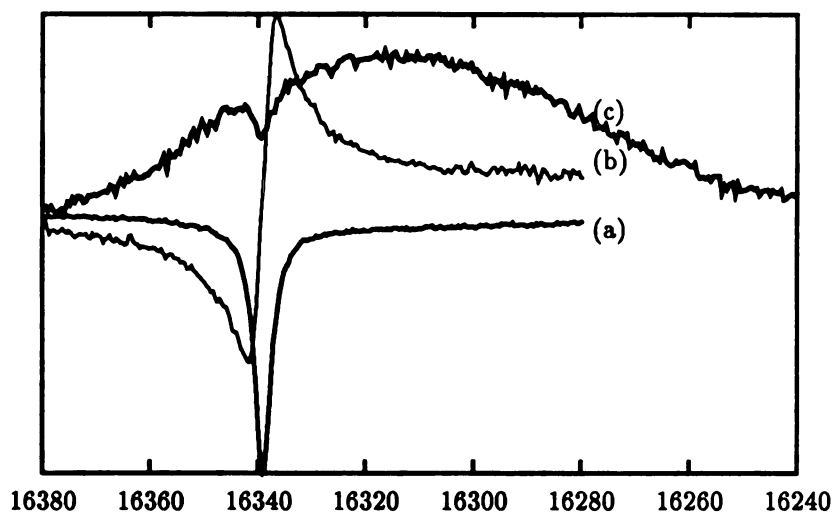


Figure 3.7: (a) Intensity modulated double resonance signal. of the R(4,3) transition in the ν_3 band of $^{13}\text{CH}_3\text{F}$. (b) Orientation modulated double resonance signal. (c) Single resonance absorption signal. The single resonance absorption signal has a Bennett hole due to the laser pumping. The orientation modulated double resonance signal has dispersion line shape. The horizontal axis is the (negative) microwave offset frequency (MHz).

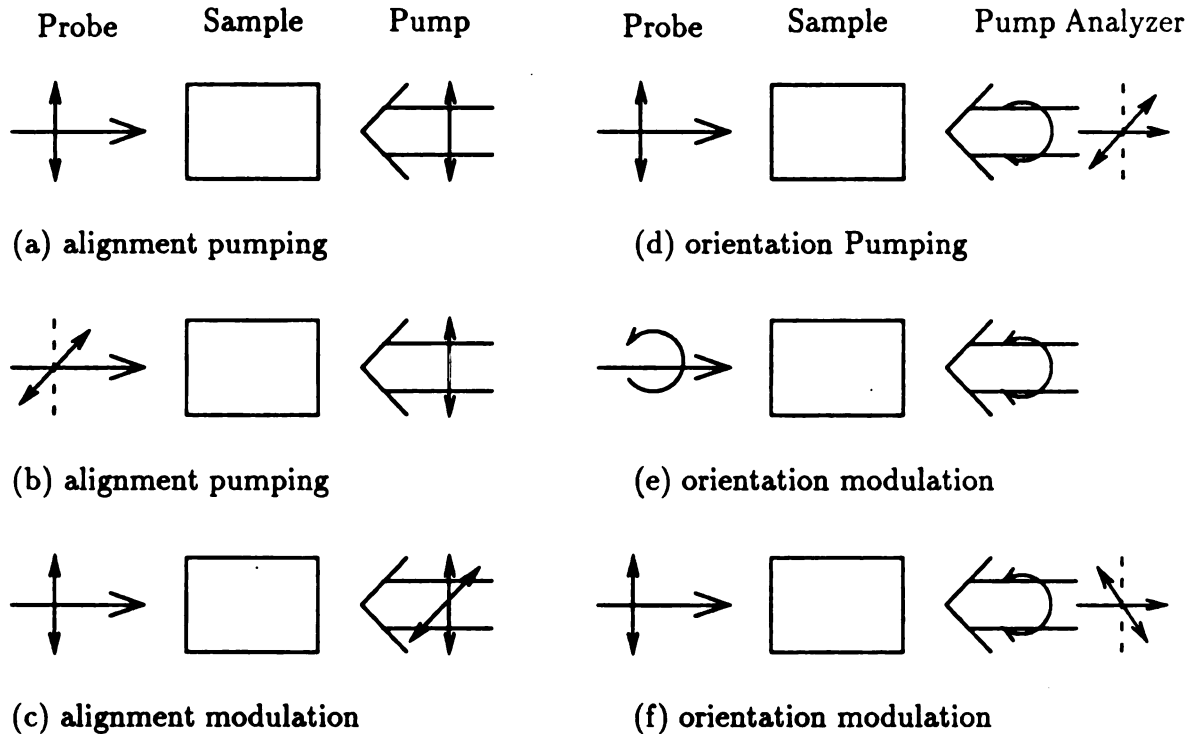


Figure 3.8: Experimental conditions for (a) alignment pumping: π -polarized pump, π -polarized probe; (b) alignment pumping: π -polarized pump, σ^\pm -polarized probe; (c) alignment modulation: π -polarized probe, $\sigma^\pm - \pi$ polarized pump; (d) orientation pumping: π probe, σ^+ pump, 90° polarizer; (e) orientation modulation: σ^+ probe, $\sigma^+ - \sigma^-$ pump, and (f) orientation modulation: π probe, $\sigma^+ - \sigma^-$ pump, 45° polarizer. For historical reasons (a) and (b) are also called as saturation absorption whereas (d) is called as polarization spectroscopy. Experiment (f) is named circular birefringent measurement because it measures laser-induced circular birefringence.

in Figure 3.10. For the time domain experiments, a rate of 100 Hz was used to ensure complete relaxation, while for some frequency domain experiments a 1 kHz rate was used to obtain better S/N ratio.

The sample cell was either a 1-m long glass tube, 25 mm in diameter, or a 1-m long White-type cell, operated with either 4-pass or 8-pass. The sample pressure was 10-60 mTorr and the temperature was 297 K. The 9P(32) laser (Laser1) pumped the $^2R(4,3)$ transition in the fundamental ν_3 band.

The IMSL radiation (dashed line in Figure 3.9) was directed to an InSb detector (SD) whose output was amplified and then processed by a lock-in amplifier (L1) at the pump laser modulation frequency (F) for steady state experiments or by a LECROY model 6810 transient recorder for time resolved experiments. In the time domain experiments the IMSL frequency was fixed at a frequency selected after observation of the frequency domain spectra. The IMSL absorption was then recorded as a function of time by the transient recorder. Figures 3.11 and 3.12 are frequency- and time-domain spectra recorded in this way.

The uniqueness of the described system is that it enables one to observe both the frequency domain and the time domain signal under the same conditions. Therefore, with nominal pumping power ($\sim 1W$), the typical double resonance line shape (sum of a Gaussian and spikes) can be recorded in the frequency domain (Figure 3.11) and the time response of each part can be observed separately (Figure 3.12). Since pulses of arbitrary duty ratio can be generated as long as the rate is less than 10 kHz, population increase rates (*pump-on*) as well as population relaxation rates (*pump-off*) can be studied simultaneously with the same setup by acquiring one complete pump cycle. Usually two complete cycles were recorded and then compared to avoid unpredictable errors such as sudden vibrations or random noise.

A. Electro-Optic Switch

Unlike the typical Q-switched lasers used for time resolved experiments, which have a spectral bandwidth comparable to or broader than the Doppler profile, the

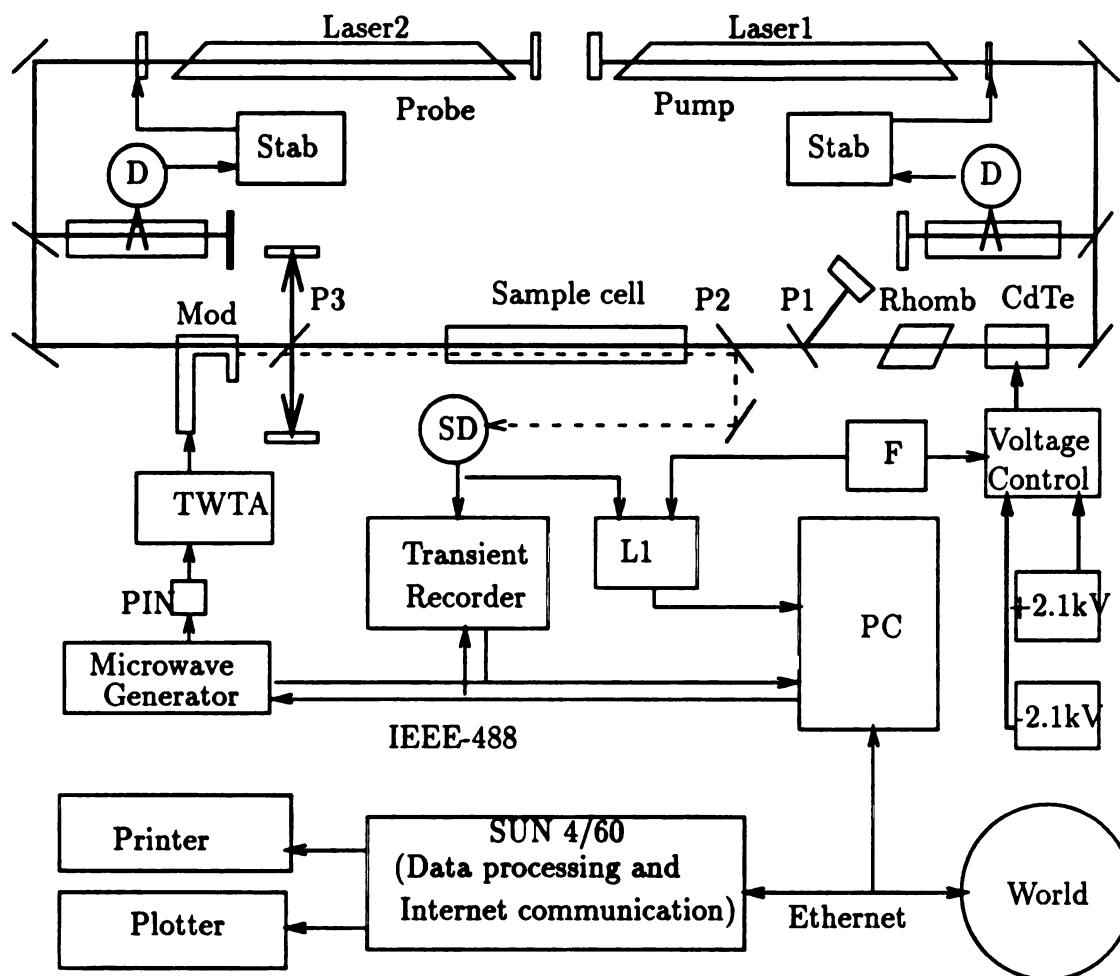


Figure 3.9: A schematic of the time resolved double resonance system used in this study. The flowing gas laser (Laser1) was used to pump $^Q R(4,3)$ transition in the ν_3 band. The beam paths of two CO₂ lasers and the high voltage cables are drawn with thick lines. The dashed line represents the IMSL beam path. Details of the operation are described in the text.

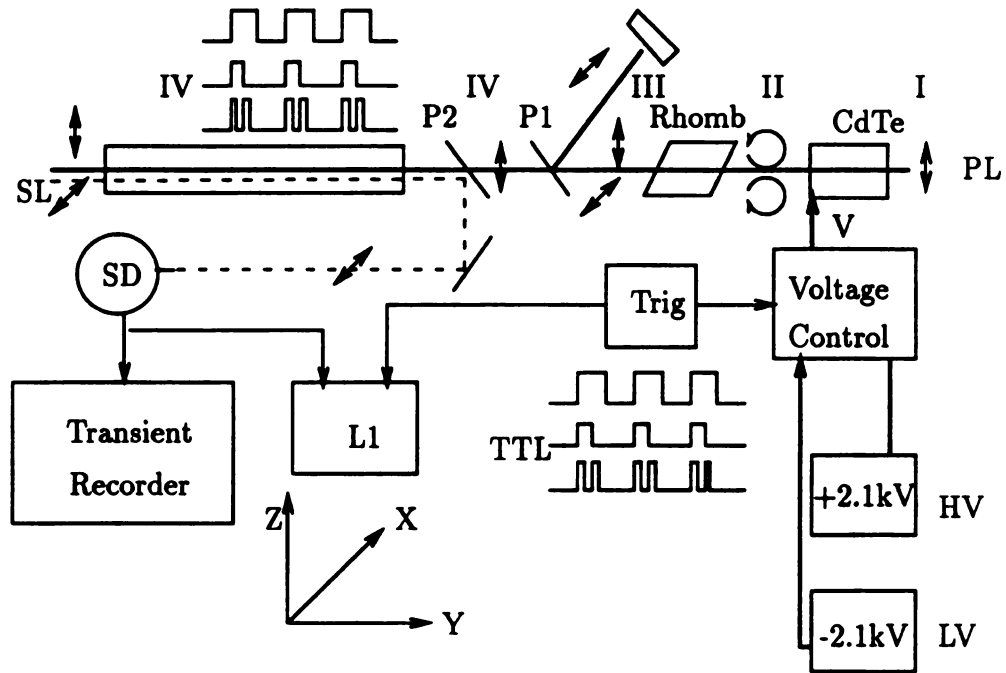


Figure 3.10: Diagram of the electro-optic switching system used for time resolved measurement. A TTL signal controls the high voltage control circuit and applies either +2.1 kV or -2.1 kV to the CdTe housing. A $YZ(\pi)$ plane polarized pump beam (PL) is either converted to right circular polarization (σ^+) or to left circular polarization (σ^-) by the CdTe, depending on the polarity of the high voltage applied to it. A Fresnel rhomb oriented at 45° converts the circularly polarized beams back into either σ^\pm or π . A blocking polarizer whose angle is set parallel to the YZ plane blocks the σ^\pm polarization of the pump beam and passes only the π polarized state of the pump beam. The amplitude of the final pump beam (IV) follows the shape of the TTL signal that is applied. A σ^\pm polarized sideband laser (SL) interacts with the sample, reflects off P2, and is monitored by the detector (SD).

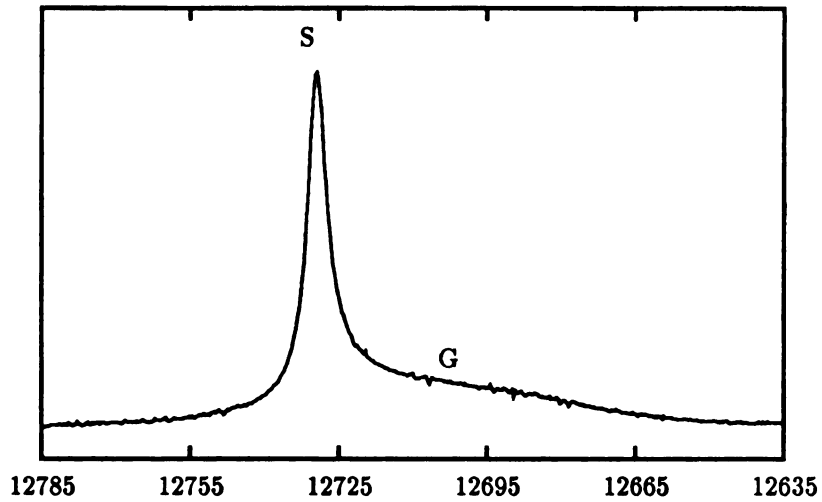


Figure 3.11: Double resonance spectra of the ${}^9\text{P}(6,3)$ transition. Soft inelastic $\Delta J = 1$ collisions with a large impact diameter result in the sharp spike marked S whereas the Gaussian marked G comes from the vibrational swapping mechanism. With sub-Doppler resolution, the two processes in the same transition can be time resolved separately.

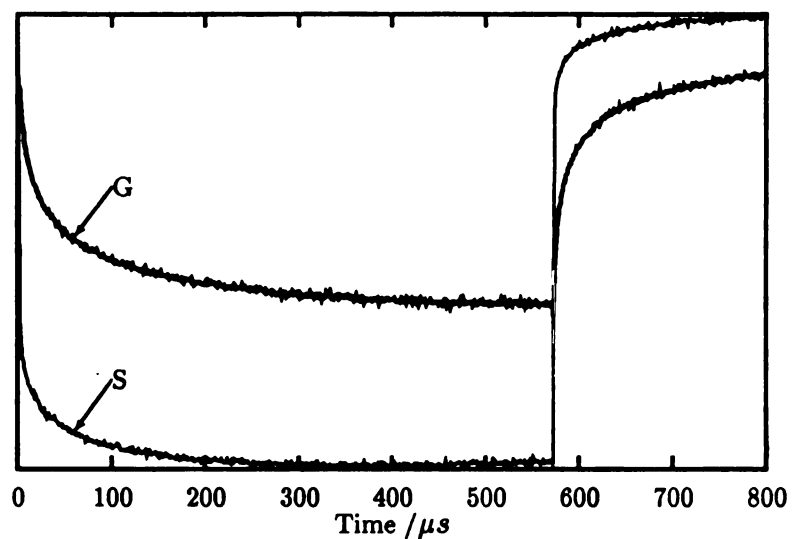


Figure 3.12: Time resolved spectra of the ${}^Q\text{P}(6,3)$ transition. G represents the signal from the Gaussian whereas S is from the spike. At time 0, the pump laser is turned off and relaxation is observed whereas at time $570\mu\text{s}$ the pump laser is turned on, and an increase in signal was observed. The difference between G and S can be seen at early time ($< 10\mu\text{s}$) where the $\Delta J = 1$ process dominates.

electro-optic switch system provides a *soft pulse* with a spectral bandwidth comparable to that of our steady state double resonance system. One of the main difficulties in building the system shown in Figure 3.9 was the need to switch the high voltage (± 2.1 kV) applied to the CdTe housing within less than $1 \mu\text{s}$. This required numerous tests of home made transformers by M. Rabb, who designed the high-voltage switching circuit used. Due to the heat generated by the high voltage switching, the maximum modulation frequency was limited to 10 kHz.

B. Data Acquisition

The time constant of the recording system and the electro-optic switching was checked using a Honeywell Model LK146C8 HgCdTe photovoltaic detector (100 MHz band width) with scattered light from the pump laser. The total system time constant measured was better than $1 \mu\text{s}$, which was the limit of the electro-optic switch.

An Infrared Associates Model HG-100 InSb photoconductive detector with matched pre-amplifier with 350 kHz cutoff frequency was used to record the spectra in this study. The pre-amplified detector signal was sent to a LECROY model 6810 transient digitizer and to a Stanford Research Associates SRS-510 lock-in amplifier at the same time in order to monitor the intensity while recording in the time domain as shown in Figure 3.9. Since the (transferred) spikes have very narrow spectral width, a frequency shift of the probe and/or the pump laser was easily noticeable by monitoring the output voltage level of the lock-in amplifier. Care was taken to ensure that the frequencies of both lasers were constant by monitoring the voltage level.

The LECROY model 6810 transient digitizer, which was controlled by an IBM-AT compatible microcomputer through an IEEE-488 interface, had a maximum acquisition rate of 5 MHz with single channel acquisition. The IEEE-488 interface board was an IO-tech Model 488 that was controlled by a National Instruments GPIB driver. By using the program supplied by LECROY, after some modifications, it was possible to obtain 1000 scans of 4096 data points in less than one hour. The acquired data were sent to a SUN 4-60 workstation through an Ethernet at the speed of 1 Mbit/sec,

where they were either converted into ASCII format for processing or archived. Due to the large size of the data set only interesting time intervals were extracted and then processed by either of two computer programs, GNUPLOT¹³⁴ or MATLAB.¹³⁵

Chapter 4

Results and Discussion

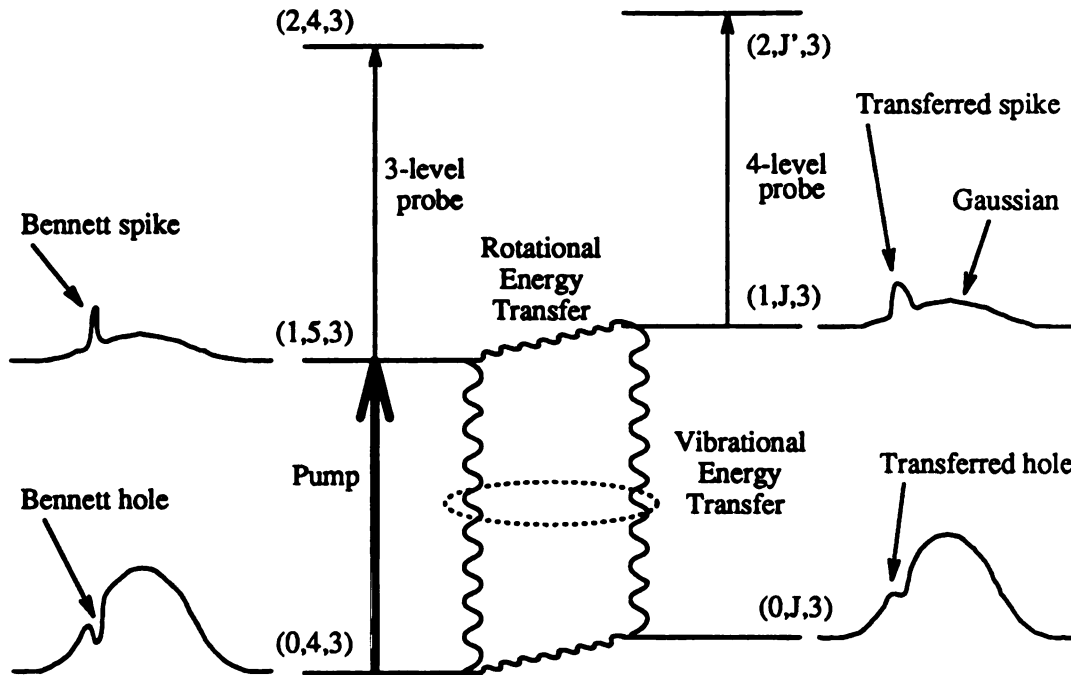


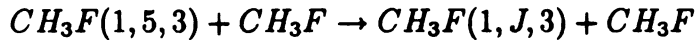
Figure 4.1: Graphical illustration of velocity distribution of molecules involved in the pump and probe. The Bennett hole can be studied by probing either the ${}^{\text{Q}}\text{P}(4,3)$ or the ${}^{\text{Q}}\text{Q}(4,3)$ transition while the Bennett spike can be done by using the ${}^{\text{Q}}\text{P}(5,3)$ transition in $2\nu_3 \leftarrow \nu_3$ band. The Bennett spike is collisionally transferred into different rotational levels and probed by four-level double resonance. It is not clear whether there exist transferred holes or not.

I. Introduction

Figure 4.1 is a graphic illustration of collisional energy transfer paths and their results on the velocity distribution of ${}^{13}\text{CH}_3\text{F}$ molecules perturbed by a pump laser. A CO_2 9P(32) laser depopulates molecules in a selective velocity group from the $(v, J, K) = (0, 4, 3)$ level to the $(1, 5, 3)$ level, thereby creating a Bennett hole in the lower level and a Bennett spike in the upper level. The ${}^{\text{Q}}\text{P}(5,3)$ transition in the $2\nu_3 \leftarrow \nu_3$ band was used to probe molecules excited by the pump in a 3-level double resonance. Molecules excited by the pump experience collisions that can change their rotational and/or vibrational levels, which are then probed in a four level double resonance.

Sharp transferred spikes observed in the $K = 3$ levels are the result of collisions

that change the rotational quantum number J by 1 ($\Delta J = \pm 1$; dipole interaction, parity changed) or by more than one ($\Delta J = \pm 2$; quadrupole interaction, parity unchanged, $\Delta J = \pm 3$; octopole interaction, parity changed). Due to the large impact parameters for majority of these collisions, molecules conserve many of their characteristics such as velocity, alignment, and orientation even after a number of collisions. These molecules are responsible for the sharp spike observed in the power modulation and a dispersion shape in the circular birefringence measurement. The widths of the transferred spikes increase as $|\Delta J| = |J_{probe} - J_{pump}|$ since collisionally induced large changes in J either require several collisions or collisions with small impact parameter, either of which smear out the characteristics of the molecules.



In the vibrational swapping collisions where the vibrational quantum numbers are exchanged between two collision partners, molecules probed in the four level double resonance originate from the ground vibrational level that had a nearly Gaussian velocity distribution. Therefore those molecules that contribute to the broad Gaussian lineshape observed in the double resonance do not show any sign of photo selection of their alignment or their orientation.



Another collision path that follows $\Delta K = 3n$ was observed in $K = 0, 3, 6, 9$ levels as a broad spike in the lineshape of the double resonance. Although directly pumped molecules are responsible for the absorption skewed to the spike direction, they do not conserve their alignment or their orientation as well as $\Delta K = 0$ process, probably because the change in the K quantum number requires a hard collision which destroys the photo selected alignment and/or orientation.



Our main concern in this chapter is about the sharp spike observed only from $K = 3$ levels in $^{13}CH_3F$ or from $K = 9$ in $^{12}CH_3F$. A lineshape study of transferred spikes in $^{12}CH_3F$ is discussed first. Then the lineshapes of intensity modulated or

polarization modulated double resonance of $^{13}\text{CH}_3\text{F}$ and its time resolved observation are described subsequent sections. In all of the spectra shown in this chapter the horizontal axis is the microwave frequency offset from the frequency of laser line used to generate the sidebands. The laser and the sign of the sideband is given in Table 4.1, for $^{12}\text{CH}_3\text{F}$ and in Table 4.5 for $^{13}\text{CH}_3\text{F}$.

II. Lineshape Study of Transferred Spikes in $^{12}\text{CH}_3\text{F}$

A. Three-Level Double Resonance

Three-level double resonances were observed while pumping either the $^{\text{Q}}\text{Q}(12,2)$ or the $^{\text{Q}}\text{R}(11,9)$ transitions in the ν_3 band with probe transitions in both the ν_3 fundamental band and in the $2\nu_3 \leftarrow \nu_3$ hot band. Examples of three-level double resonances for the two pump transitions with probe transitions in the fundamental band are shown in Figs. 4.2 and 4.3, while a three-level double resonance for the $^{\text{Q}}\text{R}(11,9)$ pump and a hot-band probe transition is shown in Fig. 4.4. Comparison of Fig. 4.2 and 4.3 demonstrated that pumping the $^{\text{Q}}\text{R}(11,9)$ transition is more effective than pumping the $^{\text{Q}}\text{Q}(12,2)$ transition for comparable laser power. This was not unexpected, because the linestrength is greater and the offset in frequency is smaller for the $^{\text{Q}}\text{R}(11,9)$ than for the $^{\text{Q}}\text{Q}(12,2)$ transition (Table 1.1). In addition, although strong three-level double-resonance spectra could be obtained for either system, the combination of pump and probe transitions for the $^{\text{Q}}\text{Q}(12,2)$ double resonances attainable with our system was such that no usable information about the pump power density could be obtained from the lineshapes. This was a result of the relative frequencies of the pump and probe transitions as well as the pump power available and is explained elsewhere.¹¹ Finally, because the separation in frequency is greater for larger K , the probe transitions were well separated when the $^{\text{Q}}\text{R}(11,9)$ transition was pumped, whereas there was strong overlapping with the $^{\text{Q}}\text{Q}(12,2)$ pump. In fact, with the $^{\text{Q}}\text{Q}(12,2)$ pump, transferred spikes are seen as a result of the simultaneous pumping of the $^{\text{Q}}\text{Q}(12,1)$ transition. For all of these reasons, we chose to concentrate on double resonances obtained with the $^{\text{Q}}\text{R}(11,9)$ pump. Analysis of the lineshapes

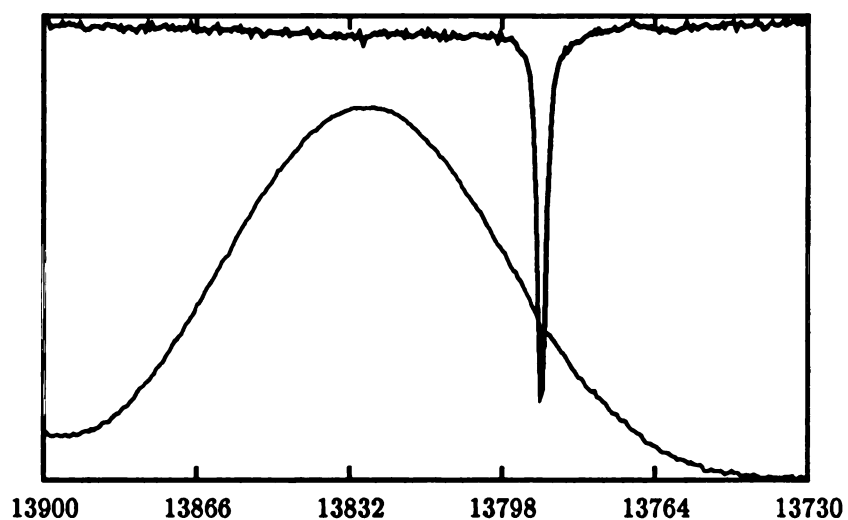


Figure 4.2: Three-level infrared-infrared double-resonance spectra of the ${}^{\text{Q}}\text{P}(12,2)$ transition in the ν_3 band of ${}^{12}\text{CH}_3\text{F}$; the ${}^{\text{Q}}\text{Q}(12,2)$ transition in the same band was pumped by the $9\text{P}(20)$ ${}^{12}\text{C}^{16}\text{O}_2$ laser. The horizontal axis is the (negative) microwave frequency (MHz) offset from the $9\text{R}(12)$ ${}^{13}\text{C}^{16}\text{O}_2$ laser. The lower trace is the single + double resonance and the upper trace is the double resonance.

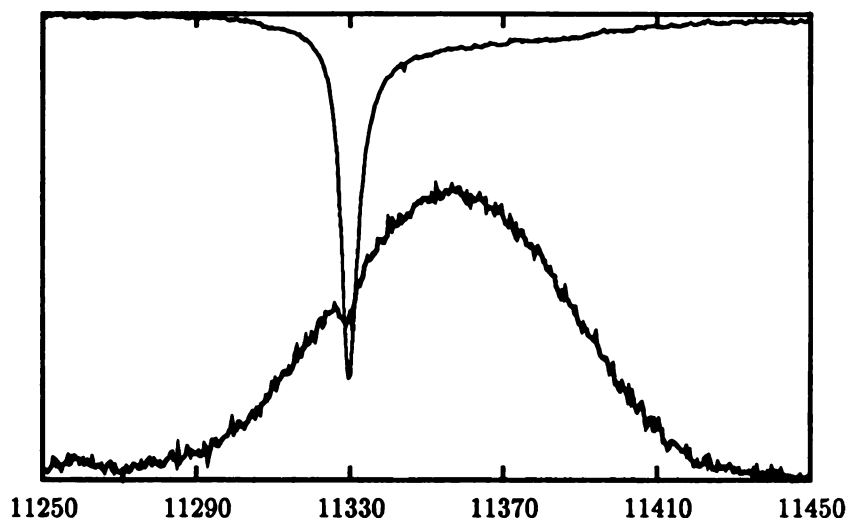


Figure 4.3: Three-level Infrared-infrared double resonance spectra of the ${}^{\text{Q}}\text{Q}(11,9)$ transition in the ν_3 band of ${}^{12}\text{CH}_3\text{F}$; the ${}^{\text{Q}}\text{R}(11,9)$ transition in the same band was pumped by the $9\text{P}(22) {}^{12}\text{C}^{18}\text{O}_2$ laser. The horizontal axis is the microwave frequency (MHz) offset from the $9\text{P}(20) {}^{12}\text{C}^{16}\text{O}_2$ laser. The lower trace is the single + double resonance and the upper trace is the double resonance. The broad line was recorded after the first demodulation. For simplicity, the term *single resonance signal* is used to indicate this part in the text, since it is the average value of the single resonance and the double resonance. The spectrum with a sharp spike was recorded after the second demodulation. This part is called the *double resonance signal* in the text; it is the double resonance minus the single resonance. The area of the Bennett hole measured in the single resonance signal was $\sim 1\%$ of the total area, which implies that $\sim 2\%$ of the molecules in the ground state are excited by the laser pumping.

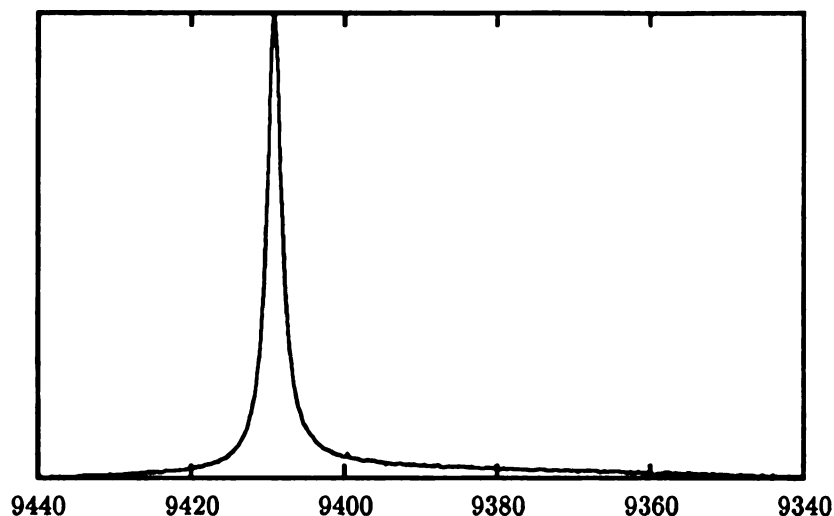


Figure 4.4: Three-level infrared-infrared double-resonance spectrum of the ${}^{\text{Q}}\text{Q}(12,9)$ transition in the $2\nu_3 \leftarrow \nu_3$ band of ${}^{12}\text{CH}_3\text{F}$; the ${}^{\text{Q}}\text{R}(11,9)$ transition in the ν_3 band was pumped by the 9P(22) ${}^{12}\text{C}^{18}\text{O}_2$ laser. The horizontal axis is the (negative) microwave frequency (MHz) offset from the 9P(36) ${}^{12}\text{C}^{18}\text{O}_2$ laser.

for the ${}^{\text{Q}}\text{R}(11,9)$ double resonances showed that the area of the Bennett hole produced in a fundamental band probe transition was of the order of 2% of the area of the single-resonance transition, which gives an indication of the extent of pumping for the experiments reported here.

The ${}^{\text{Q}}\text{R}(11,9)$ was also more favorable for the experiments here because the pump and probe transitions of interest (those with $k = 9$) were well resolved. For low k in CH_3F , the transitions are so close together that the ${}^{\text{Q}}\text{Q}(12,1)$ transition is also pumped when the ${}^{\text{Q}}\text{Q}(12,2)$ is pumped.

The three-level lineshapes were analyzed as described in the previous section (and more thoroughly elsewhere¹¹) in order to obtain a value for the width of the Bennett spike produced in the pumped level in the $\nu_3 = 1$ state. For these experiments, the pump laser power was typically 1 W and the beam diameter was ~ 10 mm. The resulting spike in the upper state population was essentially Lorentzian with a halfwidth at halfheight that was ~ 1.4 MHz.

B. Four-Level Double Resonance

Four-level double resonances were observed for each of the three pump transitions – ${}^{\circ}\text{R}(11,9)$, ${}^{\circ}\text{Q}(12,2)$, and ${}^{\circ}\text{R}(31,4)$ – but for the high- J pump only one four-level effect, on the ${}^{\circ}\text{P}(30,4)$ fundamental transition, was strong enough to be observed easily. Although many four-level effects could be seen with the ${}^{\circ}\text{Q}(12,2)$ pump, for the reasons given in the previous section, I report results of lineshape analyses only for experiments with the ${}^{\circ}\text{R}(11,9)$ pump transition. Fig. 4.5 is a plot of the four-level effects on some ${}^{\circ}\text{P}(14,K)$ transitions caused by pumping the ${}^{\circ}\text{Q}(12,2)$ transition. The simultaneous pumping of the $K = 1$ and 2 transitions is clearly seen. Fig. 4.6 shows the four-level effects, recorded by the double-modulation procedure, on the $\text{Q}(9,3) - \text{Q}(9,9)$ and $\text{Q}(12,3) - \text{Q}(12,9)$ hot band transitions observed with the ${}^{\circ}\text{R}(11,9)$ pump. These transitions occur in the same sweep because one set absorbs the negative sideband and the other absorbs the positive sideband. Although four-level effects are seen for all of the transitions, obvious transferred spikes are seen only for the $\text{Q}(12,9)$ and $\text{Q}(9,9)$ lines. In addition extra intensity enhancement is apparent for the transitions with $K = 6$ and $K = 3$ showing again the $\Delta k = 3n$ selection rule for direct transfer of rotational energy by collision. The four-level effects on the transitions for which $K \neq 9 \pm 3n$ are attributed to $V - V$ energy transfer (vibrational energy swapping).

A series of transferred spikes for both fundamental and hot band probes were observed with the ${}^{\circ}\text{R}(11,9)$ pump and analyzed by means of the four-level double-resonance lineshape equation given above. The lasers used for the probing in these experiments are shown with the calculated center frequencies and microwave offsets in Table 4.1.

Examples of the lineshapes are shown in Figures 4.7 and 4.8 and an example of the result of the fitting is shown in Figure 4.9 assuming single spike and in Figure 4.10 assuming two spikes. They show that while the transferred spike part of the double-resonance lineshape cannot be fit satisfactorily with one K-S function, a sum of two K-S functions provides a very precise representation. The fitted values of the r.m.s. change in velocity that results from collision(s) that bring the molecules

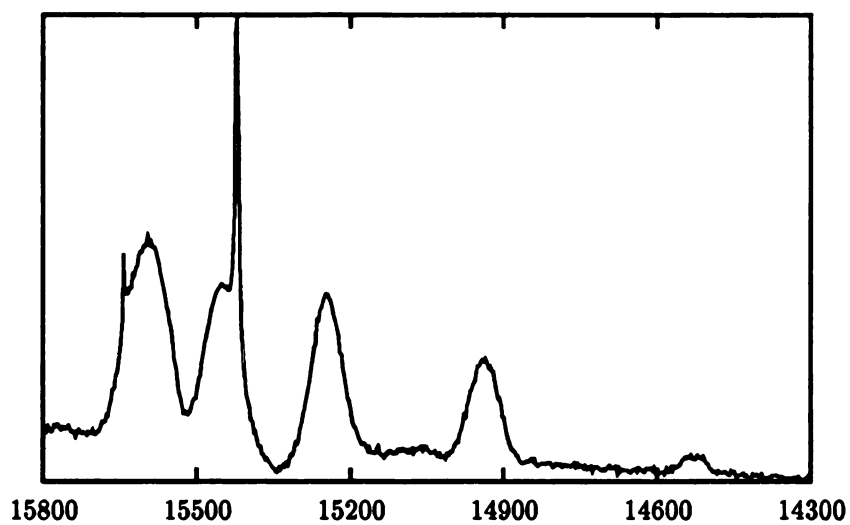


Figure 4.5: Four-level infrared-infrared double-resonance of the ${}^{\text{Q}}\text{P}(14,0)$ - ${}^{\text{Q}}\text{P}(14,5)$ transitions in the $2\nu_3 \leftarrow \nu_3$ band of ${}^{12}\text{CH}_3\text{F}$. The ${}^{\text{Q}}\text{Q}(12,2)$ and ${}^{\text{Q}}\text{Q}(12,1)$ transitions in the ν_3 band, were pumped simultaneously by the $9\text{P}(20)$ ${}^{12}\text{C}^{16}\text{O}_2$ laser. The horizontal axis is the (negative) microwave frequency (MHz) offset from the $9\text{P}(12)$ ${}^{13}\text{C}^{16}\text{O}_2$ laser. Transferred spikes are seen on both the ${}^{\text{Q}}\text{P}(14,2)$ and ${}^{\text{Q}}\text{P}(14,1)$ transitions. (The ${}^{\text{Q}}\text{P}(14,1)$ and ${}^{\text{Q}}\text{P}(14,0)$ transitions are almost completely overlapped.)

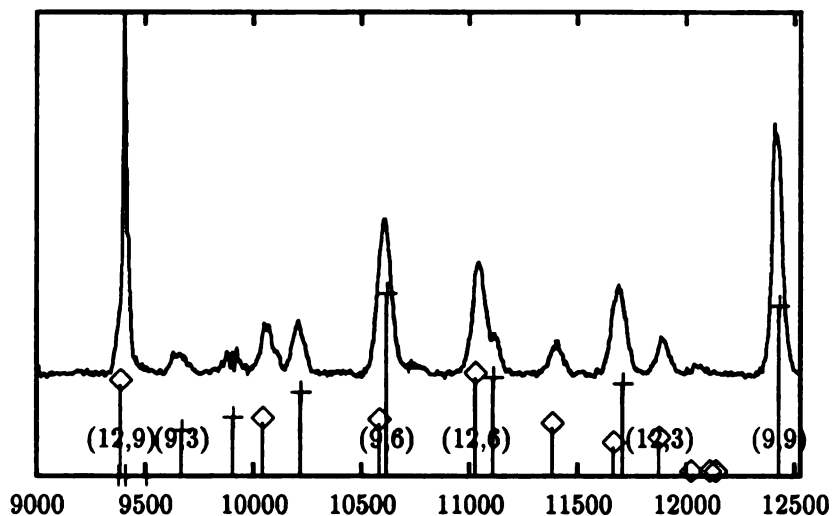


Figure 4.6: Four level infrared-infrared double resonance of the ${}^{\circ}\text{Q}(9,3)$ - ${}^{\circ}\text{Q}(9,9)$ and ${}^{\circ}\text{Q}(12,3)$ - ${}^{\circ}\text{Q}(12,9)$ transitions in the $2\nu_3 \leftarrow \nu_3$ band of ${}^{12}\text{CH}_3\text{F}$. The ${}^{\circ}\text{Q}(12,K)$ transitions are the result of absorption of the negative sideband while ${}^{\circ}\text{Q}(9,K)$ transitions are the result of absorption of the positive sideband, both of which are present in the probe radiation. The horizontal axis is the microwave frequency (MHz) offset from the $9\text{P}(36)$ ${}^{12}\text{C}^{16}\text{O}_2$ laser, negative for ${}^{\circ}\text{Q}(12,K)$, positive for ${}^{\circ}\text{Q}(9,K)$. The ${}^{\circ}\text{R}(11,9)$ transition in the ν_3 fundamental band was pumped by the $9\text{P}(22)$ ${}^{12}\text{C}^{18}\text{O}_2$ laser. Calculated frequencies and relative intensities for normal single resonance spectra are plotted below the recorded spectra with + for $J=9$ and with \diamond for $J=12$.

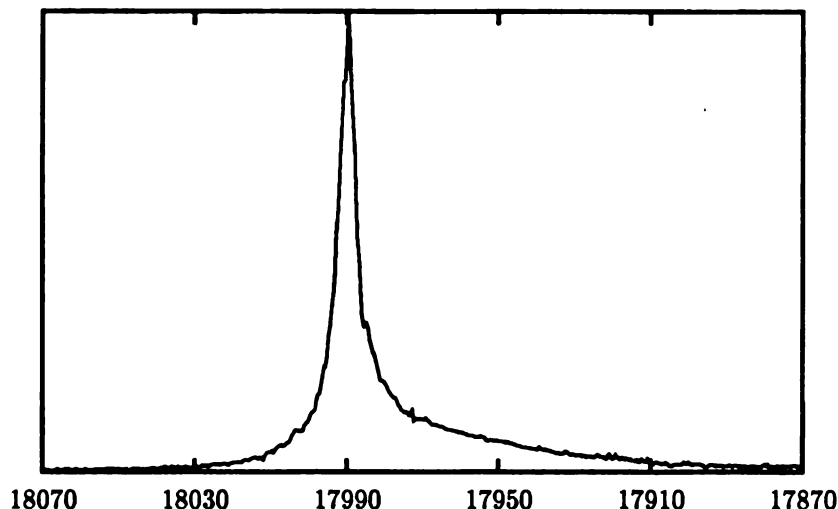


Figure 4.7: Four-level infrared-infrared double-resonance spectrum of the ${}^{\text{Q}}\text{R}(13,9)$ transition in the $2\nu_3 \leftarrow \nu_3$ band of ${}^{12}\text{CH}_3\text{F}$; the ${}^{\text{Q}}\text{R}(11,9)$ transition in the ν_3 band was pumped by the 9P(22) ${}^{12}\text{C}^{16}\text{O}_2$ laser. The horizontal axis is the (negative) microwave frequency (MHz) offset from the 9P(36) ${}^{12}\text{C}^{16}\text{O}_2$ laser.

into the states probed are shown in Tables 4.4 and 4.3 for hot band ($2\nu_3 \leftarrow \nu_3$ band) and fundamental (ν_3 band) transitions, respectively. The values for the hot-band transitions are plotted in Figure (4.11) against ΔJ , where ΔJ is the difference between the J value for the lower state of the probe and the upper state of the pump transition. In view of the relatively slow rate of direct vibrational energy transfer, the r.m.s. changes in velocity for the hot band probes reflect the changes as a result of collisionally-induced rotational transitions in $v_3 = 1$. The values given in Table 4.4 and plotted in Figure 4.11 parallel the values obtained earlier for ${}^{13}\text{CH}_3\text{F}$.²⁸ They increase monotonically as ΔJ increases in absolute value.

The ratio of the area of the broad component to the narrow component of the transferred spikes also increases as ΔJ increases (shown in Figure 4.13). If the broad component is interpreted as resulting from collisions with small impact parameter, this is indication that a greater proportion of hard collisions is required for rotational energy transfer with larger ΔJ . Finally, the ratio of the areas of the Gaussian to spike contributions also increases as ΔJ increases, which indicates that the time required

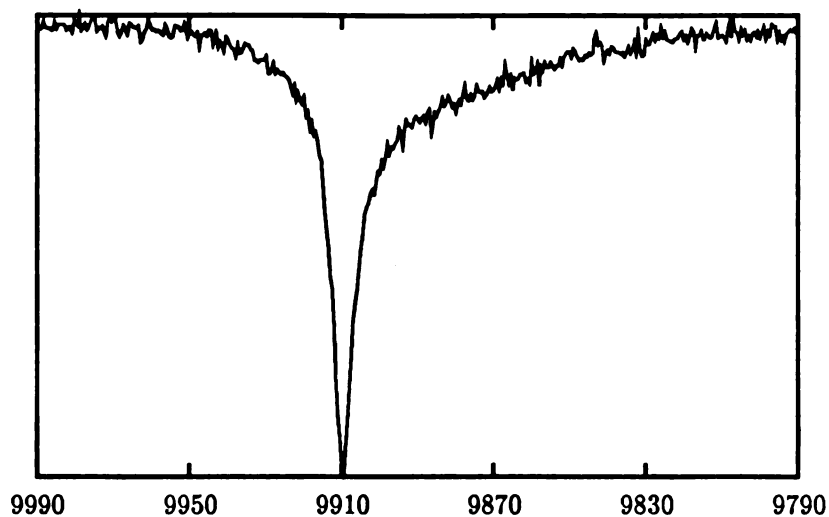


Figure 4.8: A typical double resonance spectrum in the fundamental band. (${}^{\text{Q}}\text{R}(11,9)$ transition in the ν_3 band is shown.)

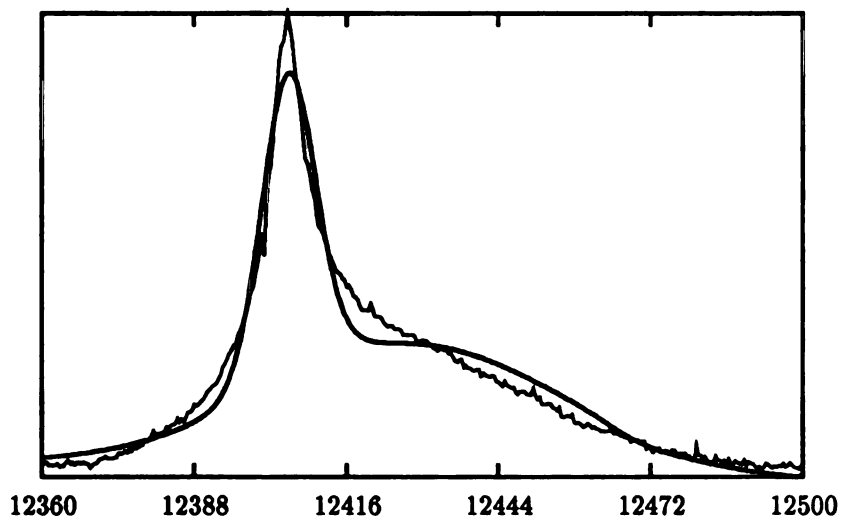


Figure 4.9: Comparison of observed (noisy line) and calculated (smooth line) four-level double-resonance spectrum for the ${}^{\text{Q}}\text{Q}(9,9)$ transition in the $2\nu_3 \leftarrow \nu_3$ band of ${}^{12}\text{CH}_3\text{F}$; the ${}^{\text{Q}}\text{R}(11,9)$ transition in ν_3 band was pumped by the $9\text{P}(22)$ ${}^{12}\text{C}^{18}\text{O}_2$ laser. The horizontal axis is the microwave frequency (MHz) offset from the $9\text{P}(36)$ ${}^{12}\text{C}^{16}\text{O}_2$ laser. The calculated curve is the best fit to a single Keilson-Storer function + Gaussian.

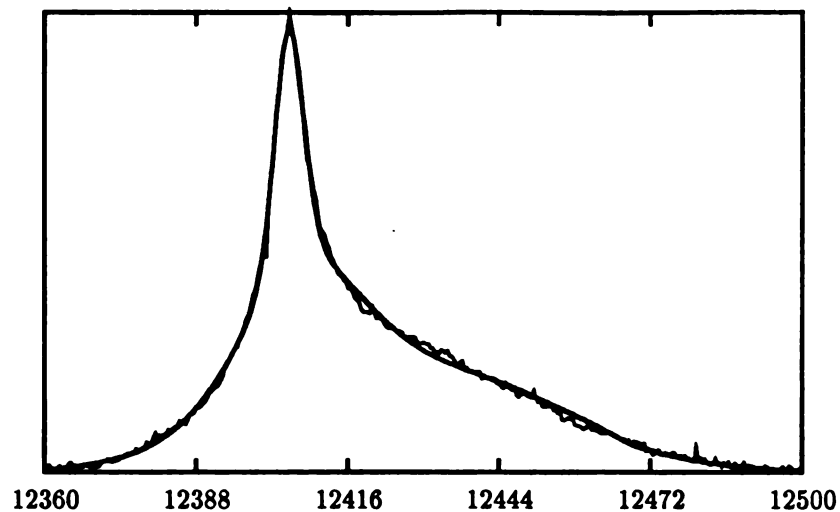


Figure 4.10: Comparison of observed (noisy line) and calculated (smooth line) four-level double-resonance spectrum for the same pump-probe combination and horizontal axis as shown in Fig. 8. Here, the calculated curve is the best fit to a sum of two Keilson-Storer function + Gaussian.

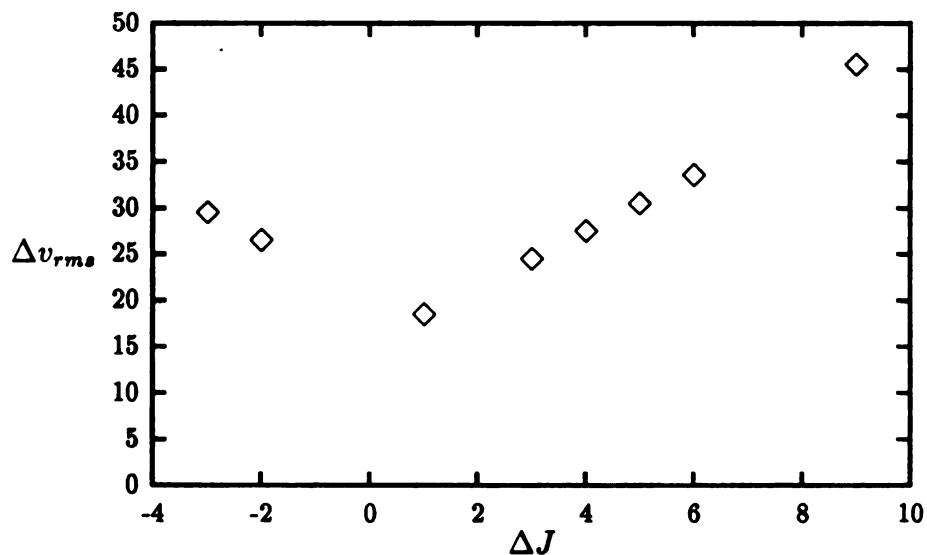


Figure 4.11: Plot of the ratio of the area of the wide spike to that of the narrow spike vs. ΔJ for the four-level double resonances listed in Table 4.2.

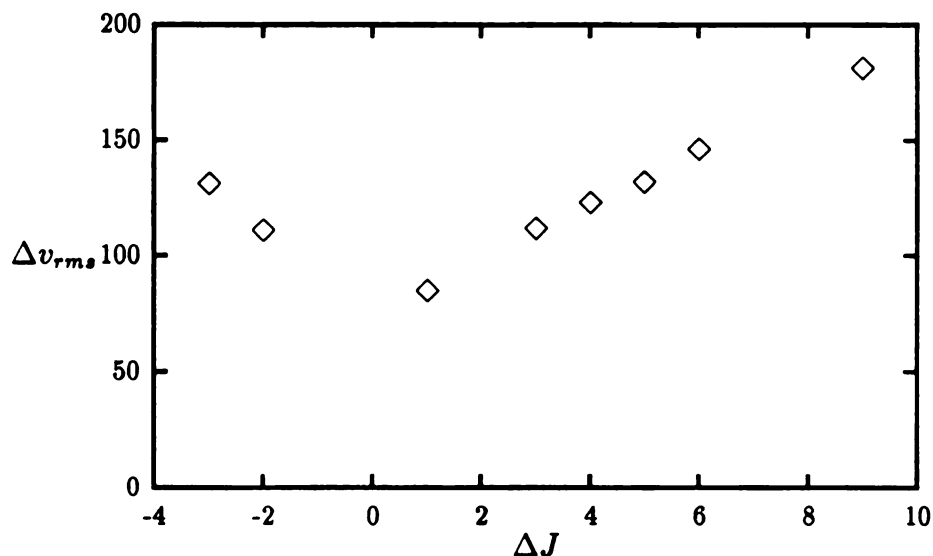


Figure 4.12: Plot of the r.m.s. change in speed vs. ΔJ for the molecules that contribute to the broad spike for the four-level double resonance transitions listed in Table 4.2.

for rotational energy transfer increases as ΔJ increases.

Contrary to our perception about transferred holes and spikes, the Δv_{rms} values calculated for the fundamental probes in Table 4.3 depend on the upper state of the probe transitions, which implies that there may be no transferred holes or that the contribution of the transferred holes to the observed signal may be small. Considering that the sharp spikes originate from directly pumped molecules, this is reasonable since it is highly improbable that only molecules in the selected velocity group fill up the burned hole in the collisional process. This question could probably be answered by probing transitions in different vibrational modes such as ν_6 while pumping the same ${}^Q\text{R}(4,3)$ transition in the ν_3 band. Unfortunately our IMSL system does not cover the ν_6 band frequency region.

In principle, it should be possible to make a quantitative comparison of rate constants for collisional rotational energy transfer and $V - V$ processes by comparison of the intensities of the double resonance effects. We show in the Appendix that by comparison of relative intensities of three-level and four-level double resonance effects

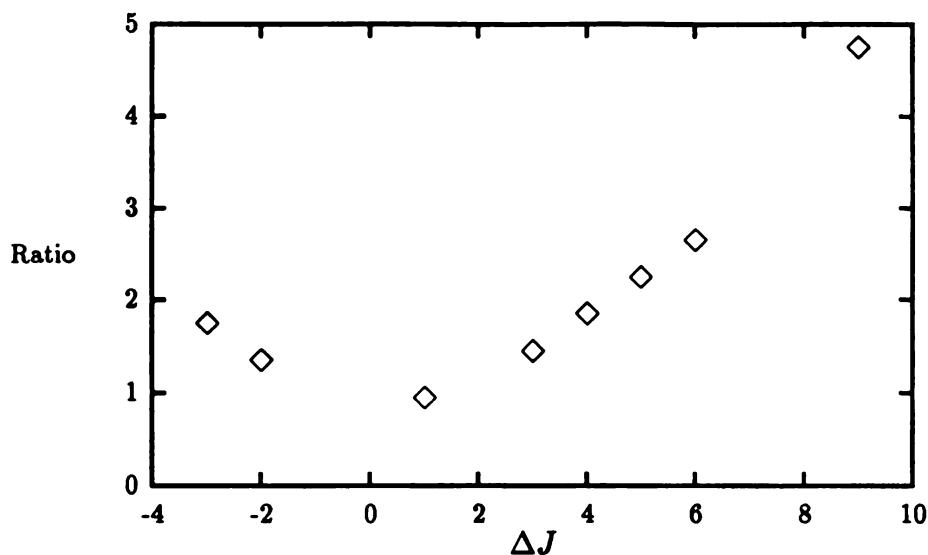


Figure 4.13: Plot of the ratio of the area of the wide spike to that of the narrow spike *vs.* ΔJ for the four-level double resonances.

under the same experimental conditions that it is possible to determine the ratio of the effective rate constant for collisional energy transfer from the upper level of the pump to the lower level of the probe, either directly or through some other level, to the effective rate constant for loss of population from the lower level of the probe by any mechanism.

If the ${}^{\text{Q}}\text{R}(11,9)$ transition in the ν_3 band is pumped, the three-level double resonance effect on the ${}^{\text{Q}}\text{Q}(12,9)$ transition and the four-level effects on the ${}^{\text{Q}}\text{Q}(9,9)$ and ${}^{\text{Q}}\text{Q}(13,9)$ transitions, all in the $2\nu_3 \leftarrow \nu_3$ band, can be recorded without changing laser lines. Furthermore, the intensity-stabilization system in our IMSL source insures that the intensity of the sideband used to monitor these lineshapes remains constant. Thus, by taking appropriate ratios of the narrow spike, broad spike, and Gaussian contribution of each of the two four-level double-resonance lineshapes to the intensity of the three-level lineshape recorded under the same conditions, the corresponding ratios of rate constants can be determined.

For the transitions studied, the ratios at sample pressure 20 mTorr and $\sim 297\text{K}$

are 0.183, 0.110, and 0.0044 for the narrow spike, broad spike, and Gaussian, respectively, for the ${}^{\text{Q}}\text{Q}(13,9)$ transition and 0.116, 0.195, and 0.0064 for the corresponding components of the ${}^{\text{Q}}\text{Q}(9,9)$ transition, respectively. The uncertainty in these ratios is rather large, perhaps 10–15 %.

The lower level of the ${}^{\text{Q}}\text{Q}(13,9)$ transition can be reached from the upper level of the ${}^{\text{Q}}\text{R}(11,9)$ pump by a single $\Delta J = +1$ collisionally-induced transition, while the lower level of the ${}^{\text{Q}}\text{Q}(9,9)$ transition requires $\Delta J = -3$ from the upper level of the pump. The population ratios show that the effective rate constant for production of the sharp spike is more than 50 % larger than the rate constant for production of the broad spike for the ${}^{\text{Q}}\text{Q}(13,9)$ transition, whereas the reverse is true for the ${}^{\text{Q}}\text{Q}(9,9)$ transition. This provides additional evidence for either more collisions or harder collisions required to cause a $|\Delta J| = 3$ than a $|\Delta J| = 1$. At a pressure of 20 mTorr, the Gaussians are only 1.5 % and 2.1 % as intense as the overall spikes for the ${}^{\text{Q}}\text{Q}(13,9)$ and ${}^{\text{Q}}\text{Q}(9,9)$ transitions, respectively. The sum of the population ratios is slightly larger for the ${}^{\text{Q}}\text{Q}(9,9)$ than for the ${}^{\text{Q}}\text{Q}(13,9)$ transition (0.32 vs 0.30), which would be expected for thermal equilibration of the populations of the rotational states in $v_3 = 1$. However, comparison of these ratios for different transitions requires the assumption that the rate constants for effective loss of population from these levels is the same, which is probably not the case.

C. Summary

As expected, there is a strong parallel between the results obtained for ${}^{12}\text{CH}_3\text{F}$ in this work and those obtained for ${}^{13}\text{CH}_3\text{F}$ in a previous study from this laboratory.²⁸ The principal results are as follows:

1. Transferred spikes are seen in the double-resonance probe transitions in CH_3F only when the quantum numbers for the pump and probe transitions obey the collisional selection rule $\Delta k = 3n$ where n is a positive or negative integer. Sharp spikes are seen only for $\Delta k = 0$.
2. Transferred spikes are seen for all values of J for which the selection rule in (1) is satisfied. For fundamental pump and hot band probe the change in velocity

on collision increases monotonically as the J of the lower state of the probe gets further away from the J of the upper state of the pump in either direction. For fundamental pump and probe the change in velocity generally increases as the difference in the J values of either the lower or upper states of the transition increase.

3. The lineshapes of the transferred spikes are very well represented by a theoretical equation based on a collision kernel that is the sum of two Keilson-Storer functions.
4. The area of the broad component of a transferred spike increases relative to the area of the narrow component as ΔJ increases.
5. A Gaussian-shaped component, centered at the resonance frequency of the transition and with the expected Doppler width, is observed as a double-resonance effect for all fundamental and hot-band transitions. For transitions with both spike and Gaussian components, the area of the Gaussian increases relative to the spike as ΔJ increases.

As mentioned in the previous study,²⁸ the transferred spikes for $|\Delta J| > 1$ do not obey dipole selection rules, so there is a question as to whether these effects occur as a series of dipole-allowed collisionally-induced transitions or as one or more transitions with $|\Delta J| > 1$. Arguments have been presented for both possibilities, but as of yet we do not have direct evidence for either mechanism. Recent time-resolved infrared-millimeter wave results have been interpreted by means of a computer simulation that included both mechanisms with the result that for $|\Delta J| > 2$ or 3, the effects of single collisions with large ΔJ dominate. This is a question that could in principle be answered by time-resolution of the transferred spikes and some preliminary time resolved experiments are described in section 3.

III. Saturation Absorption Spectroscopy in $^{13}\text{CH}_3\text{F}$

The famous $^{\text{Q}}\text{R}(4,3)$ transition in the ν_3 band of $^{13}\text{CH}_3\text{F}$, whose transferred spikes were studied by Matsuo and Schwendeman,²⁸ can be pumped with a $^{12}\text{CO}_2$ gas laser

unlike the ${}^Q\text{R}(11,9)$ transition of ${}^{12}\text{CH}_3\text{F}$ which requires an isotopic ${}^{12}\text{C}^{18}\text{O}_2$ gas laser. Therefore, we could pump this transition with our flowing gas laser which can deliver moderately high power (1-5 W). The fate of the molecules pumped in the ${}^Q\text{R}(4,3)$ transition is the subject throughout the last portion of this dissertation.

A. Three-level Double Resonance Lineshape

Difference in the lineshape of three-level double resonance spectra was observed between parallel (σ^\pm/σ^\pm) and perpendicular (σ^\pm/π) configurations. When the ${}^Q\text{P}(5,3)$ $2\nu_3 \leftarrow \nu_3$ hot band was recorded with a π probe while a σ^\pm polarization pumps the ${}^Q\text{R}(4,3)$ ν_3 transition, its linewidth is narrower than the one recorded with both σ^\pm pump and probe (Figure 4.14). Contrary to the previous report by Leite *et al.*⁶² where a wider linewidth was observed in σ^\pm/π configuration, a broader lineshape was observed in the σ^\pm/σ^\pm configuration (thick line) compared with the spectrum with σ^\pm/π (thin line) under the same condition. The different observation is attributed partly to the fact that our energy levels are in a cascade system whereas a folded three level (two in terms of energy levels) system was studied by Leite *et al.*, but mainly to the fact that saturation broadening is dominant in our experiment, whereas collision broadening is dominant in Leite's experiment.

A surprising observation is that the absolute intensity from the parallel configuration experiment is smaller than from the perpendicular configuration one (Figure 4.15) contrary to a three-level calculation.¹³⁶ It is possible, even after careful control of the experimental conditions, that some experimental errors such as intensity difference in the two experiments or phase settings in the lock-in amplifier led to the discrepancies. Or, since the three-level calculation did not consider m changing collisions this may imply the m changing collisions are important in the theory, as pointed out by Leite *et al.*^{62,63}

At low pressure, where the effect of phase-changing collisions is small, a dip (or a splitting depending on the point of view) appeared at the center frequency of the spike as others have reported.^{74,77,137,78,11} The dip recorded under the σ^\pm/σ^\pm configuration is wider, as shown in Figures 4.16 and 4.17. It is obvious in each of the figures that

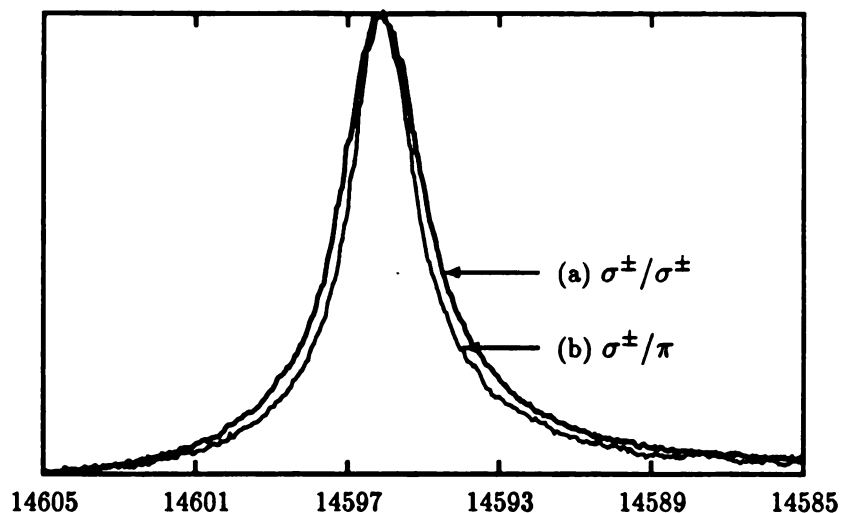


Figure 4.14: Three-level double resonance spectra of ${}^Q\text{P}(5,3)$ transition in the $2\nu_3 \leftarrow \nu_3$ band while the ${}^Q\text{R}(4,3)$ transition in the ν_3 fundamental band was pumped. The intensities of both peaks were normalized. (a) σ^\pm probe and σ^\pm pump is broader than (b) π probe and σ^\pm pump. Sample pressure was 19 *mTorr*.

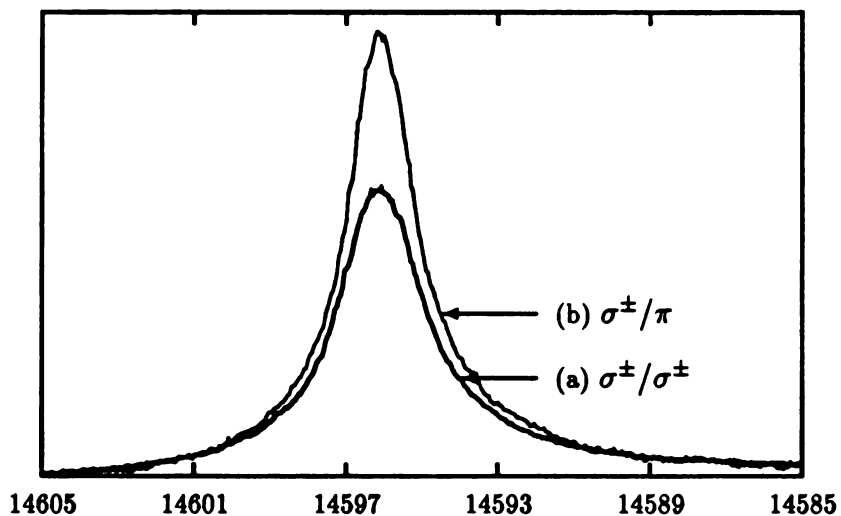


Figure 4.15: Three-level double resonance spectra of the ${}^Q\text{P}(5,3)$ transition in the $2\nu_3 \leftarrow \nu_3$ band while the ${}^Q\text{R}(4,3)$ transition in the ν_3 fundamental band was pumped. (a) σ^\pm probe and σ^\pm pump is weaker than (b) π probe and σ^\pm pump. Sample pressure was 19 *mTorr*.

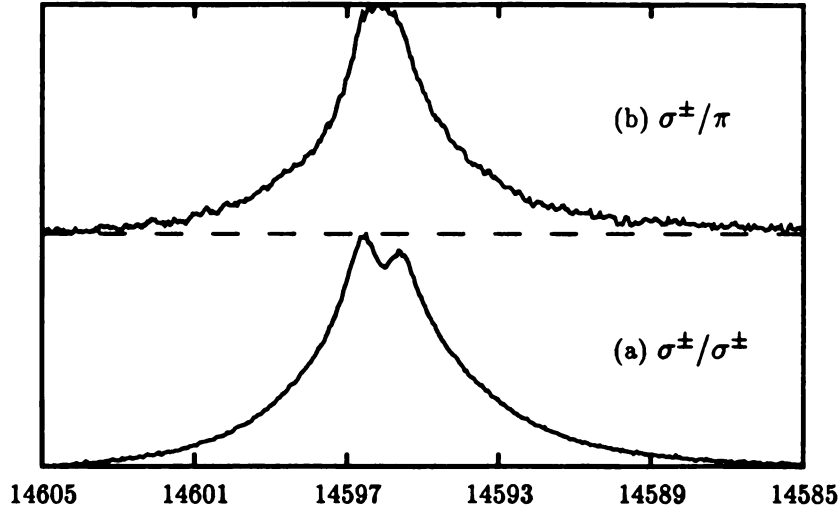


Figure 4.16: Pump/probe polarization dependence of three-level double resonance observed in the $^{\text{Q}}\text{P}(5,3)$ transition, recorded with 3 mTorr sample.

the lower trace, recorded with the parallel configuration, is wider in the splitting and broader in width than the upper trace obtained with the perpendicular configuration.

These observations agree with the three-level calculation considering the m selection rules ($\Delta m = \pm 1$ for perpendicular configuration and $\Delta m = 0$ for parallel configuration) and appropriate rotational line strengths. The calculated results are plotted in Figure 4.18. Due to the inhomogeneous beam profile of the pump laser as a result of the rapid divergence after the electro-optic modulator, only qualitative comparisons were made.

As the pressure increases, phase changing collisions become important and the dip decreases as shown in figure 4.19. Based on the pressure dependence the dip seems to be the result of velocity selective optical pumping for reasons similar to those explained by Liao *et al.*^{82,81}

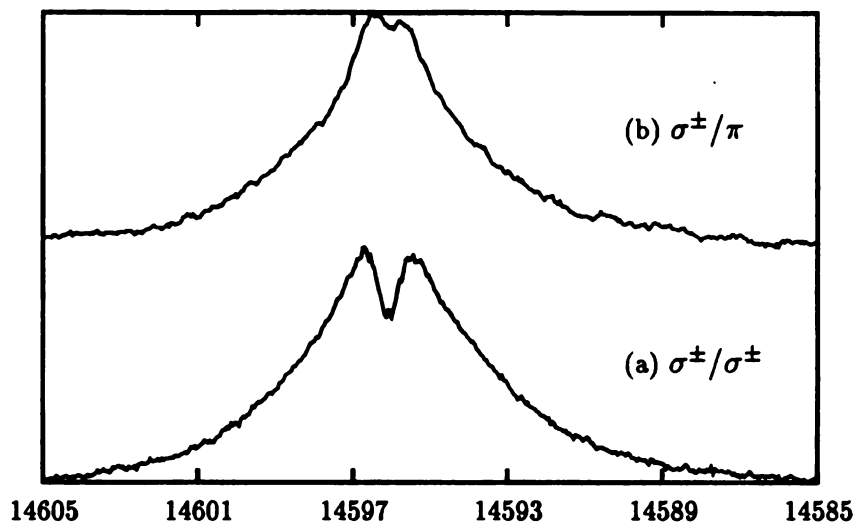


Figure 4.17: Pump/probe polarization dependence of three-level double resonance observed in the ${}^9\text{P}(5,3)$ transition, recorded with 1.5 mTorr sample.

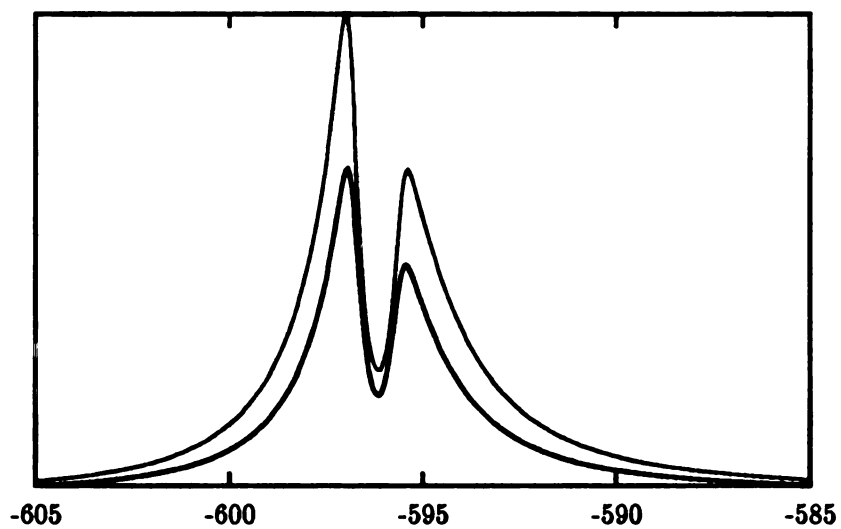


Figure 4.18: Calculated three level double resonance lineshape under (a) thin line: σ^\pm/σ^\pm (b) thick line: σ^\pm/π configurations, respectively.

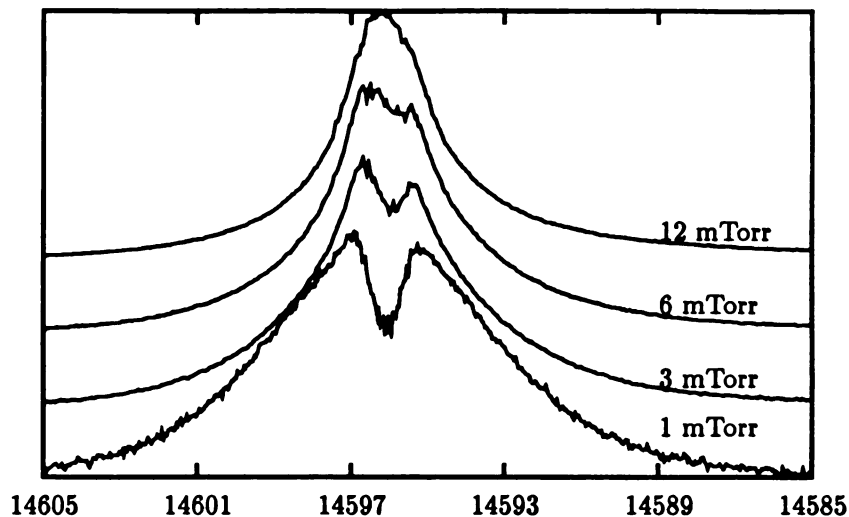


Figure 4.19: Pressure dependence of three-level double resonance observed in ${}^Q\text{P}(5,3)$ transition. To suppress relatively slow four-level contributions, the pump laser is optically modulated at 1 kHz.

B. Four-Level Double Resonance Lineshape

Although the absolute intensity of the four-level double resonance signal is stronger in the perpendicular configuration than in the parallel configuration, as in three-level double resonance, their lineshapes after intensity normalization are practically the same, as shown in Figure 4.20. The slight mismatch in the baseline most likely results from the difference in pump laser intensity for the two configurations.

At low pressures, at which a dip was observed in the three-level double resonance signal of the ${}^Q\text{P}(5,3)$ transition, a similar dip was observed in four-level double resonance when the probe laser was tuned to the ${}^Q\text{R}(4,3)$ and ${}^Q\text{R}(6,3)$ transitions under parallel configuration. Observed four-level dips are shown in Figures 4.21 and 4.22 for ${}^Q\text{P}(6,3)$ and ${}^Q\text{P}(4,3)$ in the $2\nu_3 \leftarrow \nu_3$ band, respectively. In Figure 4.21, the dip disappears as pressure increases, probably because collision broadening becomes an important factor. The observed signal is extremely weak and requires hours of data averaging. An attempt to reproduce this observation failed and no further attempt has been tried as yet. The dip was observable only under parallel configuration but not

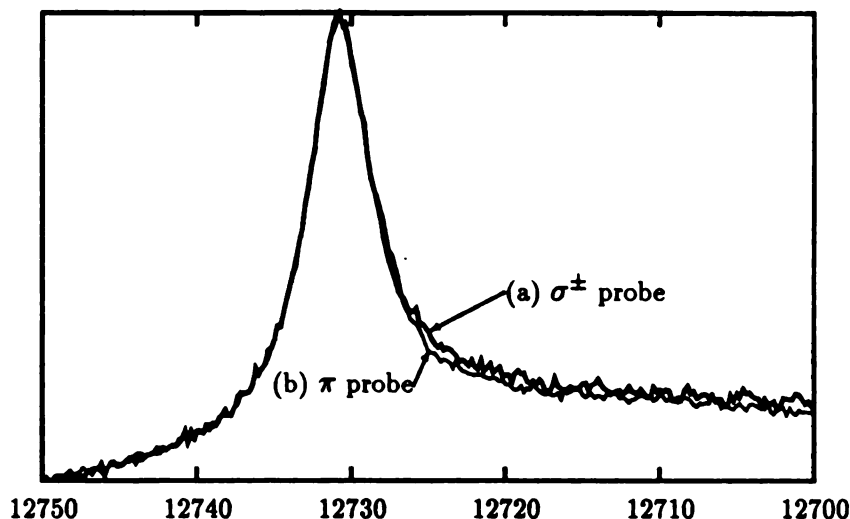


Figure 4.20: Four-level double resonance lineshape of the ${}^Q\text{P}(6,3)$ transition recorded with σ^\pm pump and (a) σ^\pm probe (thick line) (b) π probe (thin line). The two peaks had different intensity values and were normalized for comparison. Sample pressure was 21 mTorr.

with perpendicular configuration, in accordance with the report by Zou and Bloembergen.¹³⁸ The four-level dip was not observed in the ${}^Q\text{P}(7,3)$ transition, however. (Figure 4.23).

By comparing Figures 4.21 and 4.19, two differences are noticeable between three- and four-level dips. Unlike the three-level dip, the peak at higher frequency is stronger in the four-level dip. The width of the dip in the four-level is experimentally larger than the one in the three-level experiment. Although the cause of the dip is yet to be investigated theoretically and experimentally, it is possible that the same physical phenomena that create the dip in the three-level lineshape, namely either an optical Autler-Townes effect or velocity selective optical pumping, or both, have caused this observation. If the off-diagonal terms of the two pumped levels (ρ_{ab}) in a density matrix representation are coupled into the four-level scheme via elastic collisions, the dip may be calculated in the same way that the three-level calculations were calculated. That is to say the coherence is transferred via collision (*collisional coherence transfer*). Knowing that elastic collisions partially thermalize the velocity distribution

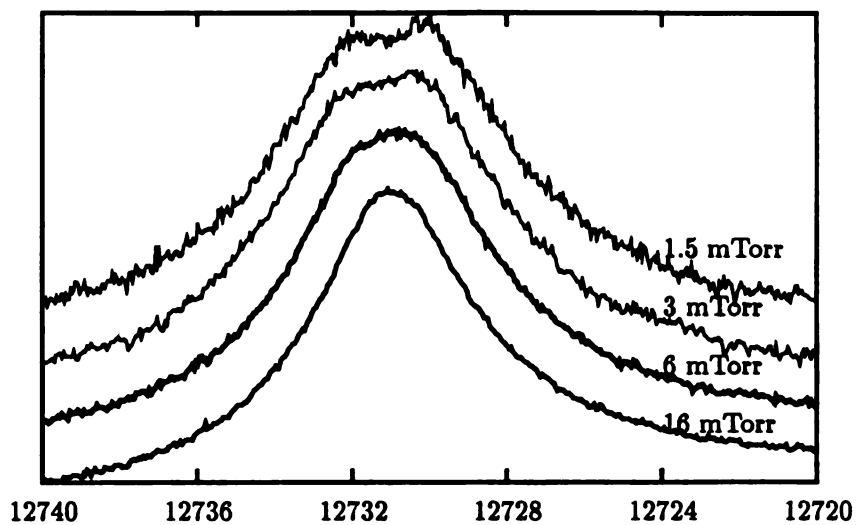


Figure 4.21: Four-level double resonance lineshape observed in the $Q_P(6,3)$ transition at various pressures.

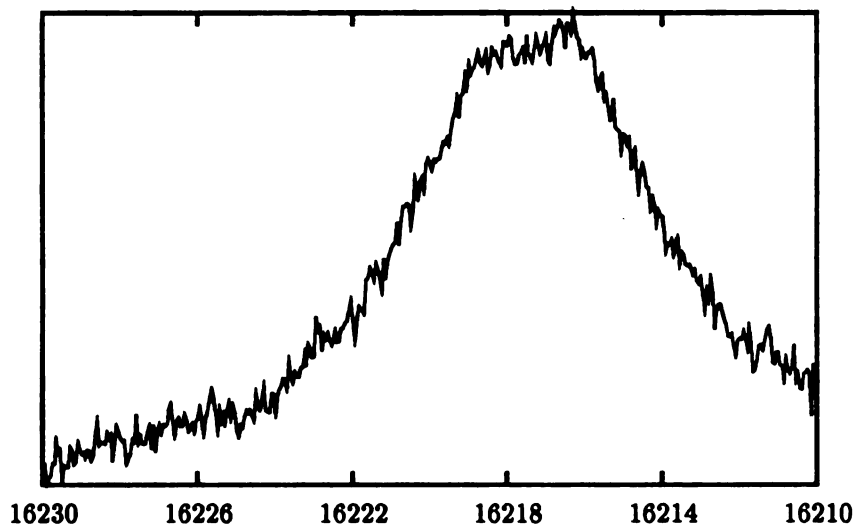


Figure 4.22: A dip observed from the $Q_P(4,3)$ transition. Sample pressure was 1.5 mTorr. The skewed direction and its width are similar to the dip observed from the $Q_P(6,3)$ transition.

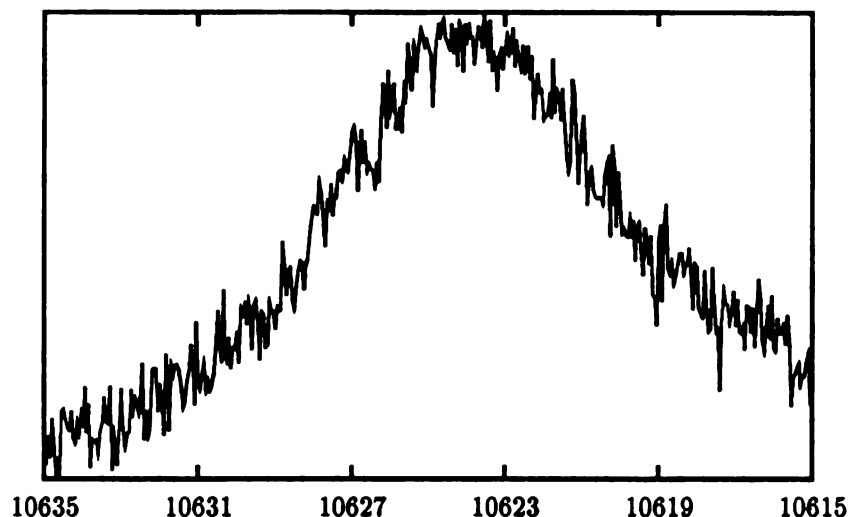


Figure 4.23: Four-level double resonance lineshape observed in the ${}^Q\text{P}(7,3)$ transition. Sample pressure was 1.5 mTorr. The peak is symmetric at the top and does not show any sign of dip.

while spreading out the coherence coupling, if the coherence transfer exists at all, the wider and reversed intensity of the splitting in the four-level dip agrees with our view of the collisional processes.

C. Simultaneous Measurements of Spikes for Co- and Counter-propagating Beam Geometry.

The sub-Doppler resolution of saturation absorption spectra has been widely used for accurate measurement of transition frequencies, as in the laser Stark Lamb dip and conventional absorption experiments. When transitions are heavily overlapped or when the molecules cannot be trapped in a Stark cell, alternative methods are required. Measurement of spikes and transferred spikes whose frequency can be accurately measured to better than 0.1 MHz is an ideal alternative, especially when the desired transitions are in a hot band overlapped with strong fundamental transitions. To obtain accurate transition frequencies, however, separate double resonance experiments under co- and counter-propagating conditions are necessary for each transition,

which requires more effort and is usually avoided in practice.

We have found that by simply reflecting the pump beam back into a sample cell, using an aperture with a tiny hole ($d \approx 1\text{mm}$) or a mirror with a small hole in it, separate spikes for co- and counter-propagating conditions can be recorded simultaneously by pumping and probing the ${}^{\text{Q}}\text{R}(4,3)$ transition (Figure 4.24). The offset between the pump laser and the center frequency of the transition can be calculated from the separation in frequency of two spikes without relying on the exact value of the laser frequency or on any applied field, such as used in Stark experiments. The offset of 24.2 ± 0.1 MHz measured in this experiment is more accurate than the previously known 25.8 MHz¹³⁹ measured in a laser Stark experiment largely because the lasers used in the present experiment were stabilized against a fluorescence Lamb dip. A number of different transitions were recorded in this way and all of them show consistent values after correcting for the Doppler effect. For example, the distance between the two spikes in Figure 4.25 observed in the ${}^{\text{Q}}\text{P}(5,3)$ transition in the $2\nu_3 \leftarrow \nu_3$ is 47.0 MHz, which becomes 48.5 MHz after Doppler correction to the ${}^{\text{Q}}\text{R}(4,3)$ frequency.

A similar measurement performed for the ${}^{\text{Q}}\text{Q}(12,9)$ transition in the $2\nu_3 \leftarrow \nu_3$ band of ${}^{12}\text{CH}_3\text{F}$ was used to determine that the offset between the ${}^{\text{Q}}\text{R}(11,9)$ transition and the 9P(20) line of a ${}^{12}\text{C}^{18}\text{O}_2$ laser is 24.8 ± 0.1 MHz. (Figure 4.26)

A second unusual feature is that the heights and widths of the resonances depend upon the propagation directions.^{62,140} A peak obtained for counterpropagating beams is narrower with a much higher maximum in the cascade three level system, whereas the opposite case was observed in a folded three level system.^{62,140} The asymmetric characteristics of the two peaks have been used in a ring resonator to obtain a unidirectional laser action as a result of the gain asymmetry¹⁴¹ or to measure the lifetime of the intermediate states.^{62,140}

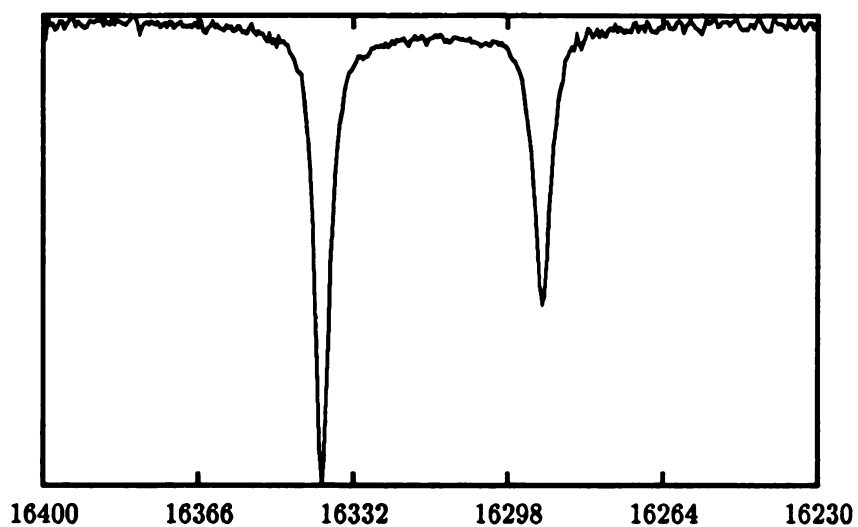


Figure 4.24: The $Q_R(4,3)$ transition in the ν_3 band of $^{13}\text{CH}_3\text{F}$ was probed by an IMSL operating on the 9R(26) line of a $^{13}\text{CO}_2$ laser while being pumped by another 9R(32) CO_2 laser. The spike under counter propagating condition is at -16339.0 MHz whereas that at -16290.5 MHz is for the co-propagating condition. The difference between the two spikes is 48.5 MHz which corresponds to 24.25 MHz offset.

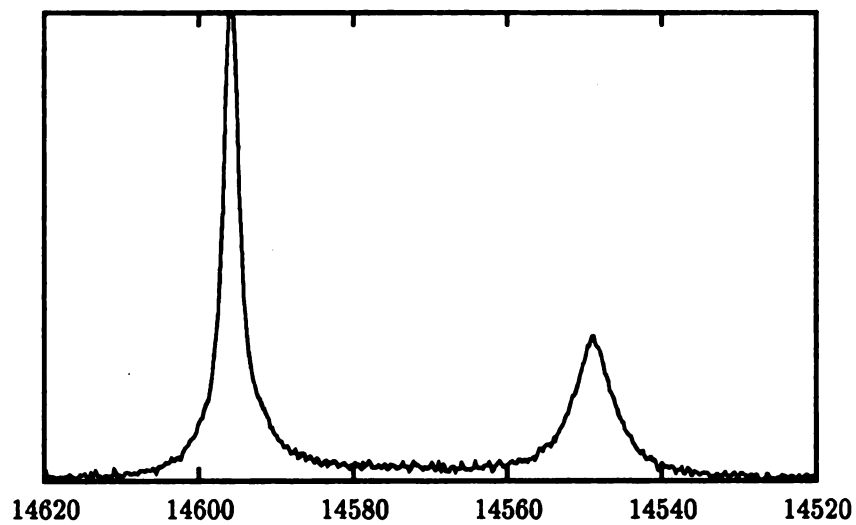


Figure 4.25: The ${}^Q\text{P}(5,3)$ transition in the $2\nu_3 \leftarrow \nu_3$ band of ${}^{13}\text{CH}_3\text{F}$ was probed by an IMSL operating on the $9\text{P}(16)$ line of a ${}^{13}\text{CO}_2$ laser while the ${}^Q\text{R}(4,3)$ transition in the ν_3 band was being pumped by another $9\text{R}(32)$ CO_2 laser. The center frequencies of the co- and counter-propagating spikes are 14596.0 MHz and 14547.0 MHz, respectively.

Table 4.1: List of transitions of the $2\nu_3 \leftarrow \nu_3$ band in $^{12}\text{CH}_3\text{F}$ and their frequencies plotted in this Chapter.

Transition	frequency	intensity	laser	line	$\Omega_l - \Omega$
$^{\circ}\text{Q}(9,9)$	30935348.53	0.008558	$^{12}\text{C}^{16}\text{O}_2$	9P(36)	12433.10
$^{\circ}\text{R}(10,9)$	31474569.75	0.001677	$^{12}\text{C}^{16}\text{O}_2$	9P(16)	-16867.65
$^{\circ}\text{Q}(12,9)$	30913528.61	0.004959	$^{12}\text{C}^{16}\text{O}_2$	9P(36)	-9386.82
$^{\circ}\text{R}(12,9)$	31558480.46	0.002586	$^{12}\text{C}^{16}\text{O}_2$	9P(14)	14451.58
$^{\circ}\text{Q}(13,9)$	30904942.47	0.004128	$^{12}\text{C}^{16}\text{O}_2$	9P(36)	-17972.96
$^{\circ}\text{R}(15,9)$	31679300.05	0.002964	$^{12}\text{C}^{16}\text{O}_2$	9P(8)	-17761.38
$^{\circ}\text{Q}(16,9)$	30875255.16	0.002337	$^{12}\text{C}^{16}\text{O}_2$	9P(38)	13357.65
$^{\circ}\text{R}(17,9)$	31756475.03	0.002793	$^{12}\text{C}^{16}\text{O}_2$	9P(6)	9991.23
$^{\circ}\text{Q}(18,9)$	30852197.20	0.001565	$^{12}\text{C}^{16}\text{O}_2$	9P(38)	-9700.32
$^{\circ}\text{Q}(21,9)$	30812737.91	0.000825	$^{12}\text{C}^{16}\text{O}_2$	9P(40)	12595.26

Table 4.2: List of transitions of the ν_3 band in $^{12}\text{CH}_3\text{F}$ and their frequencies plotted in this Chapter.

Transition	frequency	intensity	laser	line	$\Omega_l - \Omega$
$^{\circ}\text{Q}(11,9)$	31395255.59	0.983508	$^{12}\text{C}^{16}\text{O}_2$	9P(20)	11355.18
$^{\circ}\text{R}(11,9)$	31998588.06	0.365846	$^{12}\text{C}^{16}\text{O}_2$	9P(22)	-26.10
$^{\circ}\text{P}(12,9)$	30783654.50	0.331194	$^{12}\text{C}^{16}\text{O}_2$	9P(40)	-16488.15
$^{\circ}\text{R}(13,9)$	32081761.37	0.465245	$^{12}\text{C}^{16}\text{O}_2$	9R(8)	-9891.29
$^{\circ}\text{Q}(14,9)$	31368401.78	0.564118	$^{12}\text{C}^{16}\text{O}_2$	9P(20)	-15498.63
$^{\circ}\text{R}(14,9)$	32122297.33	0.484147	$^{12}\text{C}^{16}\text{O}_2$	9R(10)	-11969.56
$^{\circ}\text{R}(15,9)$	32162132.95	0.487108	$^{12}\text{C}^{16}\text{O}_2$	9R(12)	-13946.54
$^{\circ}\text{R}(16,9)$	32201268.41	0.477234	$^{12}\text{C}^{16}\text{O}_2$	9R(14)	-15822.86
$^{\circ}\text{R}(17,9)$	32239704.00	0.457373	$^{12}\text{C}^{16}\text{O}_2$	9R(16)	-17599.35
$^{\circ}\text{Q}(21,9)$	31282012.97	0.133864	$^{12}\text{C}^{16}\text{O}_2$	9P(24)	8765.82

Table 4.3: Velocity changes upon collision for ν_3 band transitions in $^{12}\text{CH}_3\text{F}$. The $^{\text{Q}}\text{R}(11,9)$ transition in the ν_3 band was pumped.

Probe ^a	Ratio ^b	$k\beta_1$ ^c	$(\Delta v_{rms})_1$ ^d	$k\beta_2$ ^e	$(\Delta v_{rms})_2$ ^f
P(12,9)	1.0	2.2	15	11	74
R(13,9)	1.4	2.8	19	12	81
Q(14,9)	1.3	2.7	18	12	79
R(14,9)	1.7	3.2	27	15	98
R(15,9)	2.4	3.7	24	16	106
R(16,9)	2.6	4.0	27	18	117
R(17,9)	2.8	4.8	32	20	131
Q(21,9)	3.7	7.5	51	23	154

^a Probe transition in the ν_3 band. $\Delta K = 0$ for all transitions.

^b Ratio of the area of the broad spike to that of the narrow spike.

^c Keilson-Storer β parameter in frequency units (MHz) for the narrow spike. $k =$ the magnitude of the wave vector for the probe transition.

^d Root-mean-square change in speed (m/s) for molecules that contribute to the narrow spike.

^e Keilson-Storer β parameter in frequency units (MHz) for the broad spike.

^f Root-mean-square change in speed (m/s) for molecules that contribute to the broad spike.

Table 4.4: Velocity changes upon collision for $2\nu_3 \leftarrow \nu_3$ band transitions in the CH_3F . The ${}^{\text{Q}}\text{R}(11,9)$ transition in the ν_3 band was pumped.

Probe ^a	ΔJ^b	Ratio ^c	$k\beta_1^d$	$(\Delta v_{rms})_1^e$	$k\beta_2^f$	$(\Delta v_{rms})_2^g$
Q(9,9)	-3	1.7	3.5	24	16	107
R(10,9)	-2	1.3	3.1	22	13	91
Q(13,9)	1	0.9	2.2	15	10	69
R(15,9)	3	1.4	3.0	20	14	92
Q(16,9)	4	1.8	3.3	22	15	101
R(17,9)	5	2.2	3.7	25	16	108
Q(18,9)	6	2.6	4.0	27	17	120
Q(21,9)	9	4.7	5.5	37	22	149

^a Probe transition in the $2\nu_3 \leftarrow \nu_3$ band. $\Delta K = 0$ for all transitions.

^b $\Delta J = J(\text{lower state of probe}) - J(\text{upper state of pump})$.

^c Ratio of the area of the broad spike to that of the narrow spike.

^d Keilson-Storer β parameter in frequency units (MHz) for the narrow spike. $k =$ the magnitude of the wave vector for the probe transition.

^e Root-mean-square change in speed (m/s) for molecules that contribute to the narrow spike.

^f Keilson-Storer β parameter in frequency units (MHz) for the broad spike.

^g Root-mean-square change in speed (m/s) for molecules that contribute to the broad spike.

Table 4.5: List of transitions and their frequencies (MHz) in $^{13}\text{CH}_3\text{F}$ plotted in this Chapter.

Transition	v_u	v_l	frequency	laser	line	$\Omega_l - \Omega$
$^{\text{Q}}\text{R}(4,3)$	1	0	31042692	$^{12}\text{C}^{16}\text{O}_2$	9P(32)	-25
$^{\text{Q}}\text{R}(4,3)$	1	0	31042692	$^{13}\text{C}^{16}\text{O}_2$	9R(26)	-16317
$^{\text{Q}}\text{P}(4,3)$	2	1	30144521	$^{13}\text{C}^{16}\text{O}_2$	9P(14)	-16198
$^{\text{Q}}\text{P}(5,0)$	2	1	30092702	$^{13}\text{C}^{16}\text{O}_2$	9P(16)	-14850
$^{\text{Q}}\text{P}(5,1)$	2	1	30092732	$^{13}\text{C}^{16}\text{O}_2$	9P(16)	-14820
$^{\text{Q}}\text{P}(5,2)$	2	1	30092823	$^{13}\text{C}^{16}\text{O}_2$	9P(16)	-14729
$^{\text{Q}}\text{P}(5,3)$	2	1	30092976	$^{13}\text{C}^{16}\text{O}_2$	9P(16)	-14576
$^{\text{Q}}\text{P}(5,4)$	2	1	30093194	$^{13}\text{C}^{16}\text{O}_2$	9P(16)	-14358
$^{\text{Q}}\text{P}(6,0)$	2	1	30040538	$^{13}\text{C}^{16}\text{O}_2$	9P(18)	-12990
$^{\text{Q}}\text{P}(6,1)$	2	1	30040868	$^{13}\text{C}^{16}\text{O}_2$	9P(18)	-12959
$^{\text{Q}}\text{P}(6,2)$	2	1	30040661	$^{13}\text{C}^{16}\text{O}_2$	9P(18)	-12867
$^{\text{Q}}\text{P}(6,3)$	2	1	30040816	$^{13}\text{C}^{16}\text{O}_2$	9P(18)	-12712
$^{\text{Q}}\text{P}(7,3)$	2	1	29988045	$^{13}\text{C}^{16}\text{O}_2$	9P(20)	-10605
$^{\text{Q}}\text{R}(10,3)$	2	1	30843128	$^{13}\text{C}^{16}\text{O}_2$	9R(14)	9116
$^{\text{Q}}\text{P}(22,3)$	2	1	29124206	$^{12}\text{C}^{16}\text{O}_2$	10R(14)	-13529
$^{\text{Q}}\text{P}(22,4)$	2	1	29124424	$^{12}\text{C}^{16}\text{O}_2$	10R(14)	-13311

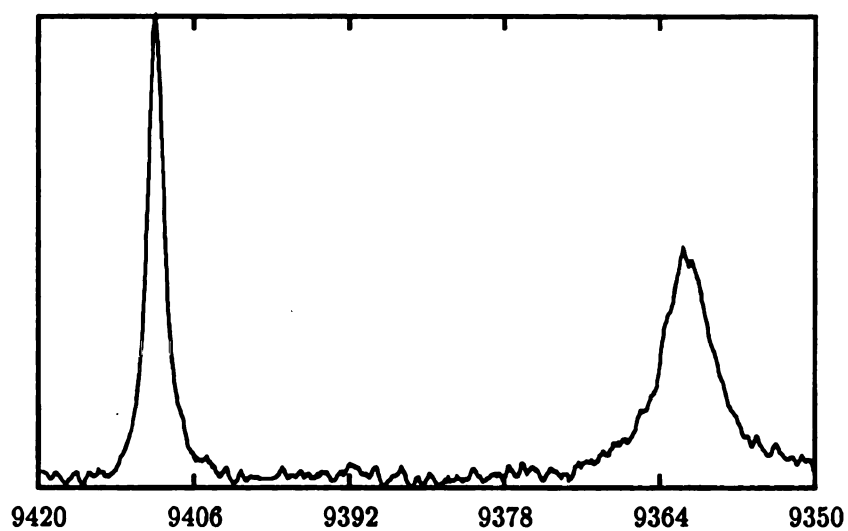


Figure 4.26: The ${}^{\text{Q}}\text{Q}(12,9)$ transition in the $2\nu_3 \leftarrow \nu_3$ band of ${}^{12}\text{CH}_3\text{F}$ was probed by an IMSL operating on the 9P(36) line of a ${}^{12}\text{CO}_2$ laser while the ${}^{\text{Q}}\text{R}(11,9)$ transition in the ν_3 band was pumped by another 9P(22) C^{18}O_2 laser. The spike under counter propagating conditions is at -9409.6 MHz whereas it is at -9361.7 MHz for co-propagating condition. The difference between the two spikes is 47.9 MHz which corresponds to 24.8 MHz offset in the ${}^{\text{Q}}\text{R}(11,9)$ after correcting for the Doppler effect.

IV. Polarization Spectroscopy

Figures 4.27 and 4.28 compare double resonance signals recorded with a π (i.e., linearly polarized) probe while a σ^+ (i.e., left circularly polarized) laser was used for pumping. The top traces in Figures 4.27 and 4.28, recorded with a π analyzing polarizer in front of the detector, are almost identical with normal intensity-modulated double resonance signals for the case in which the π probe beam is observed without the analyzing polarizer while the π pump beam is being mechanically modulated. When the analyzing polarizer is set to the σ^\pm angle, the phase of the sharp spike observed on top of the broad Gaussian is reversed as shown in the middle trace of Figures 4.27 and 4.28. The top trace was subtracted from the middle trace to remove the Gaussian (shown in the bottom trace), or these could be added to each other to remove the spike. This simple demonstration shows that the spike part and the Gaussian part have different polarization characteristics, which can be used to separate them.

The σ^+ pump beam creates a population increase in the upper level (intensity modulation) as well as inducing an optical anisotropy in the excited level. The polarization directions of the two signals created are different. The signal from the optical anisotropy has an elliptical polarization tilted away from the probe polarization, as explained in the experimental section, whereas the intensity modulated signal has the same linear polarization as the probe beam. If a polarizer is used in front of the detector to block the original probe polarization, the weak laser-induced anisotropy can be measured. This experimental technique is called *polarization labeling*.

The molecules directly excited by a σ^+ pump are probed as a spike, whereas the laser-induced optical anisotropy shifts the phase of the σ^+ component of the linearly polarized probe, tilting its polarization axis. This is shown as a negative sign when σ^\pm is selected or as positive when π is chosen. The Gaussian, as discussed in the previous section, comes from those molecules that underwent vibrational energy transfer collisions with the directly pumped molecules. Therefore molecules originating from that process will be isotropic unless the polarization of a directly pumped molecule transfers during the collision. Therefore the phase of the Gaussian does not depend

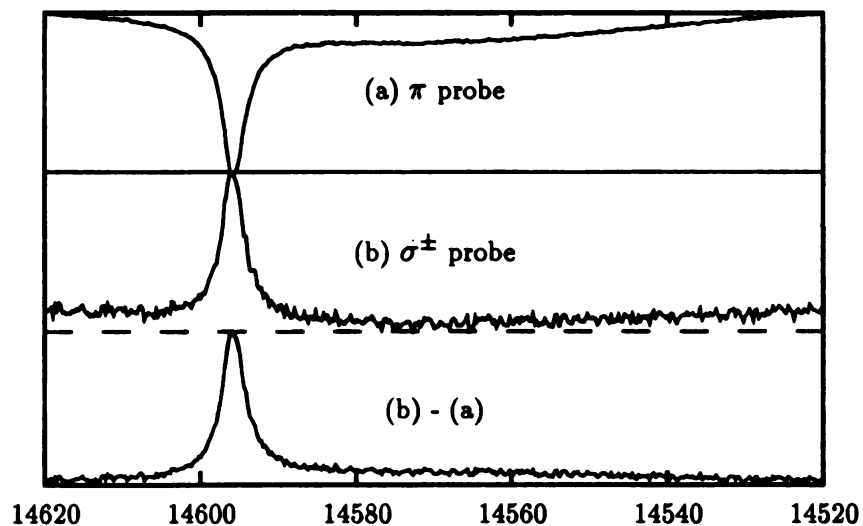


Figure 4.27: ${}^Q\text{P}(5,3)$ in $2\nu_3 \leftarrow \nu_3$ of ${}^{13}\text{CH}_3\text{F}$ at 6 mTorr. The ${}^Q\text{R}(4,3)$ in the ν_3 fundamental band was pumped by a σ^+ 9R(32) CO_2 laser. Description of the experimental conditions is given in the text.

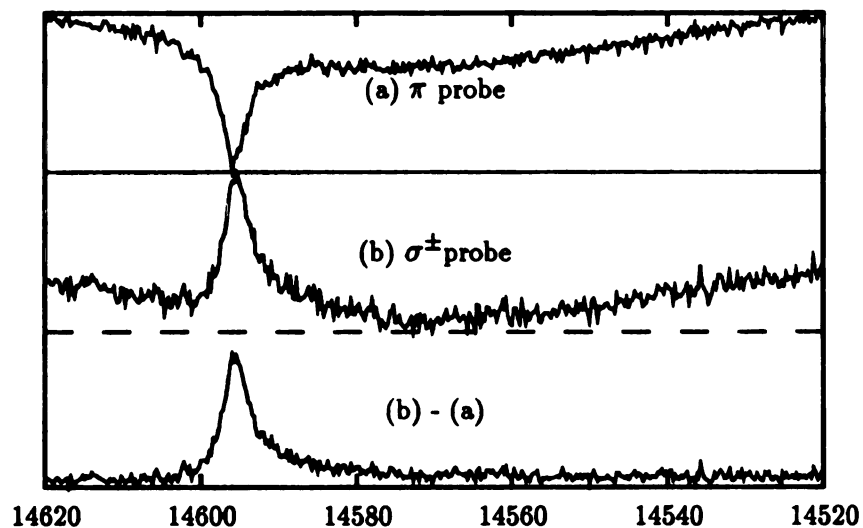


Figure 4.28: ${}^Q\text{P}(5,3)$ in $2\nu_3 \leftarrow \nu_3$ of ${}^{13}\text{CH}_3\text{F}$ at 60 mTorr. The ${}^Q\text{R}(4,3)$ in the ν_3 fundamental band was pumped by a σ^+ 9R(32) CO_2 laser. The experimental arrangement is described in the text.

upon the polarization axis selected and its phase does not change in the recorded spectrum. This laser-induced optical anisotropy was not observed when plane polarized light (σ^\pm or π) was used for pumping for obvious reasons.

The observation just described prompted polarization modulation experiments in which the polarization states of the pump beam are modulated between σ^\pm and π (alignment modulation) or between σ^+ and σ^- (orientation modulation).

V. Polarization Modulation

A. Alignment Modulation (σ^\pm/π)

Alignment modulated double resonance signals show only a sharp peak located at the usual spike frequency as shown in Figures 4.29 and 4.30. When the polarization of the pump beam is modulated such that the intensities of the pump beams polarized σ^\pm and π are the same, the total population difference ($\Delta N = N_{lower} - N_{upper}$) created by the two pump beams are same, even though, as described in the theory section, the alignments of the molecules are different. The recorded signal, therefore, represents the absorption from those molecules that change their alignment as the polarization of the pump beam changes. This may be interpreted as a form of photo-selected linear dichroism in which a differential absorption ($\Delta\alpha = \alpha_\pi - \alpha_{\sigma^\pm}$) of two beams with orthogonal planes of polarization is measured.

The observation of our alignment modulated signal in four-level double resonance shows (Figure 4.30) that the J changing inelastic collisions do not completely destroy the alignment. As explained above, the Gaussian component of the lineshape originates from ground level molecules that underwent collisional vibrational energy transfer and which therefore do not experience the polarization of the pump beam directly. They should therefore not contribute to the alignment modulated double resonance. Therefore the residual Gaussian background in Figure 4.30 is most likely the result of the intensity difference between the σ^\pm and the π pump beams due to the experimental difficulty in obtaining the same intensity after reflection by mirrors.

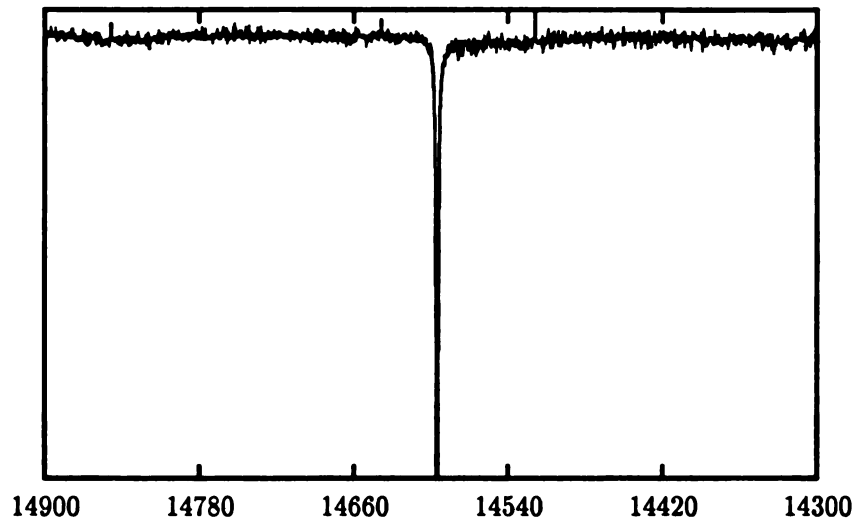


Figure 4.29: The frequency of the σ^\pm polarized probe laser was scanned from the ${}^Q\text{P}(5,0)$ to the ${}^Q\text{P}(5,4)$ transitions in the $2\nu_3 \leftarrow \nu_3$ band of ${}^{13}\text{CH}_3\text{F}$ while the polarization of the pump laser coincident on the ${}^Q\text{R}(4,3)$ transition in the ν_3 band was switched between σ^\pm and π . There is no sign of signal other than at the frequency where the ordinary spike is observed, which implies that only the spike changes its orientation to follow the change in polarization of the pump beam.

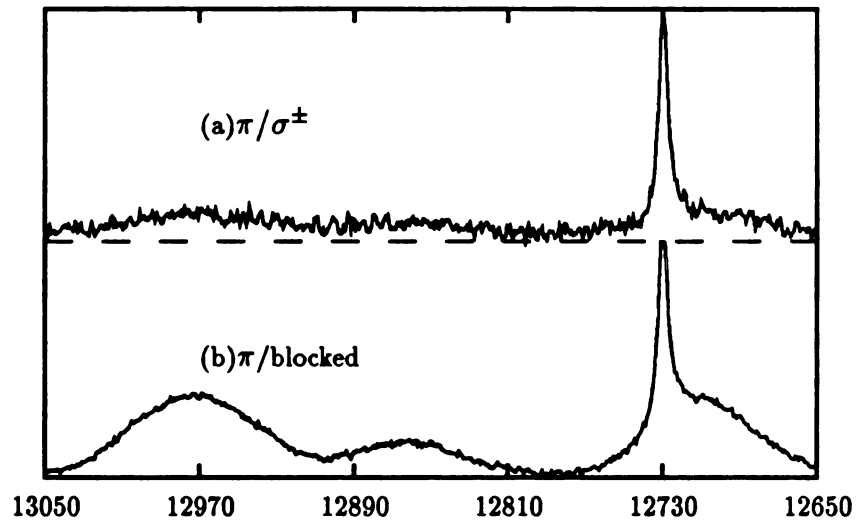


Figure 4.30: The frequency of the probe laser was scanned from the ${}^{\text{Q}}\text{P}(6,0)$ to ${}^{\text{Q}}\text{P}(6,3)$ transitions while (a) the polarization of the pump laser was switched between σ^{\pm} and π and (b) the pump beam was intensity modulated by blocking its σ^{\pm} component. Signals from the Gaussian part are apparent in (b) intensity modulation, but not in (a) alignment modulation.

B. Orientation Modulation (σ^-/σ^+)

Generally circular dichroism (CD) is measured by recording the differential absorption of left and right circularly polarized radiation ($\Delta\alpha = \alpha^+ - \alpha^-$) in two-step experiments or by polarization modulation in which the polarization of the radiation is modulated between σ^+ and σ^- . This technique can also be applied to the measurement of photo-selected vibrational circular dichroism (VCD), in which an intense σ^+ light is used to select the molecules and the polarization of a weak probe beam is modulated between σ^+ and σ^- . Even those molecules that do not show ordinary VCD exhibit this kind of photo-selected VCD, since the circularly-polarized strong pump beam induces circular dichroism by creating oriented molecules. For experimental reasons, the photo-selected VCD was measured by probing a σ^+ beam while modulating the pump beam between σ^+ and σ^- , as shown in Figure 3.6.

The three level double resonance signal of the ${}^Q\text{P}(5,3)$ transition in the $2\nu_3 \leftarrow \nu_3$ band of ${}^{13}\text{CH}_3\text{F}$ was recorded with different configurations while the ${}^Q\text{R}(4,3)$ transition in the ν_3 band was pumped by a 9R(32) CO_2 laser. The pump laser was modulated by switching the polarization between σ^+ and σ^- . In Figure 4.31-(a,b) a circularly polarized probe beam interacts with the molecules and then hits the detector. When a wire-grid polarizer was used in front of the sample cell to create a plane polarized probe beam, the signal almost disappeared, providing firm proof for circular dichroism (Figure 4.31-(b)). If the polarizer was after the sample cell (in front of the detector), a spectrum with half the intensity of the VCD signal was observed (Figure 4.31-(c)). This is expected since circularly polarized light can be considered to be a sum of two plane polarized beams and only half of the probe beam intensity is hitting the detector. The only difference in the experimental conditions between (b) and (c) in Figure 4.31 is whether the wire-grid polarizer is located (b) before or (c) after the sample cell. Therefore, the probe beam is plane polarized in (b) when it interacts with molecules whereas in (c) it is circularly polarized.

The experimental test just described ensures that the VCD in Figure 4.31-(a) is not the result of experimental artifacts, such as intensity difference between σ^+ and σ^- or an elliptical polarization. The usual picture of circular polarization being the

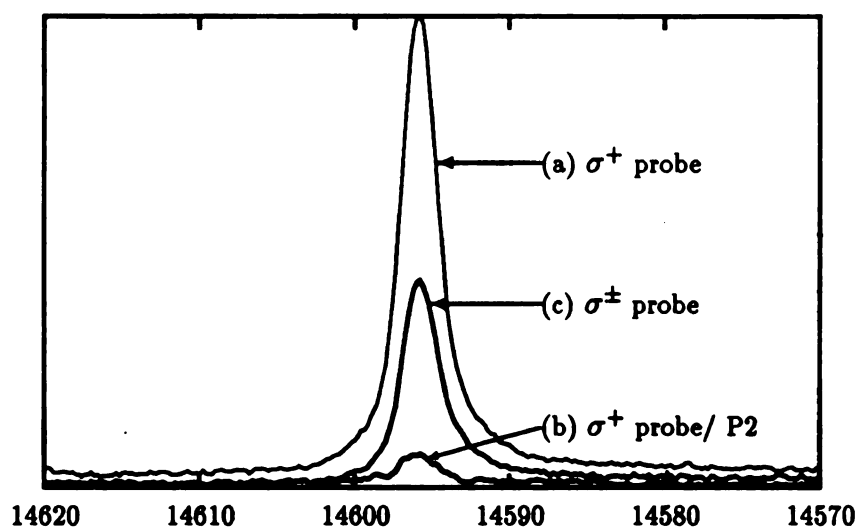


Figure 4.31: Photo-selected VCD observed from ${}^Q\text{P}(5,3)$ in the $2\nu_3 \leftarrow \nu_3$ band of ${}^{13}\text{CH}_3\text{F}$ while the ${}^Q\text{R}(4,3)$ in the ν_3 band was pumped. (a) A σ^+ probe was used while the polarization of the pump beam was modulated between σ^+ and σ^- . (b) A wire-grid polarizer was put in front of the sample cell to create a plane polarized probe beam. Other conditions were exactly same as in (a). (c) The polarizer used in (b) was moved to in front of the detector. The probe beam is circularly polarized while interacting with molecules but plane polarized at the detector.

sum of two orthogonal plane polarized beams is assured from the intensity ratio of (a) and (c) in Figure 4.31. Here we will derive recorded intensities for these three experimental conditions using the Jones calculus explained in Chapter 2. First a $\sigma^\pm(J_{\sigma^\pm})$ polarization is converted into σ^+ by a quarter wave plate ($M_{\lambda/4}$) and used for the probe while the polarization of the pump is modulated between σ^+ and σ^- . Using the Jones calculus the recorded intensity is

$$\begin{aligned} I &= |M_{or}M_{\lambda/4}J_{\sigma^\pm}|^2 - |M_{or'}M_{\lambda/4}J_{\sigma^\pm}|^2 \\ &= p_r^2 - p_l^2 . \end{aligned}$$

This recorded signal represents laser induced vibrational circular dichroism. If a polarizer ($M_{\theta=90}$) is put before the sample cell

$$\begin{aligned} I &= |M_{or}M_{90}M_{\lambda/4}J_{\sigma^\pm}|^2 - |M_{or'}M_{90}M_{\lambda/4}J_{\sigma^\pm}|^2 \\ &= 0 , \end{aligned}$$

which agrees with our experimental observation. When the same polarizer is moved in front of the detector, the recorded signal is

$$\begin{aligned} I &= |M_{90}M_{or}M_{\lambda/4}J_{\sigma^\pm}|^2 - |M_{90}M_{or'}M_{\lambda/4}J_{\sigma^\pm}|^2 \\ &= (p_r^2 - p_l^2)/2 . \end{aligned}$$

It is again a circular dichroism measurement, but its intensity is halved.

C. Laser-induced Birefringence

In the series of previous experiments, two linear polarizers can be used with a relative 45° angle, one before the sample cell, the other after the sample cell. Then the detector sees

$$\begin{aligned} I &= |M_{\theta=45}M_{or}M_{\theta=0}M_{\lambda/4}J_{\sigma^\pm}|^2 - |M_{\theta=45}M_{or'}M_{\theta=0}M_{\lambda/4}J_{\sigma^\pm}|^2 \\ &= p_r p_l \sin(2\delta)/2 . \end{aligned}$$

This is a pure circular birefringence induced by the optical pumping. This result is confirmed from the approximate method discussed in Chapter 2. In Eq. 2.47 the

resulting intensity under similar experimental conditions was

$$\begin{aligned} I(\omega) &= I_o[4 \sin^2 \theta - 4 \sin \theta \cos \theta (\Delta k)L + (\Delta k^2 + \Delta \alpha^2)L^2 \cos^2 \theta] \\ &= I_o[4 \sin^2 \theta + 2 \sin(2\theta)\Delta kL + (\Delta k^2 + \Delta \alpha^2)L^2 \cos^2 \theta] \end{aligned}$$

where θ is the angle of the linear polarizer referred to the x axis. The effect of polarization modulation is to change the sign of Δk . Therefore the difference in signal is

$$\begin{aligned} I(\omega) &= 2I_o[\sin(2\theta)\Delta k - \sin(2\theta)(-\Delta k)]L \\ &= 4I_o \sin(2\theta)\Delta kL . \end{aligned}$$

Since $\theta = 45^\circ$ in this experiment, the observed signal is $4I_o\Delta kL$. With this method a dispersion lineshape was observed by probing the ${}^Q\text{P}(5,3)$ transition in the $2\nu_3 \leftarrow \nu_3$ band while pumping the ${}^Q\text{R}(4,3)$ in the ν_3 band; the spectrum is shown in Figure 4.32.

Similar spectra were observed for the ${}^Q\text{P}(6,3)$ transition in the $2\nu_3 \leftarrow \nu_3$ band, which does not have direct connection to the level perturbed by the pump. As shown in Figures 4.33-4.35 a photo-selected VCD, a dispersion shape, and an intensity modulated signal all show the same tendency when observed by the three-level double resonance. Upon comparison of the three spectra, it is clear that the Gaussian signal observed in the intensity modulation is removed in the polarization modulation completely.

Another interesting observation was made when the pressure of the sample was lowered to below 5 mTorr until a splitting was observed in the intensity modulated signal. A number of spectra were recorded under three different conditions with a linearly polarized probe. The first of these was recorded with so-called intensity modulation in which the pump was mechanically chopped. It is shown at Figure 4.36. It shows a splitting at the center of the spike. Then the electro-optic switch system described previously was placed in the pump beam path in addition to the mechanical chopper and the same experiment was repeated with the mechanical chopper. The result is shown at Figure 4.37. It seems that the presence of the CdTe crystal spoils the laser beam profile and results in no splitting. The experiment was then repeated once more without the mechanical chopper. Instead, the polarization of the pump

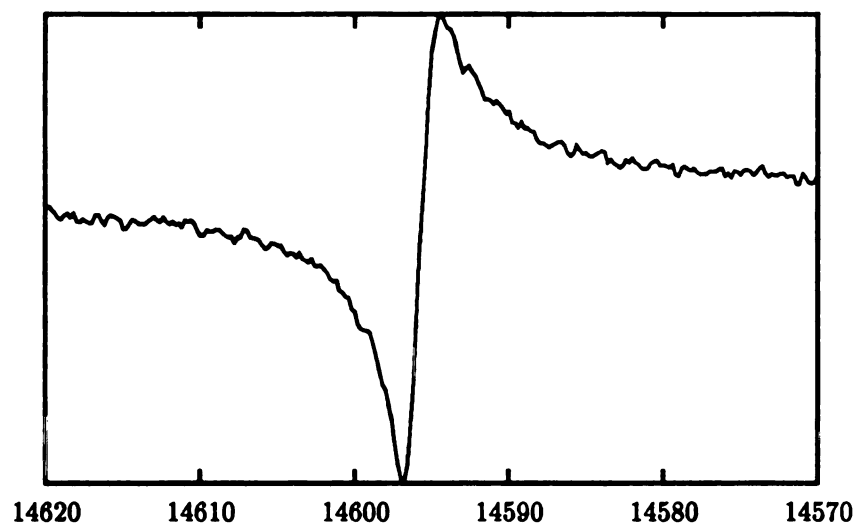


Figure 4.32: A dispersion signal observed in the ${}^Q\text{P}(5,3)$ transition in the $2\nu_3 \leftarrow \nu_3$ band of ${}^{13}\text{CH}_3\text{F}$ while the ${}^Q\text{R}(4,3)$ transition in the ν_3 band was pumped. Two polarizers were used for the probe beam (one to generate a plane polarized probe beam before the sample cell, the other after sample cell set to 45° relative to the first polarizer) while the polarization of the pump beam was modulated between σ^+ and σ^- .

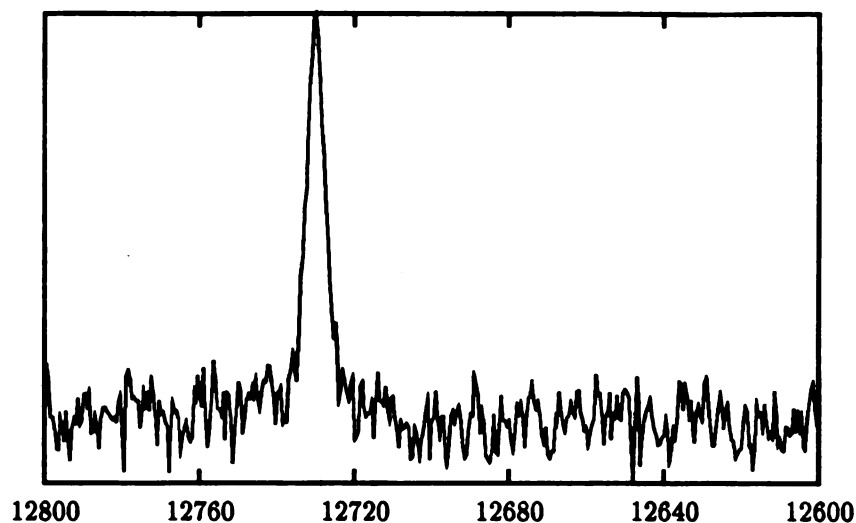


Figure 4.33: Photo-selected VCD observed in the ${}^Q\text{P}(6,3)$ transition in the $2\nu_3 \leftarrow \nu_3$ band while the ${}^Q\text{R}(4,3)$ transition in the ν_3 band was pumped. A σ^+ probe was used while the polarization of the pump beam was modulated between σ^+ and σ^- .

beam was modulated between σ^+ and σ^- by the electro-optic switch system. The result of this experiment is shown in Figure C. It shows a sign of a dip at the center of the dispersion signal. Upon comparing Figures 4.37 and C it is clear that the orientation modulated signal is more sensitive than the intensity modulated signal for observing the splitting. In fact, this can be expected considering that in the intensity modulation the signal is from any population changes that result from collisions, whereas in orientation modulation the signal is from only the molecules that do not change their orientation. In other words, the oriented molecules that underwent no or a few soft collisions are favorably probed compared to intensity modulation, where the history of the molecules does not matter as long as they stay in the same velocity group. All of these observed lineshapes agree at least qualitatively with calculations from our three-level double resonance theory.¹²

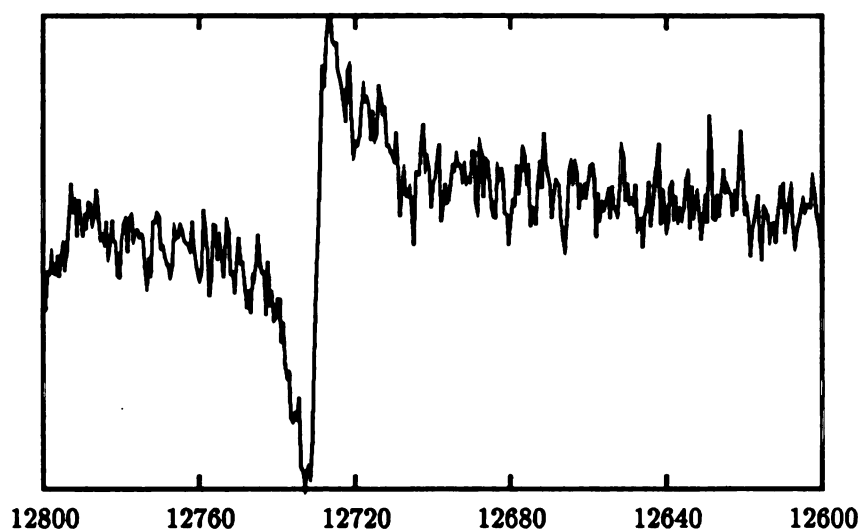


Figure 4.34: A dispersion signal observed in the ${}^{\text{Q}}\text{P}(6,3)$ transition in the $2\nu_3 \leftarrow \nu_3$ band of ${}^{13}\text{CH}_3\text{F}$ while the ${}^{\text{Q}}\text{R}(4,3)$ transition in the ν_3 band was pumped. Two polarizers were used for the probe beam (one to generate a plane polarized probe beam before the sample cell, the other after the sample cell set to 45° relative to the first polarizer) while the polarization of the pump beam was modulated between σ^+ and σ^- .

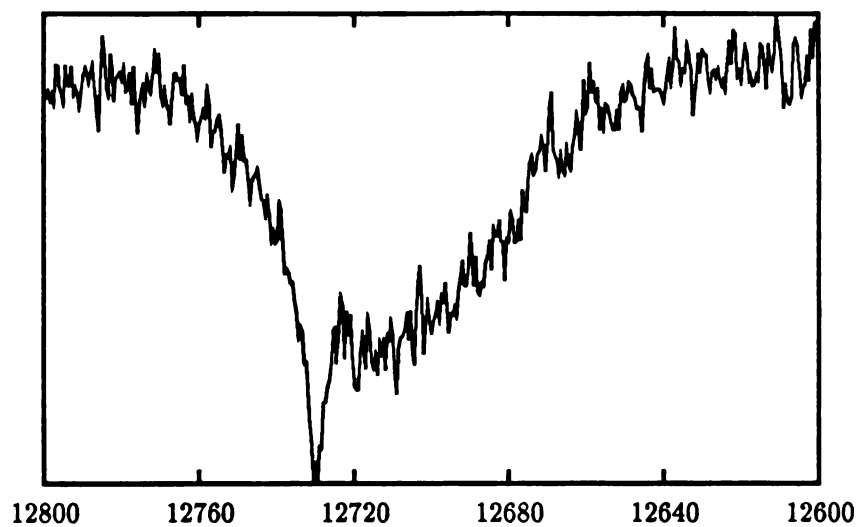


Figure 4.35: Intensity modulated double resonance signal observed in the ${}^Q\text{P}(6,3)$ transition with the same conditions as in the previous figure. A σ^+ probe was used while the power of the π pump beam was modulated with a mechanical chopper.

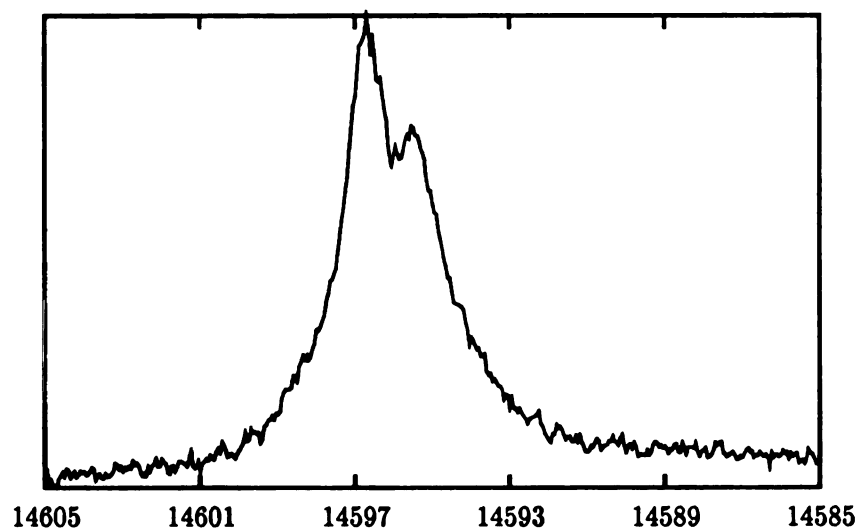


Figure 4.36: Intensity modulated spectrum of the ${}^Q\text{P}(5,3)$ transition in the $2\nu_3 \leftarrow \nu_3$ band while the ${}^Q\text{R}(4,3)$ transition in the ν_3 band was pumped.

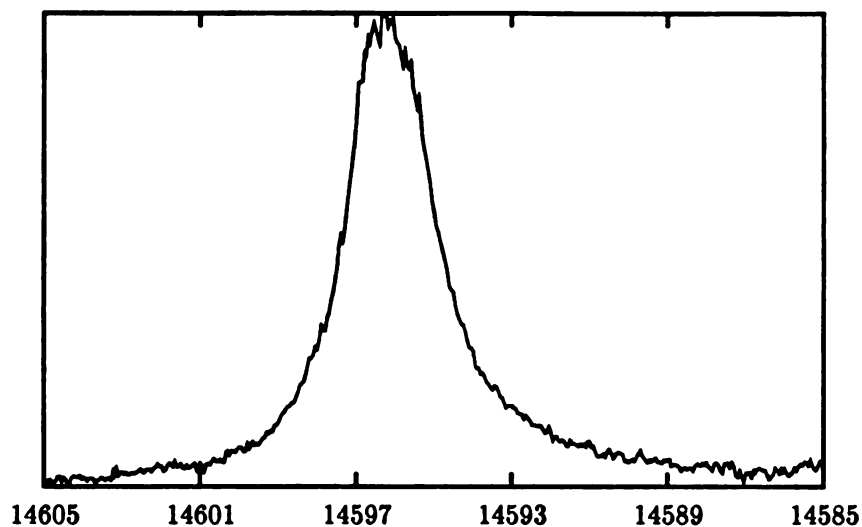


Figure 4.37: Intensity modulated spectrum of the ${}^Q\text{P}(5,3)$ transition in the $2\nu_3 \leftarrow \nu_3$ band while the ${}^Q\text{R}(4,3)$ transition in the ν_3 band was pumped. A π probe was used with an analysing polarizer ($\theta = 45$) in front of the detector.

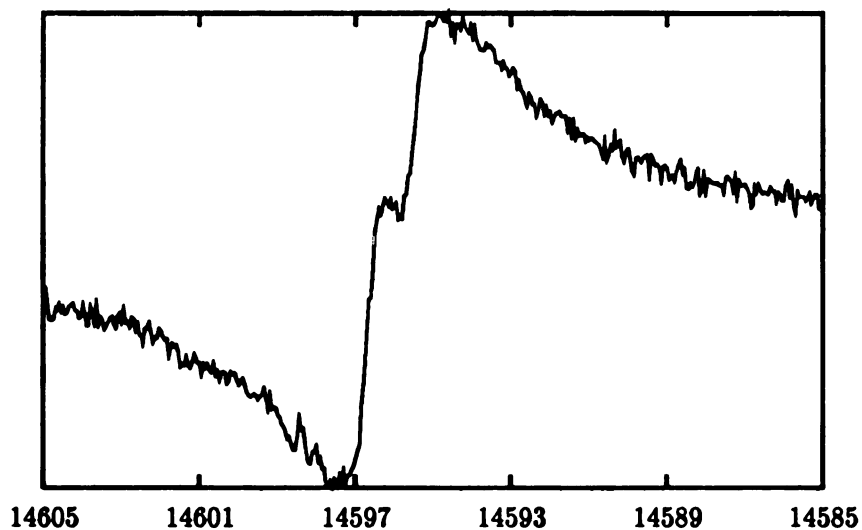


Figure 4.38: Orientation modulated spectrum of the ${}^Q\text{P}(5,3)$ transition in the $2\nu_3 \leftarrow \nu_3$ band while the ${}^Q\text{R}(4,3)$ transition in the ν_3 band was pumped. A π probe was used with an analysing polarizer ($\theta = 45$) in front of the detector.

VI. Polarization Labeling

The assignment of observed transitions can be assisted by polarization labeling experiments based on the phase and the intensity of the signals as explained in the theory. Although intensity modulated signals (*modulated-population spectroscopy*⁸³) allow a distinction between fundamental band and hot band transitions, the polarization labeling experiment provides information about whether the transition is in the $P(\Delta J = -1)$, $Q(\Delta J = 0)$, or $R(\Delta J = +1)$ branch.

In practice, however, measuring the birefringence is better than the normal polarization labeling experiments for number of reasons.

1. The birefringence measurement results in better signal/noise ratio (S/N) because the probe beam sees a constant perturbation by the pump in the birefringence measurement, whereas, in polarization labeling the probe beam experiences a sudden change in pump power in addition to the laser-induced optical anisotropy. Even though the sudden change experienced by the probe gives only a DC signal, it affects the entire detecting system and results in a poorer S/N ratio compared with the birefringence measurement.
2. It is somewhat easier to determine the center frequency of the dispersion lineshape obtained in the birefringence measurement than the center frequency of the absorption lineshape determined in the polarization labeling experiment.

The signs of the polarization modulated dispersion lineshapes show a clear distinction among P , Q , and R branches, as in polarization labeling spectroscopy. Three different transitions are shown in Figures 4.39-b, 4.40-b, and 4.41. Measurement of many other transitions showed that the phase of the dispersion shape changes from positive to negative in P -branch transitions, from negative to positive in R -branch, and no observable signal was recorded in Q -branch transitions, which agrees with the results for polarization labeling spectra. By combining the two double resonance signals (intensity modulation and polarization modulation), observed transitions can be assigned unambiguously to P , Q , or R branches and to fundamental or hot band transitions. The results are summarized in Table 4.6.

Table 4.6: Summary of relative signs observed in the population- and orientation-modulated double resonance signals. P, Q, R : Branch of the transition. $+, -,$ and 0 are for positive, negative, and no observable signal, respectively.

ν_{upper}	ν_{lower}	Branch	Population	Orientation
1	0	P	-	- ← +
1	0	Q	-	0
1	0	R	-	+ ← -
2	1	P	+	+ ← -
2	1	Q	+	0
2	1	R	+	- ← +

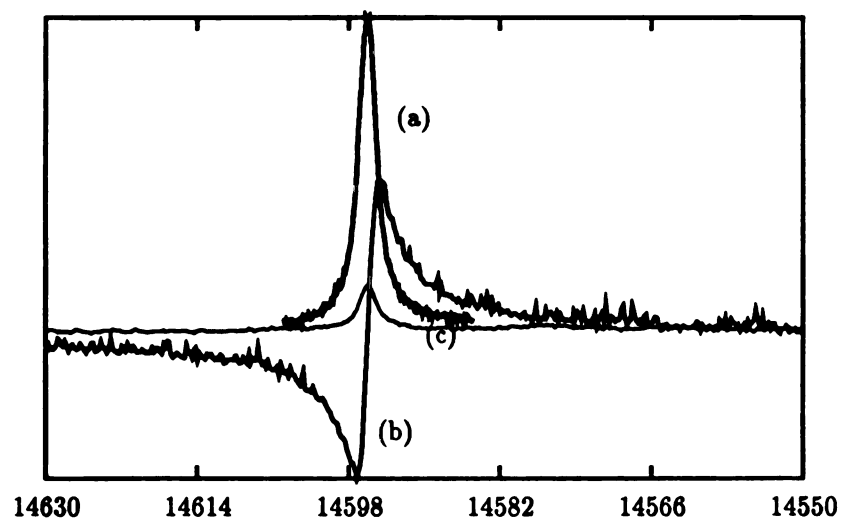


Figure 4.39: The $(\nu, J, K) = (2, 4, 3) \leftarrow (1, 5, 3)$ observed in double resonance: (a) intensity modulated signal; (b) polarization modulated signal; (c) signal recorded after the first demodulation during polarization modulation.

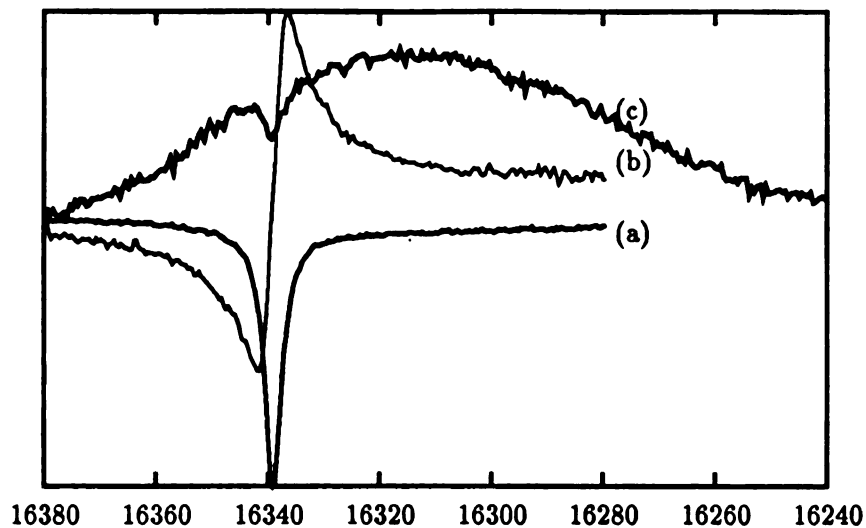


Figure 4.40: The $(v, J, K) = (1, 5, 3) \leftarrow (0, 4, 3)$ observed in double resonance: (a) intensity modulated signal; (b) polarization modulated signal; (c) signal recorded after the first demodulation during polarization modulation.

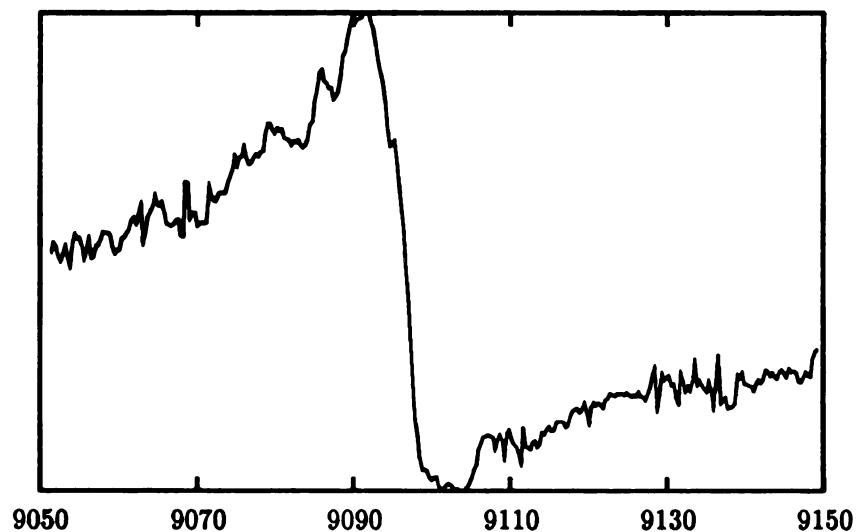


Figure 4.41: The $(v, J, K) = (2, 11, 3) \leftarrow (1, 10, 3)$ observed in four-level double resonance under conditions of polarization modulation. The sign changes from positive to negative.

A remarkable result is seen in Figure 4.41. Even after the many collisions that must occur in order to be observed from the $J = 10$ level and the substantial change in angular momentum that is required, the directly-pumped molecules still remember the orientation induced by the pump laser.

VII. Backward and Forward Spikes: Revisited

As demonstrated earlier in this chapter, center frequencies of transitions and their offsets from the laser frequencies can be measured accurately by measuring the frequencies of two spikes occurring under co- and counter-propagating conditions (c.f. Figures 4.24, 4.25, and 4.26). As shown in Figure 4.42, the same experiment with polarization modulation gives two dispersion shaped peaks which allow easy estimation of the center frequencies of the spikes without fitting. The dispersion signal can also be used to lock the laser frequency at the center of the dispersion shape, thereby eliminating the intentional frequency modulation that is necessary to lock the laser to the usual fluorescence Lamb dip.

Since the intensity of the pump laser does not change in the polarization modulation experiment, the signal recorded after the first demodulation shows the double resonance effect under constant pumping condition. This effect of laser pumping can be simultaneously recorded while the orientation changes are being recorded from the second lock-in amplifier. In Figures 4.43 and 4.44 the lower trace (signal recorded after the first demodulation) shows the pumping effect on the absorption with a very good S/N.

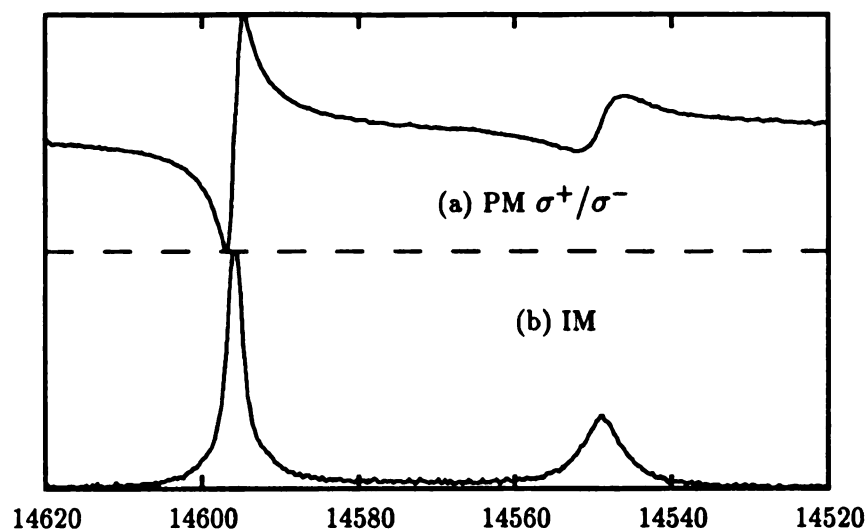


Figure 4.42: The $(v, J, K) = (2, 4, 3) \leftarrow (1, 5, 3)$ transition of $^{13}\text{CH}_3\text{F}$ was probed by an IMSL while $(v, J, K) = (1, 5, 3) \leftarrow (0, 4, 3)$ was pumped (a) by polarization modulation (PM) between σ^+ and σ^- (b) by intensity modulation (IM). In both cases the pump laser was reflected back into sample cell to record both of the spikes occurring under co- and counter-configuration.

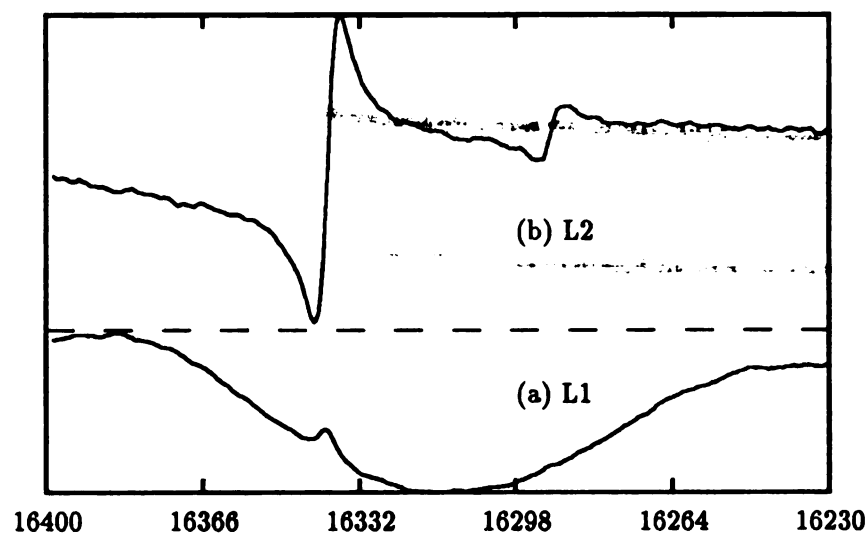


Figure 4.43: The $(v, J, K) = (1, 5, 3) \leftarrow (0, 4, 3)$ double resonance signal recorded (a) after the first demodulation from L1 (b) after double demodulation from L2.

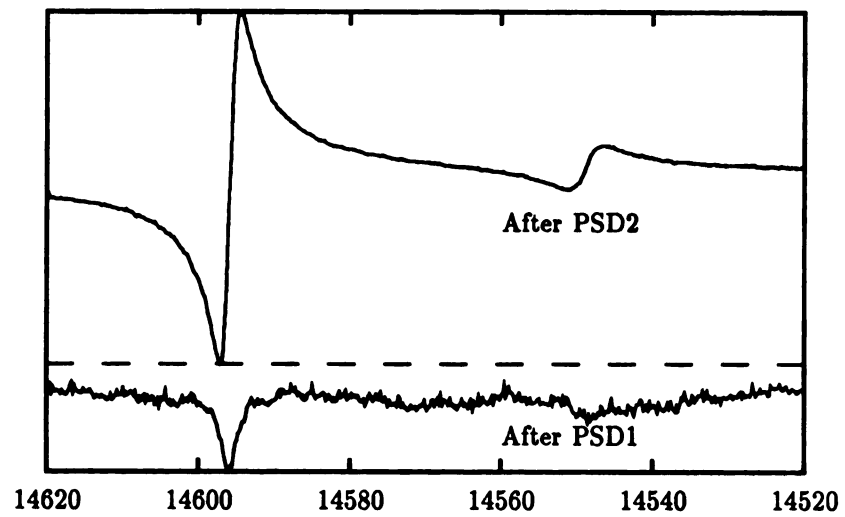


Figure 4.44: The $(v, J, K) = (2, 4, 3) \leftarrow (1, 5, 3)$ double resonance signal.

VIII. Time Resolved Spectroscopy

A. Measurement of Relaxation rates

Since the transferred spikes originate from those directly pumped molecules that underwent J changing collisions with large impact parameters while the Gaussian part is presumed to result from $V - V$ energy transfer, I expected the transferred spikes to have the fastest time response to the pumping. Everitt and De Lucia¹¹³ found from their measurements of time-resolved infrared-millimeter wave double resonance spectra, that the directly pumped spike has the fastest time response. In our work, we found that the time response of the transferred spikes becomes slower as the absolute value of ΔJ ($= |J_{pumped} - J_{probed}|$) becomes larger as shown in Figure 4.45. Of the transitions studied, the directly pumped ${}^Q\text{P}(5,3)$ spike had the steepest slope, whereas the ${}^Q\text{P}(7,3)$ spike had the slowest rise time. For $\Delta J > 0$, there is also a delay after the pump laser is turned on, which increases with $|\Delta J|$ suggesting an increasing effect of multiple collisions.

Unlike time-resolved experiments involving rotational transitions where population changes are the result of transitions into and out of both levels in the same vibrational mode, time-resolved signals from vibrational spectra in a stacked double-resonance configuration may show population changes of only the lower probed level, since population changes of the upper probed level may be negligible. Therefore, by measuring several levels adjacent to the pumped level, it should be possible to find out whether multiple $\Delta J = \pm 1$ collisions or single $\Delta J = n$, ($n = 2, 3, 4\dots$) collisions are the main collision paths that change rotational energy populations. Also, by measuring the spikes and the Gaussian separately, it should be possible to deduce directly the relaxation rates of the three collision processes from recorded signals.

From the $\Delta J = 1$ collision rate reported by Henry and De Lucia,¹¹³ the calculated rate of growth of the population of the $(J, K) = (4, 3)$ or $(6, 3)$ levels in the $2\nu_3 \leftarrow \nu_3$ band at 20 mTorr is 1.32 MHz. Since the recorded signal is the convolved result of the system time response (350 kHz band width) with a population change of the probed level that is the result of dozens of collision channels, direct fitting of the

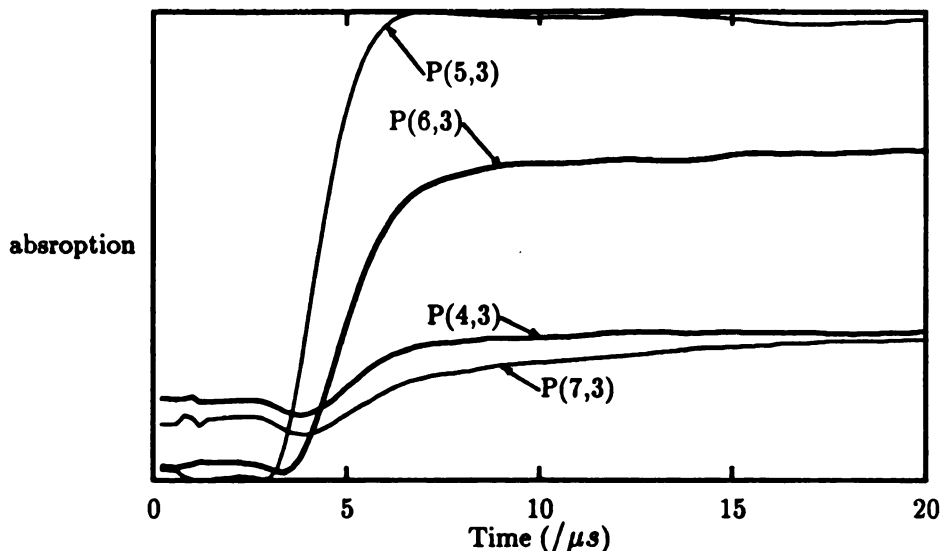


Figure 4.45: Time resolved spectra of the (transferred) spike of ${}^Q\text{P}(4,3)$, ${}^Q\text{P}(5,3)$, ${}^Q\text{P}(6,3)$, and of ${}^Q\text{P}(7,3)$ transitions in the $2\nu_3 \leftarrow \nu_3$ band. The ${}^Q\text{R}(4,3)$ transition in the ν_3 fundamental band was pumped on at $3 \mu\text{sec}$. The transient digitizer was pre-triggered to record starting values.

relaxation rates from the decay curve was not possible. Instead, as reported by Henry and De Lucia,¹¹³ a simulation including all of the important collision channels is required to extract relaxation rates from the observed decay curves. Unfortunately, the signal/noise ratio (S/N) of our system is only marginal, so that it was difficult to record more than five transitions, which were not enough for the simulation. The S/N can be improved by increasing the sample pressure, but at higher pressure the rate also increases above the limit of the LECROY 6810 and puts the probe signal at a level at which it is no longer a linear function of the absorption coefficient. This would require a difficult calibration to locate the baselines. Even though many transitions with good S/N were recorded with an 8-pass 1-m White type cell, these experiments showed the same non-linearity problem. For these reasons, efforts to obtain the relaxation rates were not attempted any further and only a qualitative description of the observed results will be given.

As expected, at higher pressure the rates of the collision processes increase, which leads to faster time response as shown in Figure 4.46. Although I thought that the

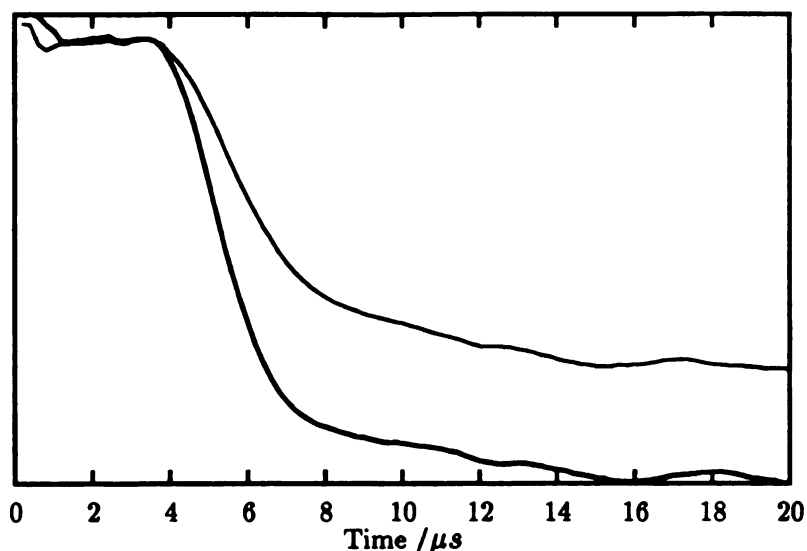


Figure 4.46: Time resolved signal of the ${}^{\text{Q}}\text{P}(6,3)$ transition at (a) 20 mTorr (b) 40 mTorr

pump-on response and the *pump-off* response would be the same, since the rates do not change, a faster *pump-on* increase than *pump-off* decrease was observed by recording at least one complete pump cycle. This is shown in Figure 4.47.

For previously described reasons, the measurement of relaxation rates was not attempted any further. However, it was confirmed that there exist at least three different relaxation paths with different rates as predicted from the lineshape study of four-level double resonance. The results shown in Figure 4.48 represent the $\Delta J = n, \Delta K = 0$ process, the $\Delta K = 3n$ process, and the vibrational energy transfer, respectively. It is summarized with approximate rates;

1. sharp spike, $\sim \mu\text{sec}$, observed only from $K = 3$ levels, $\Delta J = \pm n, \Delta K = 0$
 $\text{CH}_3\text{F}(v, J, K) + \text{CH}_3\text{F} \rightarrow \text{CH}_3\text{F}(v, J \pm n, K) + \text{CH}_3\text{F}$
2. broad spike, $\sim \text{msec}$, observed from $K = 3n, n = \text{integer}$ levels, $\Delta K = 3n$
 $\text{CH}_3\text{F}(v, J, K) + \text{CH}_3\text{F} \rightarrow \text{CH}_3\text{F}(v, J', K \pm 3n) + \text{CH}_3\text{F}$
3. Gaussian, $\sim \text{msec}$, observed from all of the levels, vibrational swapping
 $\text{CH}_3\text{F}(1, J, K) + \text{CH}_3\text{F}(0, J', K') \rightarrow \text{CH}_3\text{F}(0, J'', K'') + \text{CH}_3\text{F}(1, J''', K''')$

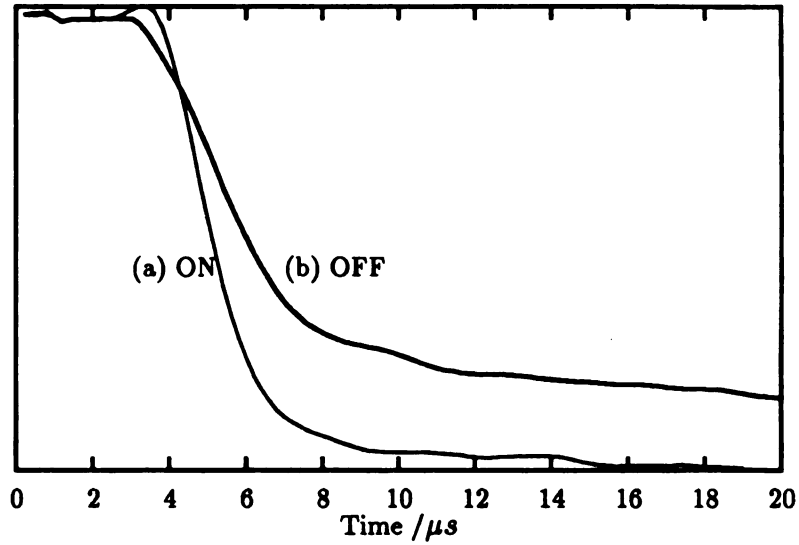


Figure 4.47: Time resolved signal of the ${}^{\text{Q}}\text{P}(6,3)$ transition. (a) when the pump laser is turned on; (b) when the pump laser is turned off. The measured ON signal is subtracted from a constant to have common starting level. The on-stage time response is faster and more intense than the off-stage.

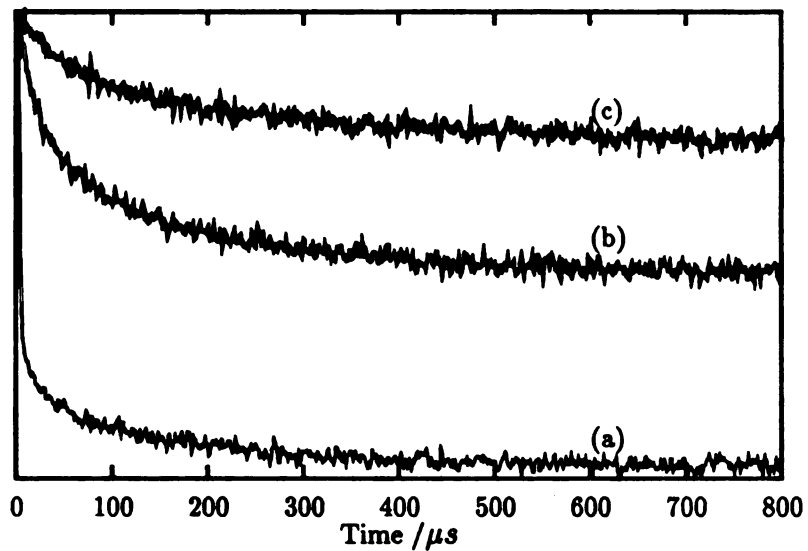


Figure 4.48: Time resolved signals of (a) sharp spike (b) Gaussian + broad spike observed in ${}^{\text{Q}}\text{P}(6,3)$ transition (c) Gaussian observed in ${}^{\text{Q}}\text{P}(6,2)$ transitions.

B. Phase Separation of Ortho- and Para-transitions

Even though relaxation rates of the three collision processes were not obtainable, the time resolved data contain useful time domain information. Since $\Delta k \neq 3n$ collision-induced transitions require a collision-induced change of the spin state, pumping a $K = 3$ transition should lead to faster population changes in other $K = 3n$ transitions than in $K \neq 3n$ transitions. It should be possible to observe this difference by varying the phase of the lock-in amplifier that processes the steady state double resonance signal.

The spectrum shown in Figure 4.49 includes the steady-state four-level double resonance signals of the $J = 22, K = 1..9$ transitions in the $2\nu_3 \leftarrow \nu_3$ band of $^{13}\text{CH}_3\text{F}$ recorded by using the system shown in Figure 3.9 while the $^{\text{Q}}\text{R}(4,3)$ transition in the ν_3 band was pumped. At $J = 22$, the $\Delta J = \pm 1$ rotational relaxation contribution is almost certainly smaller than (at most comparable to) the other two processes. The only contributions to the double resonance signals of the para transitions ($K \neq 3n$), are from vibrational energy transfer processes whereas both vibrational energy transfer and $\Delta K = 3n$ processes contribute to the signals of the ortho transitions ($K = 3n$). This is clearly seen when the intensities of the recorded spectrum are compared with the intensities of a calculated spectrum, as in Figure 4.49. Therefore it is reasonable to assume that the ortho- and para-transitions have slightly different time responses.

Unfortunately, the time resolved signals of $K = 3$ and $K = 4$ shown in Figure 4.50 had so similar time response that when they were normalized they looked almost the same. Nevertheless, the phase difference of the two peaks, if any, could be easily detected by simulating the output of a lock-in amplifier at different phases by using

$$S(\phi) = \int_0^1 D(t) \sin(\omega t + \phi) dt, \quad (4.1)$$

where ω is the modulation frequency, ϕ is the phase, $S(\phi)$ is the calculated signal at phase ϕ , and $D(t)$ is the detected signal at time t . The experimental time domain signals and the resulting simulated phase variation are plotted in Figures 4.50 and 4.51.

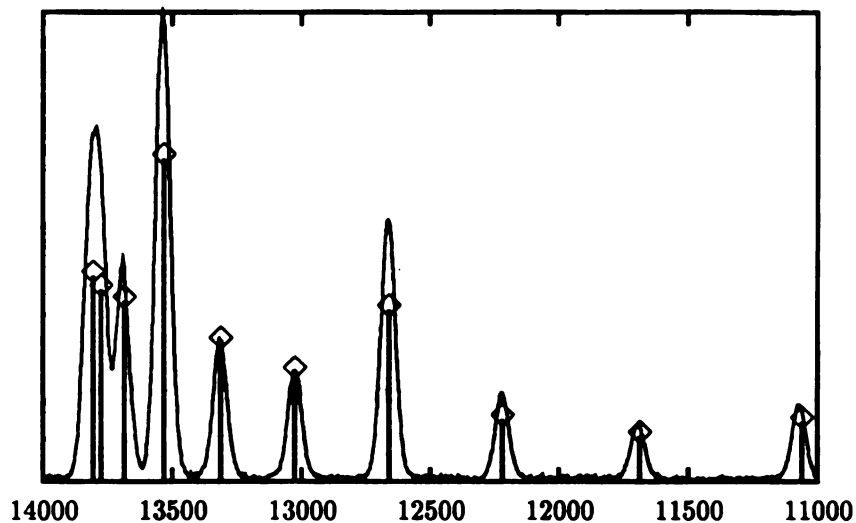


Figure 4.49: Double-resonance spectrum of ${}^Q\text{P}(22,K)$ transitions in the $2\nu_3 \leftarrow \nu_3$ band of ${}^{13}\text{CH}_3\text{F}$ upon which calculated frequencies and intensities are superposed. It is clear that the $K = 3n$ transitions are stronger than calculated compared with $K \neq 3n$ transitions. The pump transition is ${}^Q\text{R}(4,3)$ in the ν_3 band and the pump source is a $9\text{P}(32)$ ${}^{12}\text{C}^{16}\text{O}_2$ laser. The probe source is the negative sideband on the $10\text{R}(14)$ ${}^{12}\text{C}^{16}\text{O}_2$ laser; the horizontal axis is the microwave frequency offset.

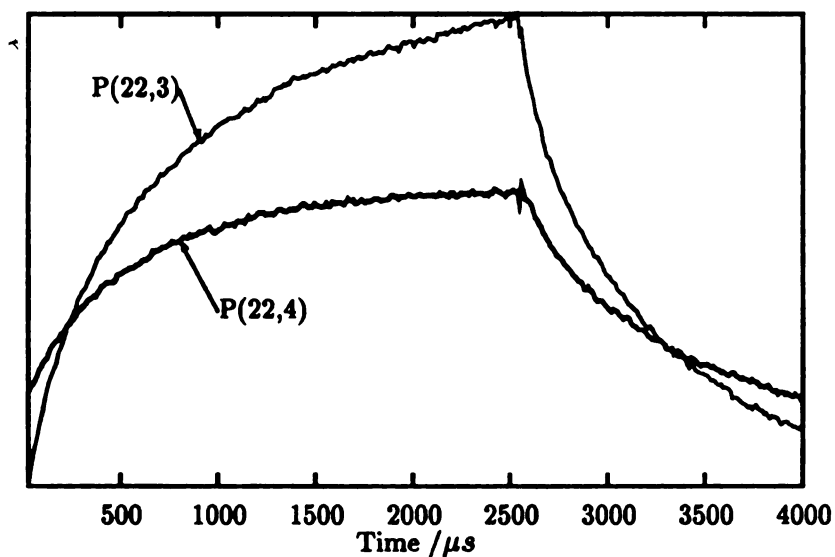


Figure 4.50: Time resolved spectra of $K=3$ and $K=4$ transitions in Figure 4.51. The $K=3$ transition is stronger and faster than the $K=4$ transition.

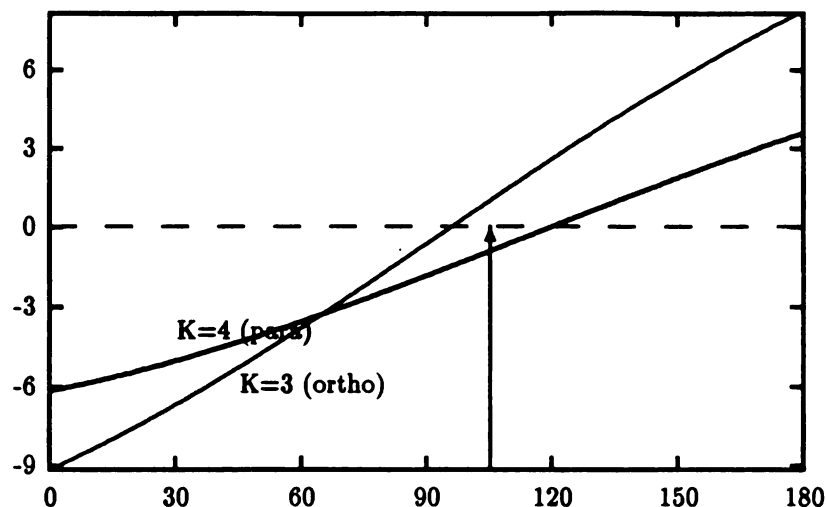


Figure 4.51: Calculated output vs. phase setting of the lock-in amplifier for the peak double resonance signal for the ${}^Q\text{P}(22,3)$ (thin line) and ${}^Q\text{P}(22,4)$ (thick line) transitions shown in Figure 4.49.

From Figure 4.51, it is obvious that the two signals have different phases; otherwise, the two signals would have changed their signs at the same phase. At the phase near 110° , where an arrow is drawn, the absorption of the $K = 3$ (ortho-transition) occurs in the positive phase while the absorption of the $K = 4$ (para-transition) occurs in the negative phase. In fact, by using this calculated phase in an experiment it was possible to clearly distinguish ortho-transitions ($K = 3n$) from para-transitions ($K \neq 3n$) as shown in Figure 4.52.

The spectrum shows that the phase of $K = 3n$ transitions are all positive whereas the phase of $K \neq 3n$ transitions are all negative, as expected from the simulation. Apparently the $\Delta k = 3n$ selection rule persists for many J states away from the originally-pumped level ($J = 5$). The spectrum also shows that the $\Delta K = 3n$ peaks are skewed to lower frequency relative to their center frequencies. This supports the assumption that the $k = 3n$ populations result primarily from a sequence of rotational transitions that brings the molecules from the originally-pumped level to the lower level of the probe without complete thermalization of velocity.

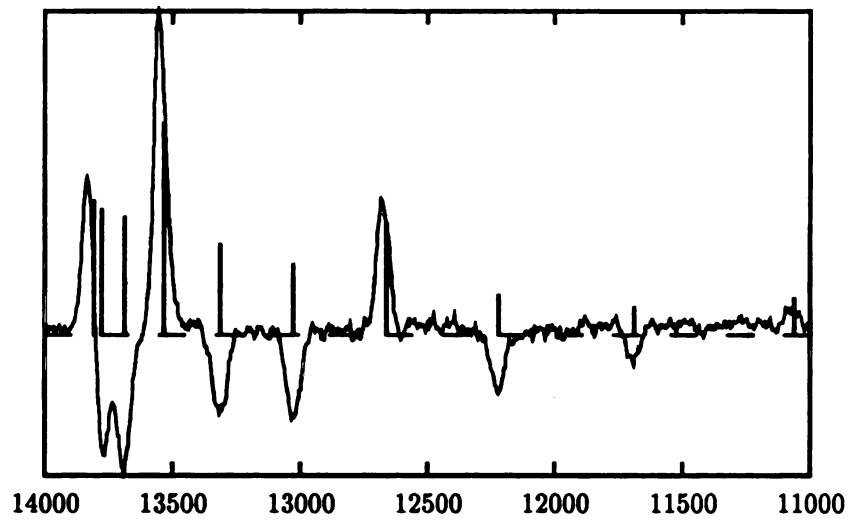


Figure 4.52: Double-resonance spectrum of ${}^9\text{P}(22, K)$ ($K=0..9$, left to right) transitions in the $2\nu_3 \leftarrow \nu_3$ band of ${}^{13}\text{CH}_3\text{F}$ observed with the 110° phase. (The calculated spectrum is drawn with vertical bars for comparison.) The pump transition is ${}^9\text{R}(4,3)$ in the ν_3 band and the pump source is a $9\text{P}(32)$ ${}^{12}\text{C}^{16}\text{O}_2$ laser. The probe source is the negative sideband on the $10\text{R}(14)$ ${}^{12}\text{C}^{16}\text{O}_2$ laser; the horizontal axis is the microwave frequency offset.

The results of the time-dependent spectra confirm the assumptions of the simulation of the time dependence of infrared-millimeter wave double-resonance spectra proposed by Everitt and De Lucia.¹¹³ They found it necessary to use a larger rate constant for $\Delta k = 3n$ transitions than for $\Delta k \neq 3n$ transitions. The lineshapes of our infrared-infrared double-resonance spectra confirm their hypothesis that the $\Delta k = 3n$ transitions are collisionally-induced rotational transitions whereas the $\Delta k \neq 3n$ transitions result from a V-V energy transfer. The spectra in Fig. 4.52 also demonstrate that the $\Delta k = 3n$ excitation produced by radiation pumping persists for many J values away from the originally pumped level. Whether this requires many collisions or only a few is not certain. Based on the time delay in the time resolved observation of the transferred spikes ($J = 5, 6,$ and 7) and the phase shift observed in the $P(22, K)$ transitions, it is clear that many successive collisions of $\Delta J = 1$ and of $\Delta k = 3n, \Delta J = n$ exist. Harradine *et al.*⁵² interpret their data in terms of successive $\Delta J = \pm 1$ collisions, whereas the simulation of Everitt and De Lucia¹¹³ includes a separate rate constant for $\Delta k = 0, \Delta J = n$ collisions which would dominate at the $\Delta J = 17$ required for Figure 4.52.

IX. Summary

1. The electro-optic switching system was shown to be useful for time resolved infrared-infrared double resonance spectroscopy. With a faster digitizer and a more stable laser system this experiment should give unambiguous answers to many of the current questions about collisional energy transfer.
2. The three collisional processes predicted from the lineshape of four-level infrared-infrared double resonance signals were time resolved and show different characteristics in the time domain. Time gated frequency domain spectra should be very useful for extraction of relevant information from their line shape.
3. Transitions in ortho and para CH_3F were distinguished by the difference in phase, which implies successive collisions in the $\Delta k = 3n$ process. More detailed and extensive experiments are required to confirm this result.

4. The laser guiding optics used in the polarization modulation experiments can be used to time resolve the alignment relaxation rates and orientation relaxation rates without modifications.

Chapter 5

Conclusion and Future Work

I have demonstrated a number of sub-Doppler or Doppler-free double resonance spectroscopic techniques by tailoring the polarization states of lasers used in double resonance experiments. They are useful in studying collisional processes of molecules as well as in identifying observed transitions. Through the use of an electro-optic polarization modulation device and a partially transmitting mirror, various of experiments were demonstrated that can measure linear dichroism, circular dichroism, and circular birefringence of a laser-induced optical anisotropy. Especially, the measurement of circular birefringence is shown to be very useful and easy to implement in experiments. A similar technique can be used to observe a laser-induced dichroism and birefringence, in which a circularly polarized probe beam is recorded, while the polarization state of the pump beam is modulated between π and σ^\pm . If the probe beam is recorded after passing a polarizer set 0° relative to the YZ plane, a pure linear dichroism can be measured, whereas a linear birefringence can be recorded by rotating the polarizer 45° .

By taking advantage of the Doppler line profile, it was possible to extract velocity changes of molecules as a result of collisions from the lineshapes of the transferred spike. It should be possible to relate the observed dispersion lineshape to the orientation of the molecules, thereby obtaining changes not only of velocity but also of orientation as result of collisions.

Table 5.1: Summary of identified relaxation paths, lineshapes, relaxation times, and their effects on velocity, alignment, and orientation.

Process	Lineshape	Rate	Velocity	Orientation
$\Delta J = 1, \Delta K = 0$	Sharp spike	μs	Yes	Yes
$\Delta K = 3n, n$ integer	Broad spike	ms	Yes	No
V-V energy transfer	Gaussian	ms	No	No

The electro-optic switching system should be very useful for time-resolved infrared-infrared double resonance spectroscopy. The three collisional processes predicted from the lineshape of four-level infrared-infrared double resonance signals were time resolved and show different characteristics in the time domain. Time-gated frequency domain spectra should be very useful for extraction of relevant information from their line shape. If the laser guiding optics are modified, as in the polarization spectroscopy section, the system can also be used to time resolve laser-induced optical anisotropy, in which a photoreaction can be initiated with a laser and its progress can be probed by monitoring the polarization signals either of the reactants or of the products. Since the polarization information allows a three-dimensional view of molecules, this would be extremely powerful in studies where spatial information is required such as in enzymes or in catalysts.

Table 5.1 summarizes the characteristics of the different collisional processes observed.

The sub-Doppler resolution and spatial resolution of the saturation experiments should be a valuable tool in remote sensing since a spatially fixed probe can be recorded while the pump beam selects different regions as in Figure 5.1.

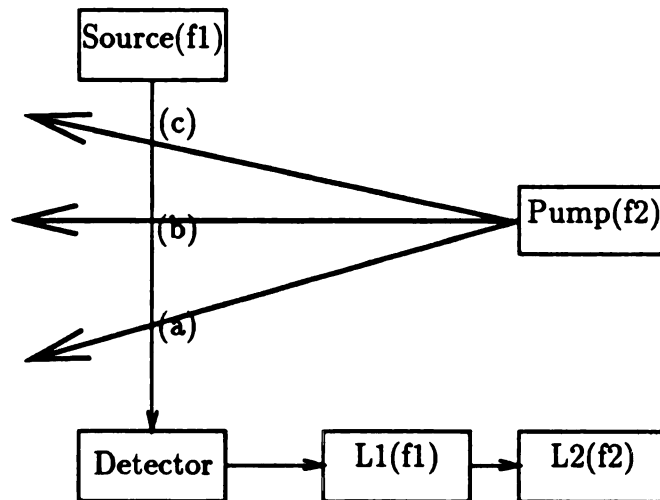


Figure 5.1: Application of double resonance in remote sensing. By changing the incident angle of the pump beam, only a selected portion (a, b, or c) of the probe beam path is affected and its signal can be recovered after the double demodulation.

Chapter 6

APPENDIX

APPENDIX

The purpose of this Appendix is to develop equations that facilitate the direct comparison of the intensities of three-level and four-level double resonances taken with the same apparatus under conditions of constant pump and probe powers. The basic equation for this purpose is the relation between the spectroscopic absorption coefficient and the imaginary part of the density matrix element that connects the two states most closely involved with the absorption by the probe beam. We use this equation in the form

$$\alpha = \left(\frac{16\pi^2 N}{cE^\circ} \right) \nu \sum_m \mu_{ab}(m) \int_{-\infty}^{\infty} d''_{ba}(m, \nu_y) d\nu_y \quad (\text{A1})$$

in which ν is the frequency and E° is the electric field amplitude of the probe beam and $\mu_{ab}(m)$ is the transition dipole moment connecting states a and b of energies E_a and E_b , respectively, for which $\nu \sim (E_b - E_a)/h$. The density matrix factor d''_{ba} is defined by

$$\rho_{ba} = (d'_{ba} + id''_{ba}) e^{-2\pi i \nu t} \quad (\text{A2})$$

where ρ_{ba} is the element of the density matrix connecting states a and b . Also in Eq. A1, c is the speed of light in the sample; N is defined to be the number of molecules per cm^3 in the lower level of the pump transition; and α is assumed to be expressible as a sum of absorption coefficients for transitions involving individual m states, where $m\hbar$ is the component of the angular momentum of an individual molecule in the direction of the space-fixed Z axis.

For three-level double resonance, we assume a strong pump beam traveling in the Y direction and polarized in the YZ plane, so that $\Delta m = 0$ selection rules apply for the pump transition. The probe beam is assumed to be polarized in the YX plane for which the selection rules are $\Delta m = \pm 1$. A further assumption, confirmed by calculation, is that the probe is weak enough that

$$\int_{-\infty}^{\infty} d''_{ba}(m, \nu_y) d\nu_y = x_{ab}(m) \bar{d}''_{ba}(m) \quad (\text{A3})$$

where $x_{ab}(m) = \mu_{ab}(m)E^\circ/h$ and $\bar{d}_{ba}''(m)$ is independent of x_{ab} . Consequently, although each pump transition is associated with two double resonances,

$$\begin{array}{c} m \xrightarrow{\text{pump}} m \xrightarrow{\text{probe}} m-1 \\ \text{and} \quad m \xrightarrow{\text{pump}} m \xrightarrow{\text{probe}} m+1, \end{array}$$

the two probe transitions may be viewed as part of a single double resonance, for which the probe intensity is the sum of two terms. Therefore, we may write

$$\begin{aligned} \sum_m \mu_{ab}(m) \int_{-\infty}^{\infty} \bar{d}_{ba}''(m, \nu_y) d\nu_y = \sum_m [\mu_{ab}(m+1 \leftarrow m) x_{ab}(m+1 \leftarrow m) \\ + \mu_{ab}(m-1 \leftarrow m) x_{ab}(m-1 \leftarrow m)] \bar{d}_{ba}''(m). \end{aligned} \quad (\text{A4})$$

For a probe transition in the $2\nu_3 \leftarrow \nu_3$ band of CH_3F ,

$$\mu_{ab}(m \pm 1 \leftarrow m) = \mu_\nu \langle J, k, m \pm 1 | \phi_{Xz} | J, k, m \rangle \quad (\text{A5})$$

in which μ_ν is the vibrational transition moment for the $2\nu_3 \leftarrow \nu_3$ band and ϕ_{Xz} is the direction cosine between the space-fixed X and molecule-fixed z axis. Combination of Eqs. A1, A4, and A5 with the definition of x_{ab} yields

$$\alpha_3 = \left(\frac{16\pi^2 \mu_\nu^2 N}{hc} \right) \nu \sum_m g(m) \bar{d}_{ba}''(m) \quad (\text{A6})$$

in which

$$g(m) = | \langle J', k, m+1 | \phi_{Xz} | J, k, m \rangle |^2 + | \langle J', k, m-1 | \phi_{Xz} | J, k, m \rangle |^2. \quad (\text{A7})$$

The density matrix factor \bar{d}_{ba}'' is calculated by solving the density matrix equations for a 3-level system. The form of the equations used in this work is described in detail elsewhere¹¹ and is essentially equivalent to other published forms (e.g., Refs. 121,142,143). In our calculation, we assume a three-level system with energies $E_g < E_a < E_b$. By setting N in Eq. A1 to the number of molecules in state g at thermal equilibrium, the thermal equilibrium values of the diagonal elements of the density matrix are each calculated relative to $\rho_{gg}^\circ = 1$. Therefore, for example, for a single m component of level a ,

$$\rho_{aa}^\circ = \exp(-h\nu_p/k_B T) \quad (\text{A8})$$

in which ν_p is the center frequency of the pump transition, k_B is the Boltzmann constant, and T is the temperature. The absorption coefficient in Eq. A6 has been written as α_3 to identify it as the absorption coefficient for three-level double resonance.

To obtain the counterpart of Eq. A6 for four-level double resonance, we begin again with Eq. A1 in which ν is the center frequency, μ_{ab} is the transition moment, and d''_{ba} is the off-diagonal density matrix for the probe transition ($E_g < E_e$ are the pumped levels and $E_a < E_b$ are the probed levels.). In this case,

$$\int_{-\infty}^{\infty} d''_{ba}(m, \nu_y) d\nu_y = x_{ab}(m) \bar{d}''_{ba} \quad (\text{A9})$$

where $x_{ab}(m)$ is still $\mu_{ab}(m)E^o/h$, but now \bar{d}''_{ba} is independent of m since we assume that the probe power is non-saturating. Therefore, in this case of four-level double resonance,

$$\alpha_4 = \left(\frac{16\pi^2 \mu_v^2 N}{hc} \right) \nu S_{Jk} \bar{d}''_{ba}, \quad (\text{A10})$$

in which

$$S_{Jk} = \begin{cases} [(J+1)^2 - k^2]/3(J+1) & \text{for } J+1 \leftarrow J \\ (2J+1)k^2/3J(J+1) & \text{for } J \leftarrow J \\ (J^2 - k^2)/3J & \text{for } J-1 \leftarrow J \end{cases} \quad (\text{A11})$$

The S_{Jk} defined here differ from those often seen (e.g. Ref. (144)) because they include summation over m , but exclude summation over the directions of the space-fixed axes, which is just the reverse of the usual formulation.

For both 3-level and 4-level double resonance in the work described here, the probe beam power, sample pressure, and optical path length are sufficiently low that absorption by the probe is not only non-saturating but also may be considered to be optically thin, so that the spectrometer signal may be written

$$S = GI_o l \alpha \quad (\text{A12})$$

where l is the path length, I_o is the incident intensity of the probe, and G is an instrument gain factor. As a result of the amplitude modulation of the pump and the coherent detection, the observed signal is in fact,

$$\Delta S = S_{on} - S_{off} = GI_o l (\alpha_{on} - \alpha_{off}) \quad (\text{A13})$$

in which S_{on} and α_{on} are the spectrometer output and the absorption coefficient with the pump beam on and S_{off} and α_{off} are corresponding values for the pump beam off.

For three-level double resonance, substitution from Eq. A6 into Eq. A13 gives

$$\Delta S_3 = C \nu_3 \sum_m g(m) \Delta \bar{d}_{ba}''(m) \quad (\text{A14})$$

where C is the quantity in parenthesis in Eq. A6 multiplied by $GI_0 l$ and $\Delta \bar{d}_{ba}''(m)$ is the pump on minus pump off value of $\bar{d}_{ba}''(m)$ for three-level double resonance; ν_3 is the center frequency of the three-level probe transition. For four-level double resonance, substitution from Eq. A10 into Eq. A13 gives Eq. 2.6,

$$\Delta S_4 = C \nu_4 S_{Jk} \Delta \bar{d}_{ba}'' \quad (\text{A15})$$

where ν_4 is the center frequency of the four-level probe transition and $\Delta \bar{d}_{ba}''$ is the pump on minus pump off value for the four-level double resonance given in Eq. 2.8 with $\Delta \rho_{bb} \cong 0$ and $\Delta \rho_{aa}$ as in Eq. 2.22. Comparison of Eq. A14 and Eq. A15 shows that measuring and fitting three-level and four-level spectra under identical spectroscopic conditions should allow determination of the ratios $\bar{\rho}_{aa}^{(i)}/\Delta \bar{\rho}_{ee}$, as defined in Eq. 2.26. This is the basis for the interpretation of the relative intensities for three-level and four-level spectra discussed in the text.

BIBLIOGRAPHY

- ¹C. Wieman and T. W. Hansch. Doppler-free laser polarization spectroscopy. *Phys. Rev. Lett.*, 36(20):1173-3, 1976.
- ²A. Szoke and A. Javan. Isotope shift and saturation behavior of the 1.15- μ transition of Ne. *Phys. Rev. Lett.*, 10(12):521-524, 1963.
- ³R. A. McFarlane, W. R. Bennett, and W. E. Lamb. *Appl. Phys. Letters*, 2:189, 1963.
- ⁴W. E. Lamb. Theory of an Optical Maser. *Phys. Rev.*, 134A:1429-1449, 1964.
- ⁵A. L. Schawlow and C. H. Townes. Infrared and Optical Masers. *Phys. Rev.*, 112(6):1940-1949, 1958.
- ⁶A. Javan, Jr. W. R. Bennett, and D. R. Herriott. Population Inversion and Continuous Optical Maser Oscillation in a Gas Discharge Containing a He-Ne Mixture. *Phys. Rev. Letters*, 6(3):106-110, 1961.
- ⁷V. P. Chebotayev and V. S. Letokhov. Nonlinear narrow optical resonances induced by laser radiation. *Prog. Quant. Electr.*, 4:111-206, 1977.
- ⁸T. Hansch, M. D. Levenson, and A. L. Schawlow. Complete Hyperfine Structure of a Molecular Iodine Line. *Phys. Rev. Lett.*, 26(16):946-949, 1971.
- ⁹Uhyon Shin, Quan Song, and R. H. Schwendeman. Observation of Transferred Spikes in Infrared-Infrared Four-Level Double Resonance in $^{12}\text{CH}_3\text{F}$. In *Symposium On Molecular Spectroscopy*, volume 45, Ohio State University, Columbus, Ohio, June 1990.

- ¹⁰Uhyon Shin and R. H. Schwendeman. Time-Resolved Measurements of Transferred Spikes in Infrared-Infrared Four-Level Double Resonance in $^{12}\text{CH}_3\text{F}$. In *Symposium On Molecular Spectroscopy*, volume 45, Ohio State University, Columbus, Ohio, June 1990.
- ¹¹Q. Song and R. H. Schwendeman. Private Communication.
- ¹²Uhyon Shin and R. H. Schwendeman. Polarization Effects in Infrared-Infrared Double Resonance, 1991. Manuscript in preparation.
- ¹³T. S. Jaseja, A. Javan, and C. H. Townes. Frequency Stability of He-Ne Masers and Measurements of Length. *Phys. Rev. Letters*, 10(5):165–167, 1963.
- ¹⁴T. W. Hansch. Nonlinear high resolution spectroscopy of atoms and molecules. In *Nonlinear Optics*, N. Bloembergen, editor, pages 17–86. North-Holland Publ., Amsterdam, 1977.
- ¹⁵L. R. Hunter and S. K. Peck. Precision atomic lifetime measurements using collisionally induced coherence transfer. *Phys. Rev. A: Gen. Phys.*, 33(6):4452–5, 1986.
- ¹⁶W. Demtroder. *Laser Spectroscopy*. Chemical Physics 5. Springer-Verlag, Berlin, 1981.
- ¹⁷V. S. Letokhov. Saturation spectroscopy. In *High Resolution Laser Spectroscopy*, K. Shimoda, editor, Topics in Applied Physics 13, pages 95–173. Springer-Verlag, Berlin, 1977.
- ¹⁸B. J. Feldman and M. S. Feld. Theory of a High-Intensity Gas Laser. *Phys. Rev. A*, 1(5):1375–1396, 1970.
- ¹⁹B. J. Feldman and M. S. Feld. Laser-Induced Line-Narrowing Effects in Coupled Doppler-Broadened Transitions. II. Standing-Wave Features. *Phys. Rev. A*, 5(2):899–918, 1972.

- ²⁰Marc D. Levenson. *Introduction to nonlinear laser spectroscopy*, chapter 3. Academic press, Inc., 2nd edition, 1988.
- ²¹Atmospheric ozone. Technical report, World Meteorological Organization global ozone research and monitoring project-Report No. 16, Vol 3, 1985.
- ²²*Ozone depletion, greenhouse gases, and climate change*. National Academy Press, 1989. Proceedings of the Joint Symposium on Ozone Depletion, Greenhouse Gases, and Climate Change, held at the National Academy of Sciences, Mar. 23, 1988.
- ²³Mission to Planet Earth. Technical report, National Aeronautics and Space Administration, 1990.
- ²⁴H. G. Cho, Yukari Matsuo, and R. H. Schwendeman. High-Resolution Infrared Spectroscopy of the $\nu_3 + \nu_6 - \nu_6$ Band of $^{12}\text{CH}_3\text{F}$. *J. Mol. Spectrosc.*, 137:215–229, 1989.
- ²⁵Sang K. Lee, R. H. Schwendeman, Richard L. Crownover, David D. Skatrud, and Frank C. De Lucia. Study of the ν_3 and $2\nu_3 \leftarrow \nu_3$ Bands of $^{12}\text{CH}_3\text{F}$ by Infrared Laser Sideband and Submillimeter-Wave Spectroscopy. *J. Mol. Spectrosc.*, 123:145–160, 1987.
- ²⁶C. Freed, L. C. Bradley, and R. G. O'Donnell. *IEEE J. Quantum Electron.*, QE-16:1195–1206, 1980.
- ²⁷F. Russell Petersen, Earl C. Beaty, and C. R. Pollock. Improved Rovibrational Constants and Frequency Tables for the Normal Laser Bands of $^{12}\text{C}^{16}\text{O}_2$. *J. Mol. Spectrosc.*, 102:112–122, 1983.
- ²⁸Yukari Matsuo and R. H. Schwendeman. Observation of collisionally transferred spikes in fluoromethane-13C by infrared-infrared double resonance. *J. Chem. Phys.*, 91:3966–75, 1989.

- ²⁹Takeshi Oka. Microwave studies of collision-induced transitions between rotational levels. V. "Selection rules" in ammonia-rare-gas collisions. *J. Chem. Phys.*, 49(7):3135-45, 1968.
- ³⁰Takeshi Oka. Microwave studies of collision-induced transitions between rotational levels. IV. Steady-state measurements in ammonia. *J. Chem. Phys.*, 48(11):4919-28, 1968.
- ³¹Takeshi Oka. Collision-induced transitions between rotational levels. In *Adv. Atom. Mol. Phys.*, volume 9, pages 127-206. 1973.
- ³²J. Lemaire, J. Houriez, F. Herlemont, and J. Thibault. Efficiency of collisions in a microwave infrared four-level system in ammonia. *Chem. Phys. Lett.*, 19(3):373-6, 1973.
- ³³W. A. Kreiner, Achim Eyer, and Harold Jones. Collisional transfer of energy in ammonia investigated by infrared-microwave multiple-resonance experiments. *J. Mol. Spectrosc.*, 52(3):420-38, 1974.
- ³⁴M. Redon, H. Gurel, and M. Fourrier. Infrared-microwave double resonance in NH₃: Studies of collision-induced transitions in the presence of a high field Stark effect. *Chem. Phys. Lett.*, 30(1):99-103, 1975.
- ³⁵G. M. Dobbs, R. H. Micheels, J. I. Steinfeld, J. H. S. Wang, and J. M. Levy. Transient effects in time-resolved infrared-microwave double resonance of ammonia. *J. Chem. Phys.*, 63:1904, 1975.
- ³⁶H. Jones and F. Kohler. Infrared-Microwave Double Resonance in CF₃I and Microwave Spectroscopy in Emission and Absorption. *J. Mol. Spectrosc.*, 58:125-141, 1975.
- ³⁷F. Herlemont, J. Thibault, and J. Lemaire. Study of rotational relaxation in CH₃Br by infrared-microwave double resonance. *Chem. Phys. Lett.*, 41(3):466-469, 1976.

- ³⁸Satoru Kano, Takayoshi Amano, and Tadao Shimizu. Infrared-microwave double resonance studies of collision-induced transitions and energy transfer processes between vibration-rotation-inversion levels of ammonia. *J. Chem. Phys.*, 64(11):4711-18, 1976.
- ³⁹K. Shimoda. In *Laser Spectroscopy of Atoms and Molecules*, H. Walther, editor, pages 198-252. Springer, Berlin, 1976.
- ⁴⁰N. Morita, S. Kano, Y. Ueda, and T. Shimizu. Double resonance study of collisional relaxation on the frequency coincidence between the $\nu_2 R(2,0)$ line of $^{15}\text{NH}_3$ and the $R(42)$ line of CO_2 laser. *J. Chem. Phys.*, 66:2226-2228, 1977.
- ⁴¹Harold Jones. Two-photon spectroscopy of ammonia ($^{15}\text{NH}_3$) with isotopic carbon dioxide lasers and double resonance studies with a new coincidence. *J. Mol. Spectrosc.*, 70(2):279-87, 1978.
- ⁴²H. Jones. Infrared-Microwave Double Resonance Techniques. In *Modern Aspects of Microwave Spectroscopy*, G. Chantry, editor, pages 123-216. Academic Press, New York, 1979.
- ⁴³Harold Jones. Infrared-Microwave Double-Resonance and Two-Photon Experiments on Propynal with CO_2 Lasers. *J. Mol. Spectrosc.*, 81:21-36, 1980.
- ⁴⁴T. Amano and R. H. Schwendeman. Infrared-microwave double resonance study of the ν_4 fundamental band of phosphoryl fluoride. *Chem. Phys.*, 57(3):333-40, 1981.
- ⁴⁵Yukari Matsuo, Sang K. Lee, and R. H. Schwendeman. Observation of collisionally transferred spikes in ammonia by infrared-infrared double resonance. *J. Chem. Phys.*, 91(7):3948-65, 1989.
- ⁴⁶Thomas W. Meyer and Charles K. Rhodes. Observation of Momentum transfer in rotationally inelastic molecular collisions of CO_2 with H_2 , He, CO_2 , and Kr. *Phys. Rev. Lett.*, 32(12):637-40, 1974.

- ⁴⁷William K. Bischel and Charles K. Rhodes. Study of momentum-transfer distributions in rotationally inelastic collisions of CO₂ with foreign gas perturbers. *Phys. Rev. A*, 14:176–188, 1976.
- ⁴⁸C. C. Jensen, T. G. Anderson, C. Reiser, and J. I. Steinfeld. Infrared double resonance of sulfur hexafluoride with a tunable diode laser. *J. Chem. Phys.*, 71(9):3648–57, 1979.
- ⁴⁹R. C. Sharp, E. Yablonovitch, and N. Bloembergen. Picosecond infrared double resonance studies on SF₆. *J. Chem. Phys.*, 74:5357, 1981.
- ⁵⁰M. Dubs, D. Harradine, E. Schweitzer, J. I. Steinfeld, and C. Patterson. Infrared double resonance of sulfur hexafluoride with a tunable diode laser. III. Observations of $2\nu_3 \leftarrow \nu_3$ transitions and collisional relaxation in $\nu_3 = 1$. *J. Chem. Phys.*, 77(8), 3824–39, 1982.
- ⁵¹Hiroaki Kuze, Harold Jones, Motowo Tsukakoshi, Arimichi Minoh, and Michio Takami. Study of collisional relaxation in ammonia by steady-state, infrared-infrared double resonance. *J. Chem. Phys.*, 80(9):4222–9, 1984.
- ⁵²D. Harradine, B. Foy, L. Laux, M. Dubs, and J. I. Steinfeld. Infrared double resonance of fluoroform-d with a tunable diode laser. *J. Chem. Phys.*, 81:4267–80, 1984.
- ⁵³L. Laux, B. Foy, D. Harradine, and J. I. Steinfeld. Measurement of state-to-state rotational energy transfer in methane by infrared double resonance. *J. Chem. Phys.*, 80(7):3499–500, 1984.
- ⁵⁴Harold K. Haugen, William H. Pence, and Stephen R. Leone. Infrared double resonance spectroscopy of V-T, R relaxation of hydrogen fluoride ($\nu = 1$): direct measurement of the high-J populations. *J. Chem. Phys.*, 80(5):1839–52, 1984.
- ⁵⁵B. Foy, L. Laux, S. Kable, and J. I. Steinfeld. Rotational energy transfer cross sections in methane (¹³CD₄) from infrared double resonance measurements. *Chem. Phys. Lett.*, 118(5):464–7, 1985.

- ⁵⁶Yoshinori Honguh, Fusakazu Matsushima, Ryuichi Katayama, and Tadao Shimizu. Infrared-infrared double resonance in a supersonic molecular beam: Accurate determination of the cross section of collision induced rotational transitions in state selected NH₃. *J. Chem. Phys.*, 83:5052–5059, 1985.
- ⁵⁷K. Veeken, N. Dam, and J. Reuss. Vibrational and rotational relaxation of ammonia studied in a molecular jet by infrared-infrared double resonance. *Chem. Phys.*, 100(2):171–91, 1985.
- ⁵⁸Julian Keilson and James Storer. On Brownian motion, Boltzmann's equation, and the Fokker-Plank equation. *Q. Appl. Math.*, 10:243–53, 1952.
- ⁵⁹Matthew Borenstein and Willis E. Lamb, Jr. Effect of velocity-changing collisions on the output of a gas laser. *Phys. Rev. A*, 5(3):1311–23, 1972.
- ⁶⁰P. R. Berman, T. W. Mossberg, and S. R. Hartmann. Collision kernels and laser spectroscopy. *Phys. Rev. A*, 25(5):2550–71, 1982.
- ⁶¹J. E. Bjorkholm, P. F. Liao, and A. Wokaun. Distortion of on-resonance two-photon spectroscopic line shapes caused by velocity-selective optical pumping. *Phys. Rev. A*, 26(5):2643–55, 1982.
- ⁶²J. R. R. Leite, M. Ducloy, A. Sanchez, D. Seligson, and M. S. Feld. Measurement of molecular-alignment relaxation rate in NH₃ using non-lorentzian laser-induced saturation resonances. *Phys. Rev. Lett.*, 39(23):1465–9, 1977.
- ⁶³J. R. R. Leite, M. Ducloy, A. Sanchez, D. Seligson, and M. S. Feld. Laser saturation resonances in NH₃ observed in the time-delayed mode. *Phys. Rev. Lett.*, 39(23):1469–72, 1977.
- ⁶⁴Uhyon Shin and R. H. Schwendeman. Observation of $\Delta k = 3n$ selection rule in collisionally-induced transitions in methyl fluoride. *J. Chem. Phys.*, 1991. Accepted for publication.

- ⁶⁵Uhyon Shin, Q. Song, and R. H. Schwendeman. Observation and analysis of transferred spikes observed in infrared-infrared double resonance in CH₃F. To be submitted, 1991.
- ⁶⁶Paul R. Berman. Study of collisions by laser spectroscopy. *Adv. At. Mol. Phys.*, 13:57–112, 1977.
- ⁶⁷C. C. Feuillade and P. R. Berman. Theory of saturation spectroscopy including effects of level degeneracy. *Phys. Rev. A*, 29(3):1236–57, 1984.
- ⁶⁸P. R. Berman, D. G. Steel, Galina Khitrova, and Jing Liu. Effects of radiative decay in four-wave-mixing spectroscopy: narrow resonances produced by nonconservation of population, alignment, and orientation. *Phys. Rev. A: Gen. Phys.*, 38(1):252–62, 1988.
- ⁶⁹J. E. M. Haverkort, J. P. Woerdman, and P. R. Berman. Experimental determination of sodium-noble-gas velocity-changing and fine-structure-changing collision kernels. *Phys. Rev. A: Gen. Phys.*, 36(11):5251–64, 1987.
- ⁷⁰M. Ligare. Dressed-state analysis of three-level quantum-jump experiments. *Phys. Rev. A*, 37(9):3293–301, 1988.
- ⁷¹G. Millot, J. Hetzler, G. Pierre, and J. I. Steinfeld. Infrared double-resonance lineshapes in strongly pumped spherical-top molecules. *Spectrochim. Acta, Part A*, 45A(1):5–15, 1989.
- ⁷²R. M. Whitley and Jr. C. R. Stroud. Double optical resonance. *Phys. Rev. A*, 14(4):1498–513, 1976.
- ⁷³F. Y. Wu, S. Ezekiel, M. Ducloy, and B. R. Mollow. Observation of amplification in a strongly driven two-level atomic system at optical frequencies. *Phys. Rev. Lett*, 38(19):1077–80, 1977.
- ⁷⁴C. Delsart and J. C. Keller. Observation of the optical Autler-Townes splitting in neon gas with a cascade level scheme. *J. Phys. B: Atom. Molec. Phys.*, 9(15):2769–75, 1976.

- ⁷⁵C. Delsart and J. C. Keller. The optical Autler-Townes effect in Doppler-broadened three-level systems. *J. Phys. (France)*, 35:350–60, 1978.
- ⁷⁶J. E. Bjorkholm and P. F. Liao. Line shape and strength of two-photon absorption in an atomic vapor with a resonant or nearly resonant intermediate state. *Phys. Rev. A*, 14(2):751–60, 1976.
- ⁷⁷J. E. Bjorkholm and P. F. Liao. AC Stark splitting of two-photon spectra. *Opt. Comm.*, 21(1):132–6, 1977.
- ⁷⁸N. Dam, L. Oulejans, and J. Reuss. Relaxation rates of ethylene obtained from their effect on coherent transients. *Chem. Phys.*, 140:217–231, 1990.
- ⁷⁹Baoshu Zhang, Xijia Gu, N. R. Isenor, and G. Scoles. Transition dipole moment measurements for the ν_9 band of difluoromethane using Rabi oscillations. *Chem. Phys.*, 126(1):151–7, 1988.
- ⁸⁰A. G. Adam, T. E. Gough, N. R. Isenor, and G. Scoles. Rabi oscillations and Ramsey fringes in fluoromethane using carbon dioxide laser-Stark spectroscopy of a molecular beam. *Springer Ser. Opt. Sci.*, 49(*Laser Spectrosc.* 7), pages 138–9, 1985.
- ⁸¹Mark A. Kramer, Robert W. Boyd, Lloyd W. Hillman, and Jr. C. R. Stroud. Propagation of modulated optical fields through saturable-absorbing media: a general theory of modulation spectroscopy. *J. Opt. Soc. Am. B*, 2(9):1444–54, 1985.
- ⁸²P. F. Liao, J. E. Bjorkholm, and P. R. Berman. Effects of velocity-changing collisions on two-photon and stepwise-absorption spectroscopic line shapes. *Phys. Rev. A*, 21(6):1927–38, 1980.
- ⁸³M. E. Kaminsky, R. T. Hawkins F. V. Kowalski, and A. L. Schawlow. Identification of Absorption Lines by Modulated Lower-Level Population: Spectrum of Na_2 . *Phys. Rev. Lett.*, 36(12):671–673, 1976.

- ⁸⁴R. Teets, R. Feinberg, T. W. Hansch, and A. L. Schawlow. Simplification of spectra by polarization labeling. *Phys. Rev. Lett.*, 37:683, 1976.
- ⁸⁵N. W. Carlson, A. J. Taylor, K. M. Jones, and A. L. Schawlow. Two-step polarization-labeling spectroscopy of excited states of Na₂. *Phys. Rev. A*, 24(2):822–34, 1981.
- ⁸⁶M. Raab, G. Honing, W. Demtroeder, and C. R. Vidal. High resolution laser spectroscopy of Cs₂. II. Doppler-free polarization spectroscopy of. *J. Chem. Phys.*, 76(9):4370–86, 1982.
- ⁸⁷B. Hemmerling, R. Bombach, and W. Demtroeder. Rotational perturbations between Rydberg states of lithium dimer. *J. Chem. Phys.*, 87(9):5186–94, 1987.
- ⁸⁸B. Hemmerling, R. Bombach, W. Demtroeder, and N. Spies. Polarization labelling spectroscopy of molecular diatomic lithium Rydberg states. *Z. Phys. D: At., Mol. Clusters*, 5(2):165–73, 1987.
- ⁸⁹W. W. Quivers Jr. Production of highly polarized vapors using laser optical pumping with velocity-changing collisions. *Phys. Rev. A*, 34(5):3822–38, 1986.
- ⁹⁰J. Cooper, R. J. Ballagh, and K. Burnett. Zeeman degeneracy effects in collisional intense-field resonance fluorescence. *Phys. Rev. A*, 22(2):535–44, 1980.
- ⁹¹A. J. Bain and A. J. McCaffery. complete determination of the state multipoles of rotationally resolved polarized fluorescence using a single experimental geometry. *J. Chem. Phys.*, 80(12):5883–92, 1984.
- ⁹²A. J. Bain and A. J. McCaffery. On the measurement of molecular anisotropies using laser techniques. I. Polarized laser fluorescence. *J. Chem. Phys.*, 83:2627–31, 1985.
- ⁹³A. J. Bain and A. J. McCaffery. On the measurement of molecular anisotropies using laser techniques. II. Differential absorption of circularly and linearly polarized light. *J. Chem. Phys.*, 83:2632–41, 1985.

- ⁹⁴A. J. Bain and A. J. McCaffery. On the measurement of molecular anisotropies using laser techniques. III. Detection of the higher multipoles. *J. Chem. Phys.*, 83:2641–45, 1985.
- ⁹⁵C. G. Aminoff and M. Pinard. Velocity selective optical pumping. *J. Phys. (Les Ulis, Fr.)*, 43(2):263–77, 1982.
- ⁹⁶C. G. Aminoff, J. Javanainen, and M. Kaivola. Collision effects in velocity-selective optical pumping of sodium. *Phys. Rev. A*, 28(2):722–37, 1983.
- ⁹⁷Shigeru Nakayama. Inverted signals in polarization spectroscopy of sodium vapour. *J. Phys. Soc. Jpn.*, 50(2):606–8, 1981.
- ⁹⁸Shigeru Nakayama. Optical pumping theory in polarization spectroscopy of Na. *J. Phys. Soc. Jpn.*, 50(2):609–14, 1981.
- ⁹⁹Shigeru Nakayama. Velocity selective optical pumping spectroscopy of D1 line in alkali atoms. *J. Phys. Soc. Jpn.*, 53(10):3351–61, 1984.
- ¹⁰⁰S. Nakayama. Polarization spectroscopy of Rb and Cs. *Opt. Comm.*, 50(1):19–25, 1984.
- ¹⁰¹Shigeru Nakayama. Doppler-free laser spectroscopic techniques with optical pumping in D1 lines of alkali atoms. *J. Opt. Soc. Am. B: Opt. Phys.*, 2(9):1431–7, 1985.
- ¹⁰²W. Gawlik, J. Kowalski, F. Trager, and M. Vollmer. Subnatural linewidth effects in polarization spectroscopy. *Laser Spectroscopy VI*, pages 136–7, 1983.
- ¹⁰³Wojciech Gawlik. Nonstationary effects in velocity-selective optical pumping. *Phys. Rev. A*, 34(5):3760–9, 1986.
- ¹⁰⁴Jom Sool Kim, Hong Jin Kong, Sang Soo Lee, and Jung Bog Kim. Polarization-modulated optical pumping spectroscopy of Na D1 and D2 lines. *Phys. Rev. A.*, 39:2236–8, 1989.

- ¹⁰⁵Jack M. Preses and George W. Flynn. Infrared laser double resonance study of vibrational energy exchange between methyl (carbon-12) fluoride and methyl (carbon-13) fluoride. *J. Chem. Phys.*, 66(7):3112-16, 1977.
- ¹⁰⁶Eric Weitz, George W. Flynn, and A. M. Ronn. Laser excitation and equilibration of excited vibrational states in methyl fluoride. *J. Chem. Phys.*, 56(12):6060-7, 1972.
- ¹⁰⁷Eric Weitz and George W. Flynn. Deactivation of laser excited CH₃F in CH₃F-X mixtures. *J. Chem. Phys.*, 58(7):2679-83, 1973.
- ¹⁰⁸Eric Weitz and George W. Flynn. Partial vibration energy transfer map for methyl fluoride: A laser fluorescence study. *J. Chem. Phys.*, 58(7):2781-93, 1973.
- ¹⁰⁹J. S. Baskin, P. M. Felker, and A. H. Zewail. Doppler-free time-resolved polarization spectroscopy of large molecules: measurement of excited state rotational constants. *J. Chem. Phys.*, 84(8):4708-10, 1986.
- ¹¹⁰Rodney I. McCormick, Frank C. De Lucia, and David D. Skatrud. A time-resolved study of rotational and vibrational excitation and relaxation in the fluoromethane (13CH₃F) optically pumped far-infrared laser. *IEEE J. Quantum Electron.*, QE-23(12):2060-8, 1987.
- ¹¹¹B. Foy, J. Hetzler, G. Millot, and J. I. Steinfeld. State-to-state rotational energy transfer in methane (13CD₄) from infrared double-resonance experiments with a tunable diode laser. *J. Chem. Phys.*, 88(11):6838-52, 1988.
- ¹¹²Henry O. Everitt and Frank C. De Lucia. A time-resolved study of rotational energy transfer into A and E symmetry species of fluoromethane-13C. *J. Chem. Phys.*, 90(7):3520-7, 1989.
- ¹¹³Henry O. Everitt and Frank C. De Lucia. Rotational energy transfer in fluoromethane: The $\Delta J = n, \Delta K = 0$ processes. *J. Chem. Phys.*, 92(11):6480-91, 1990.

- ¹¹⁴C. P. Bewick and B. J. Orr. Rotationally specific mode-to-mode vibrational energy transfer in D_2CO/D_2CO collisions. I. Spectroscopic aspects. *J. Chem. Phys.*, 93(12):8634–42, 1990.
- ¹¹⁵C. P. Bewick, J. F. Martins, and B. J. Orr. Rotationally specific mode-to-mode vibrational energy transfer in D_2CO/D_2CO collisions. II. Kinetics and modeling. *J. Chem. Phys.*, 93(12):8643–57, 1990.
- ¹¹⁶P. L. Chapovskii, A. M. Shalagin, V. N. Panfilov, and V. P. Strunin. Light-induced drift of fluoromethane molecules. *Opt. Commun.*, 40(2):129–34, 1981.
- ¹¹⁷V. N. Panfilov, V. P. Strunin, P. L. Chapovskii, and A. M. Shalagin. Light-induced drift and separation of the components of the mixture $^{13}CH_3F+^{12}CH_3F$ in a continuous IR-radiation field. *JETP Lett.*, 33(1):48–51, 1981.
- ¹¹⁸L. N. Krasnoperov, V. N. Panfilov, V. P. Strunin, and P. L. Chapovskii. Photoinduced-drift separation of the o- and p- modifications of CH_3F . *JETP Lett.*, 39(3):143–6, 1984.
- ¹¹⁹P. L. Chapovskii, L. N. Krasnoperov, V. N. Panfilov, and V. P. Strunin. Studies on separation and conversion of spin modifications of CH_3F molecules. *Chem. Phys.*, 97:449–455, 1985.
- ¹²⁰P. L. Chapovskii. Conversion of nuclear spin modifications of CH_3F molecules in the gaseous phase. *Sov. Phys. JETP*, 70(5):895–901, 1990.
- ¹²¹S. T. Sandholm and R. H. Schwendeman. The line shape of a zero-field level-crossing effect in methyl fluoride. *J. Chem. Phys.*, 78(6):3476–3482, 1983.
- ¹²²A. J. McCaffery, M. J. Proctor, and B. J. Whitaker. Rotational energy transfer: polarization and scaling. *Ann. Rev. Phys. Chem.*, 37:223–44, 1986.
- ¹²³R. Clark Jones. A New Calculus for the Treatment of Optical Systems. I. Description and Discussion of the Calculus. *J. Opt. Soc. Am.*, 31:488–493, 1941.

- ¹²⁴R. Clark Jones. A New Calculus for the Treatment of Optical Systems. II. Proof of Three General Equivalence Theorems. *J. Opt. Soc. Am.*, 31:493–499, 1941.
- ¹²⁵R. Clark Jones. A New Calculus for the Treatment of Optical Systems. III. The Sohncke Theory of Optical Activity. *J. Opt. Soc. Am.*, 31:500–503, 1941.
- ¹²⁶R. Clark Jones. A New Calculus for the Treatment of Optical Systems. IV. *J. Opt. Soc. Am.*, 32:486–493, 1942.
- ¹²⁷R. Clark Jones. A New Calculus for the Treatment of Optical Systems. V. A More General Formulation and Description of Another Calculus. *J. Opt. Soc. Am.*, 37:107–110, 1947.
- ¹²⁸R. Clark Jones. A New Calculus for the Treatment of Optical Systems. VI. Experimental Determination of the Matrix. *J. Opt. Soc. Am.*, 37:110–112, 1947.
- ¹²⁹R. Clark Jones. A New Calculus for the Treatment of Optical Systems. VII. Properties of the N -matrices. *J. Opt. Soc. Am.*, 38:671–685, 1948.
- ¹³⁰R. Clark Jones. A New Calculus for the Treatment of Optical Systems. VIII. Electromagnetic Theory. *J. Opt. Soc. Am.*, 46:126–131, 1956.
- ¹³¹David S. Kliger, James W. Lewis, and Cora E. Randall. *Polarized Light in Optics and Spectroscopy*. Academic Press, Inc., 1990.
- ¹³²Gottfried Magerl, Walter Schupita, and Ernst Bonek. A tunable CO₂ laser sideband spectrometer. *IEEE. J. Quantum. Electron.*, QE-18:1214–20, 1982.
- ¹³³Sang K. Lee, R. H. Schwendeman, and Gottfried Magerl. Infrared microwave sideband laser spectroscopy of the ν_3 and $2\nu_3 \leftarrow \nu_3$ bands of fluoromethane (¹³CH₃F). *J. Mol. Spectrosc.*, 117(2):416–34, 1986.
- ¹³⁴Thomas Williams and Colin Kelley. Gnuplot v2.0, 1990. an interactive plotting program.
- ¹³⁵Math Works inc. Matlab, 1989. an interactive matrix calculation program.

- ¹³⁶R. H. Schwendeman. G34DRD. A three-level double resonance calculation program.
- ¹³⁷C. Liedenbaum, S. Stolte, and J. Reuss. Inversion produced and reversed by adiabatic passage. *Phys. Rep.*, 178(1):1-24, 1989.
- ¹³⁸Y. H. Zou and N. Bloembergen. Collision-enhanced Hanle resonances and transverse optical pumping in four-wave light mixing in sodium vapor. *Phys. Rev. A: Gen. Phys.*, 33(3):1730-42, 1986.
- ¹³⁹S. M. Freund, G. Duxbury, M. Romheld, J. T. Tiedje, and T. Oka. Laser Stark spectroscopy in the 10 μm region: the ν_3 bands of CH_3F . *J. Mol. Spectrosc.*, 52(38):38-57, 1974.
- ¹⁴⁰V. P. Chebotayev. Three-Level Laser Spectroscopy. In *High-Resolution Laser spectroscopy*, K. Shimoda, editor, Topics in Applied Physics, 13, pages 207-255. 1976.
- ¹⁴¹B. Wellegehausen. Optically pumped cw dimer lasers. *IEEE J. Quant. Electron.*, QE-15:1108-1130, 1979.
- ¹⁴²Michio Takami. Theory of optical-microwave double resonance. I. Double resonance with optical radiation. *Jpn. J. Appl. Phys.*, 15(10):1063, 1976.
- ¹⁴³Michio Takami. Theory of optical-microwave double resonance. II. Double resonance with optical radiation. *Jpn. J. Appl. Phys.*, 15(10):1889-1897, 1976.
- ¹⁴⁴C. H. Townes and A. L. Schawlow. *Microwave Spectroscopy*. Dover, 1975.

MICHIGAN STATE UNIV. LIBRARIES



31293009139498